University of Napoli Federico II

PhD Program in Civil Systems Engineering

Department of Civil, Architectural and Environmental Engineering

Numerical Study of Flow Downstream a Step with a Cylinder

Milad Abdollahpour

Thesis submitted for the degree of PhD in Civil Systems Engineering
Napoli, February 2023

PhD Candidate:

Milad Abdollahpour Kohnehshahri

Supervisors:

Prof. Carlo Gualtieri - University of Napoli Federico II, Italy

Prof. Paola Gualtieri - University of Napoli Federico II, Italy

PhD Program Coordinator (XXXVI Cycle):

Prof. Andrea Papola - University of Napoli Federico II, Italy

Reading Committee:

Prof. Giacomo Viccione - University of Salerno, Italy

Dr. Jaroslav Tihon - The Czech Academy of Sciences, Czech Republic

Abstract

The backward-facing step flow (BFSF) is a classical problem in fluid mechanics, hydraulic engineering, and environmental hydraulics The nature of this flow, consisting of separation and reattachment, makes it a problem worthwhile to study. In this study, the effect of a cylinder placed downstream of the step on the 2D flow structure was investigated. The classical 2D BFSF was validated using OpenFOAM (Open-Source Field Operation and Manipulation). The BFSF characteristics such as, reattachment, recirculation zone, velocity profile, skin friction coefficient, and pressure coefficient were validated for a step-height Reynolds number in the range from 75 to 9,000, covering both laminar and turbulent flow. The numerical results at different Reynolds numbers of laminar flow and four RANS turbulence models (standard k-ε, RNG k-ε, standard k-ω, and SST k-ω) were found to be in good agreement with the literature data.

Later, the effect on the 2D flow structure of a cylinder placed at different horizontal and vertical locations downstream of the step was investigated. In the laminar flow, different Reynolds numbers were considered. In the turbulent flow, the effect on the flow structure of a cylinder placed at different horizontal and vertical locations downstream of the step was comparatively analyzed. When the cylinder was positioned below the step edge mid-plane, flow over the step was not altered by a cylinder. However, in other locations of a cylinder, the added cylinder modified the structure of flow increasing the skin friction coefficient in the recirculation zone. Also, the pressure coefficient of the bottom wall increased immediately downstream of the cylinder and farther downstream of the reattachment point remained stable in the flow recovery process. Moreover, the presence of the step significantly influenced the

dynamics of the vortex generation and shedding leading to an asymmetric wake distribution.

As the mixing of concentration in streams is a significant problem in environmental fluid mechanics, concentration transport studied to understand how release a pulse concentration is affected by cylinder in backward-facing step. Also, it is important to analyze the performance of hydraulic indices of concentration transport that are used in the literature to determine which index yields the most reliable results for the assessment of the pulse injection efficiency in sudden lateral expansions channel with the presence of cylindric obstacles.

The presence of step geometry at the bottom of rivers is of interest because of localized velocity gradients, affecting aquatic habitat. Finally, the effect of cylinder placement at different horizontal locations on the local variations of velocity distributions and habitat complexity metric downstream step were analyzed.

Acknowledgments

Completing a three-year life-project such as a PhD requires the collaboration of many people who, at different stages and in varied ways, contribute to maintaining the researcher's motivation. This doctoral research is a perfect example of this, so my most humble and sincere thanks go to:

My supervisors, Prof. Carlo Gualtieri and Prof. Paola Gualtieri, for challenging me to become an expert on my research field since the first day and for all the support and guidance through this process.

Prof. Carlo, I admire your dedication and commitment, always having time for a quick question. I am grateful for delivering your broad view and to-the-point feedback on time. This seems simple, but unfortunately not too many PhD students can say the same about their promotors. Thank you for being more than just a supervisor to me. Your dedication, kindness, and belief in my potential have been invaluable and inspiring. I feel privileged to have had you as my tutor and will always cherish the knowledge and skills you imparted to me.

Prof. Paola, I have much to say, it has been great to work with you during this time. I feel blessed to have had the opportunity to meet an exceptional woman who cares about people and has so much knowledge to share. The combination of a sharp point of view and positive and critical thinking was a very enjoyable way of discussing everything.

I am profoundly thankful to Dr. David F. Vetsch for having accepted me at the ETH Zurich and for having taught me how to conduct good research. I am sincerely grateful to him for having shared his expertise and network in the numerical modeling group and his hospitality.

I also would like to express my sincere gratitude to Prof. Andrea Papola, the PhD program coordinator, for his assistance in navigating the program requirements and *procedures. I am grateful for his patience and his prompt response to my queries throughout the program.*

I thank the doctoral committee Prof. Giacomo Viccione and Dr. Jaroslav Tihon for their valuable time spent reviewing my thesis and for their insightful comments and questions.

I would like to express my deepest gratitude to my wife, Nasrin, for her unwavering support, encouragement, and patience throughout my academic journey. Her love and dedication have been an endless source of motivation and inspiration, and I could not have accomplished this without her. She has always believed in me and has been my biggest cheerleader, even during the toughest times. I cannot thank her enough for her love, patience, and support, which have helped me achieve this significant milestone.

I am immensely grateful to my parents for their unwavering support and motivation throughout my academic pursuit. Their selfless sacrifices and constant encouragement have been instrumental in enabling me to successfully complete this thesis.

I thank my colleagues at DICEA, University of Naples Federico II: Roberta, Maria Cristina, Dina, Filomena, and Luiz, for the stimulating discussions, the time spent together, all the fun we have had, and for having believed in me.

I am most grateful to my colleagues at VAW, ETH Zurich, inevitable thanks go to Yannick for the inspiring discussions and for his invaluable support. I am grateful to Matthias and Frances for their invaluable assistance and warm welcome, as well as Matthew, Seline, Sudesh, and Mahmoud for their friendship and time spent together, as well as all the fellows and friends on campus.

Finally, I apologize if I have unintentionally omitted anyone who has provided support and encouragement throughout my graduate studies. I am grateful for their kindness and companionship, which made this experience more enjoyable.

Milad Abdollahpour

Table of Contents

List of Symbols

C_f	skin friction coefficient
$C_{f, min}$	minimum value of the skin friction coefficient
C_p	pressure coefficient
$C_{p, min}$	minimum pressure coefficient
$C_{p, BC}$	Borda-Carnot pressure coefficient
D	diameter of cylinder (L)
ER	expansion ratio of the channel
h	height of the step (L)
h_1	height of the inlet (L)
h_2	height of the outlet (L)
k	turbulent kinetic energy ($L^2 T^{-2}$)
L	turbulent length scale (L)
Lr	reattachment length (L)
M2	hydraulic complexity metric (L^{-1})
P	static pressure ($M L^{-1} T^{-2}$)
P_0	reference static pressure ($M L^{-1} T^{-2}$)
u,v	velocity components in x and y direction ($L T^{-1}$)
U_{max}	maximum velocity ($L T^{-1}$)

X	longitudinal coordinate (L)
Y	normal coordinate (L)
μ	dynamic viscosity of the fluid (M L^{-1} T^{-1})
υ	kinematic viscosity of the fluid (L^2 T^{-1})
ρ	fluid density (M L^{-3})
τ_w	wall shear stress (M L^{-1} $T^{-2)}$
ε	Turbulent dissipation (L^2 T^{-3})
ω	Specific dissipation rate (T^{-1})

Acronyms

ADE	Advection-diffusion equation
CFD	Computational Fluid Dynamics
DES	Detached eddy simulation
DNS	Direct numerical simulation
FVM	Finite volume method
LES	Large eddy simulation
RANS	Reynolds-averaged Navier-Stokes
RNG	Re-normalization group
SST	Shear stress transport
TKE	Turbulent kinetic energy

Dimensionless Numbers of Fluid Mechanics

Cr	Courant number
Re_h	Reynolds number based on step height
Re_D	Reynolds number based on cylinder diameter

List of Figures

List of Tables

Chapter 1 Introduction

In this first chapter, the key aspects of this study, the aim, and the approach of this Ph.D. dissertation are explained. General comments about the structure of the document are also included here.

1.1. Background of the study

Predicting the response of rivers to natural changes has been a challenging task for researchers from several disciplines over the last decades. In open channels, some morphological irregularities in the riverbeds, such as cavities, steps, and bedforms (called step-like geometry), as well as in the riversides, such as harbors, groins, and lateral expansion, have flow fields with separation at the edge that can produce recirculating downstream of the edge (Jackson et al. 2013). Such recirculation is essential in river engineering (Figure 1.1). These zones also favor the development of specific fauna and flora, which are influenced by the exchanges through the mixing layer separating the main flow and the recirculation area.

(a)

(b)

Figure 1.1. Some examples of channel expansion/contraction in nature (a) Groyne field in the River Lak, Netherlands (b) Lateral cavity in the River Meuse, Netherlands (source: Google Earth)

In the river, some obstacles such as vegetation, bridge piers in lateral expansion, as well as wood and logjams near or inside the vertical expansions, could be found, further modifying the flow properties (Figure 1.2). The presence of step-like geometries at the bottom of rivers is of interest because of the localized velocity gradients that occur between the step and the main flow current, affecting aquatic habitats. Eddies, transverse flows, velocity gradients, and other spatial flow patterns may enhance the biotic diversity of macroinvertebrates as well as fish and may increase the availability of favorable habitats for spawning, foraging, and refuge. Moreover, recirculation zones and transverse flows downstream of step-like geometry typically play an important role in stream ecology as they can develop habitat for fish and other aquatic organisms. So, understanding concentration transport (nutrient transport) downstream of step-like geometry is a significant issue in environmental fluid mechanics and river engineering (Gualtieri et al. 2010). The need to specify the flow interaction in such geometries leads to investigating that.


(a)


(b)

(c)

(d)

Figure 1.2. Some examples of channel expansion/contraction and cylindric obstacles in nature (a) Riparian vegetation - River Cecina, Italy (source: http://wiki.Reformrivers .eu) (b) Wood in the River Witibach, Switzerland (source: Neuhaus and Mende 2021) (c) Wood over the stepped channel in the River Pig Brook, England (source: Follett et al. 2021) (d) Logjams in the River Scherlibach, Switzerland (source: Neuhaus and Mende 2021)

Backward-facing step flow is one representative separation flow model, which is of significance in both theoretical and engineering development. Backward-facing step flow (BFSF) is one of the most important benchmarks in fluid mechanics. It involves the most important features of a separated flow, such as free shear flow, flow separation, separation, recirculation zone, reattachment, and redeveloping boundary layer. Such flow structures are presented in many applications such as flow over aircraft, around buildings, flow in a bottom cavity, and in stepped open channel flows. For environmental applications, the presence of a step at the bottom of rivers or lakes is of interest because of localized recirculation zones and transverse flows downstream of the step. Due to the wake dynamics of the BFSF, it is considered an optimal separated flow geometry in hydraulic engineering and environmental hydraulics (Ameur and Menni 2019). Such a flow is characterized by flow separation and reattachment induced by a sharp expansion of the configuration (Figure 1.3).

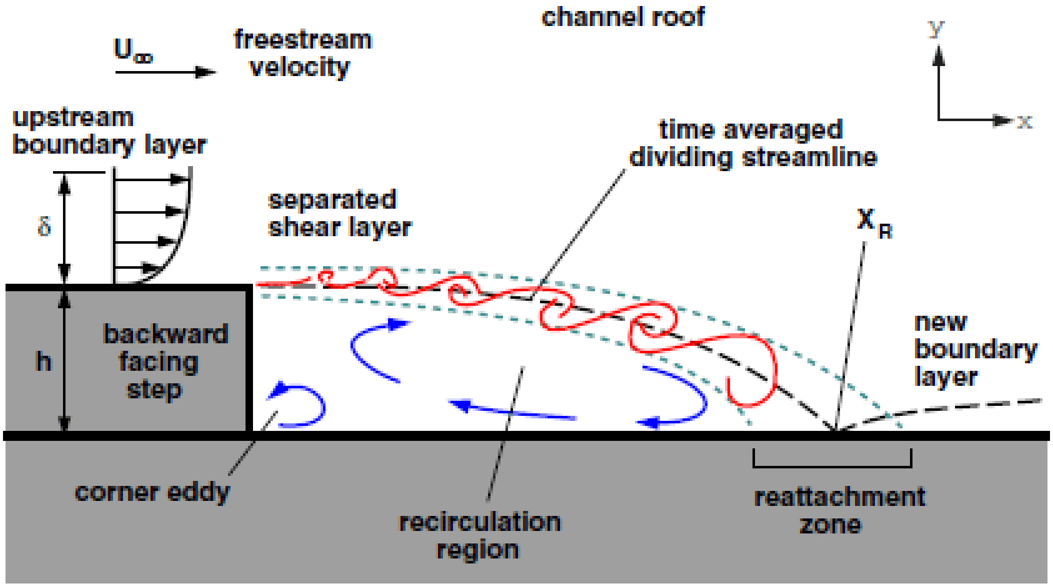

Figure 1.3. Detailed flow features of the backward facing step flow (source: Sallel et al. 2013)

In addition, a rigid cylinder model allows describing the main effects of the presence of woody vegetation in a step-like geometry. The cylinder creates a large drag due to the periodic separation and causes some differences in the pressure between the downstream and upstream. Characteristics of this flow are the separation and reattachment of the boundary layers, wake interactions, vortex breakdown, and merging (Lienhard 1966).

Control methods for recirculation flow downstream of the backward-facing step have emerged in recent years. A cylinder as benchmark in fluid mechanics can control the flow over a backward-facing step. Therefore, it's important to understand the interactions between the step and the cylinder.

In environmental applications, cylindrical obstacles such as wood or small logs may be trapped near the step, altering the turbulent properties of the flow.

Recirculation zones and transverse flows downstream of the step typically play an important role in stream ecology as they can increase the residence time of organic matter, and nutrients to enhance deposition processes.

During the last decade, computer simulations of physical processes have been used in scientific research leading to the analysis and design of engineered systems. Nowadays, numerical simulation is used to solve problems, not only to find a solution but also to ensure consistency between the modeling and the physical problem (Jauregui, 2011). Several computational studies have been performed to examine the influence of backward-facing step geometry in laminar and turbulent flow. To achieve the research aim, numerical simulation using Computational Fluid Dynamics (CFD) was employed. CFD is increasingly being used to investigate a wide range of complex environmental fluid mechanics (EFM) processes, Such as natural water systems, such as rivers, lakes, estuaries, and coastal waters. Typical examples are the study of the flow and of the transport and mixing of contaminants and sediments within those systems as well as floodplain inundation modeling (Czernuszenko and Rowinski, 2005). Also, CFD methods are sometimes applied in wastewater engineering (Gualtieri, 2006, Le Moullec et al 2010a, Le Moullec et al. 2010b, Samstag et al. 2016). Moreover, CFD methods have been applied to the analysis of hyporheic flows, e.g., mixing flow between surface and subsurface waters due to spatial and temporal variations in channel characteristics (Bayani-Cardenas, 2009; Endreny et al., 2011, Zhou and Endreny, 2013, Ren et al., 209).

1.2. Objectives and method of the Thesis

As pointed out, it is important to understand the changes in flow and turbulence characteristics using cylindrical obstacles on the stepped channel.

Of particular interest are the investigations of mean flow patterns and turbulence characteristics (reattachment, recirculation zone, velocity profile, velocity gradients, skin friction coefficient, pressure coefficient, and turbulent kinetic energy) around and in the recirculation zones of that structure. Also, the aim is to study the effects of a cylinder on the concentration transport downstream of the step, and on the local hydraulic complexity.

Important research questions regarding the above-mentioned structures that have yet to be explored are:

(1) What are the effects of the cylinder on the step in the laminar flow?

(2) What are the effects of the step on the dynamics of the vortex generation of a cylinder?

(3) Which turbulence models should be used to estimate the field flow downstream of the step in the recirculation zone? (4) What is the effect of the cylinder at different horizontal and vertical locations downstream of the step in turbulent flow?

(5) What is the effect of a cylinder on the concentration field due to its pulse load in recirculation zones downstream of the step?

(6) What is the effect of cylinder placement on the local variations of the habitat complexity metrics?

To address these questions, we employ a numerical simulation using Computational Fluid Dynamics (CFD). In the present study, numerical simulations are performed using the open-source code OpenFOAM (Open-Source Field Operation and Manipulation).

1.3. Structure of the thesis

Chapter 1 provides a general overview of the flow over the step with a cylindric obstacle and the importance of studying the behavior of flow in such a structure. The objectives of this research and thesis outline are also included in this chapter.

Chapter 2 includes a literature review of the backward-facing step flow (BFSF), flow past a cylinder, flow around rigid cylinders representing plants, and important parameters in analyzing concentration transport as well as the state of the art of its modeling.

Chapter 3 reports the numerical methodology, including geometry and mesh generation. In addition, the governing equations, initial and boundary conditions, and numerical schemes are presented for laminar and turbulent flow.

Chapter 4 presents the results of the validation of numerical simulations. This chapter reports the comparison results of the present numerical simulation, such as reattachment length, recirculation zone, velocity profile, skin friction, and pressure coefficient, with available literature data.

The next three chapters deal with the main findings of this study and its conclusions.

Chapter 5 reports the main results of the numerical study, such as reattachment length, recirculation zone, velocity profile, skin friction and pressure coefficient, turbulent kinetic energy, cylinder wakes, and how the cylinder interacts with these characteristics in both laminar and turbulent flow.

Chapter 6 includes the results of the concentration transport due to the pulse load of it in laminar flow downstream of the step and its change due to cylinder placement.

Chapter 7 reports the results of cylinder placement on the local variations of the habitat complexity metrics around the downstream step.

Finally, the conclusions are presented in **Chapter 8.**

Chapter 2 State of the art

In this chapter, the background of flow through backward facing flow step, flow around the cylinder, and important parameters in analyzing concentration transport are presented as well as the state of the art of its modeling.

2.1. Introduction

Flow separation has been investigated on a variety of different geometries, including sudden expanding, forward and backward-facing steps, cavities, high angle of attack airfoils, and bluff bodies such as cylinders. In bluff body flows, the separated shear layer has a natural instability that forms regular vortices that are shed downstream. In many separated flows, such as a backward-facing step, the separated shear layer interacts with the surface and naturally reattaches downstream, forming a recirculation region (Franck 2009).

The backward-facing step flow (BFSF) has been studied as an important flow dynamic model for more than half a century. The flow behind a cylinder is another classical benchmark in fluid mechanics. The cylinder creates a large drag due to the periodic separation and causes some differences in the pressure between downstream and upstream. This chapter reviews the research efforts on selected aspects of these flow phenomena.

2.2. Flow over the Backward Facing Step (BFSF)

The backward-facing step flow (BFSF) problem is one of the important problems in fluid mechanics. The basic geometric and physical model of backward-facing step (BFS) flow is shown in Figure 2.1 (under the 2-D scheme). Particularly, it is possible to distinguish several regions for BFSF: initial boundary layer, separated free shear layer, reattachment zone, primary recirculation or separation region, corner eddy (secondary recirculation region), redeveloping boundary layer, and second separation region (Gualtieri 2005).

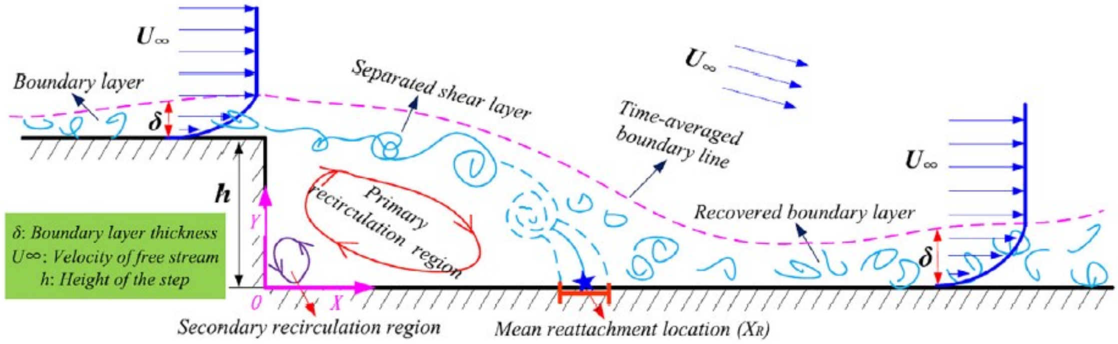

Figure 2.1. Sketch of the flow characteristics of the fluid passing a backward-facing step (source: Guo et al. 2017)

One of the earliest attempts to study flow over a BFSF was done experimentally by Abbott and Kline in 1962. Their results focused on the velocity profiles and the effects of different Reynolds numbers on flow properties. No major changes were found between the Reynolds number variation and the flow's reattachment zones in a fully developed turbulent flow. Flow separation, vortex evolution, and flow reattachment occur when the flow passes over the backward-facing step. When flow passes near boundaries with corners, vortices are generated near the corners. This phenomenon was predicted by Moffatt in 1964. Studies have been done to understand the length of the region where the vortices are generated for various geometries with corners. Flow over the backward-facing step has also been studied in dependence on the Reynolds number. Kim et al. (1980), experimentally investigated the flow characteristics of BFS geometry. Their results showed that the turbulent boundary layer's separation exerts a strong effect on the recovery region. Jovic and Driver (1994) performed experiments on turbulent flow over a BFS with Re_h= 5000. The simulation was set up such that it might be used to validate data from Le et al. 1997. Another experimental attempt to collect significant statistical data about the flow was done by Kasagi and Matsunaga (1995) in Re_h = 5540. Some of their interesting findings highlight that the normal stress in the spanwise direction played the most dominant role among the remaining normal stresses near the reattachment region.

In particular, Armaly et al. (1983), experimentally investigated the effect of step-height Reynolds number on flow separation by measurements of velocity distributions and the reattachment length over a wide range of Reynolds numbers (70 to 8000), hence covering laminar, transition, and turbulent regimes. In recent years, there are many experimental studies carried out, with various BFS designs.

It should be noted that the investigation of BFS flow from the laminar to the turbulent flow is different. The geometric parameters showed different effects on the flow separation and reattachment. Many studies have investigated the reattachment length and its parametric effects, such as expansion ratio (ER), and Reynolds number (Re) effects (Adams and Johnston 1988a, b, Durst and Tropea 1983, Kim 1978, Kuehn 1980, Ötügen 1991). Flow over BFS for varying expansion ratios was investigated experimentally by Durst and Tropea (1983), to understand the flow separation and reattachment. The results showed that the primary recirculation length increased non-linearly with an increasing expansion ratio at a constant Reynolds number. The effect of laminar Reynolds number for varying expansion ratios to understand flow separation and reattachment was studied by Biswas et al. (2004). The reattachment length increased as the expansion ratio and Reynolds numbers increased. While in turbulent flow, such length is independent of the step-height Reynolds number for low expansion ratios and increases as the expansion ratio increases (Durst and Tropea 1983, Heenan and Morrison 1998, Moss et al. 1979, Singh et al. 2011).

As such, many experimental (Bouda et al. 2008, Furuichi et al. 2004, Gautier and Aider 2014, Jovic and Driver 1995, Lee and Mateescu 1998, Tihon et al. 2001, Tihon et al. 2012, Tihon et al. 2010, Toumey et al. 2022) studies have been performed in laminar and turbulent flow. Chen et al. (2018), reviewed the recent theoretical, experimental, and numerical developments about BFSF. Besides those theoretical challenges with the separation and reattachment lengths explained herein, other features of the BFS study, such as the wall pressure coefficient and skin friction, are relevant. It is generally reported that both the pressure coefficient (C_P) and skin friction coefficient (C_f) show a drop near the step and then gradually increase again in the downward flow. The skin friction coefficient (C_f) is strongly dependent on the step-height Reynolds number (Lee and Mateescu 1998).

During the last decades, computer simulations of physical processes have been used in scientific research and the analysis and design of engineered systems. Several Computational Fluid Dynamics (CFD) studies (Al-Jelawy et al. 2016, Araujo and Rezende 2017, Biswas et al. 2004, DeBonis 2022, Erturk 2008, Gaur et al. 2022, Gualtieri 2005, Jehad et al. 2015, Kim and Moin 2010, Kopera et al. 2011, Singh et al. 2020, Yang et al. 2005) have been performed to examine the influence of backward-facing step geometry in laminar and turbulent flow. Representative experimental and numerical studies across a wide range of step-height Reynolds numbers are summarized in Table 2.1.

Table 2. 1. Characteristics of representative studies on backward-facing step flow

Reference	Flow Regime	Re_h	ER	Type of Study	Comment
Armaly et al. 1983	Laminar Transitional Turbulent	70 – 8,000	1.94	Experimental	-The effect of different Reynolds numbers on velocity distribution and reattachment length
Ruck and Makiola 1988	Turbulent	5,000 – 64,000	1.48 2 3.27	Experimental	- The effect of step angle and expansion ratio on flow characteristics
Suzuki et al. 1991	Laminar	700 1,000 1,400	2	Experimental	-Flow and heat transfer with a cylinder in different cross-stream positions
Furuichi et al. 2004	Turbulent	5,000	1.5	Experimental	-Investigation of spatio-temporal velocity fields of the separated shear layer and the reattachment region simultaneously
Gualtieri 2005	Laminar	75 – 1,006	2	Numerical (FemLab)	-The effect of Reynolds number on the primary and secondary reattachment and spanwise velocity profiles
Bouda et al. 2008	Turbulent	7,600	2	Experimental + Numerical (In-House code)	-The mean flow structure
Lan et al. 2009	Turbulent	20,000 – 50,000	1.25 1.48	Numerical (Fluent)	-The effect of different aspect ratios and Reynolds number on the flow and heat transfer
Al-Aswadi et al. 2010	Laminar	75-175	2	Numerical (In-House code)	-The effect of various types of nanofluids for heat transfer on the velocity distribution, pressure drop, wall shear stress, and skin friction coefficient encountered along both top and bottom walls

Tihon et al. 2012	Transitional	10–1,250	1.43–4	Experimental + Numerical (Fluent)	-The structure and stability of transitional flow were investigated in different channel expansion ratios and inlet flow conditions.
Prihoda et al. 2012	Turbulent	44,100 200,100 101,400	1.5	Experimental + Numerical (ANSYS CFX)	-The study was on the development of flow separation and changes of a free surface over an inclined step in the wide range of the Froude number
Selimefendigil and Öztop 2013	Laminar	50-200	2	Numerical (In-House code)	-Flow and heat transfer characteristics in pulsating flow with a stationary cylinder subjected to nanofluid
Togun et al. 2014	Laminar Turbulent	50 – 200 5,000 – 20,000	2	Numerical (In-House code)	-The study of heat transfer of turbulent and laminar Cu/water nanofluid
Selimefendigil and Öztop 2014	Laminar	10-200	2	Numerical (In-House code)	-The effects of Reynolds number, cylinder rotation angle, and strength of the magnetic dipole are studied for convective heat transfer enhancement over the step
Terekhov et al. 2016	Turbulent	15,500	1.43	Experimental	-The effect of the rib position and its height on the mean flow field, the intensity of turbulent fluctuations, and the size of the recirculation region behind the step
Choi and Nguyen 2016	Turbulent	5000-64,000	1.48 2 3.27	Numerical (OpenFOAM)	-The flow structures, separation flows, and reattachment lengths in various step angles and different expansion ratios
Xu et al. 2017	Turbulent	200 - 1,400	2	Numerical (Fluent)	-The characteristics of fluid flow and heat transfer in the

					low and middle Reynolds numbers
Park and Thornber 2018	Laminar Turbulent	100 140,000	2.25	Numerical (OpenFOAM)	-Flow past a transversely oscillating circular cylinder located in the downstream region
Anguraj and Palraj 2018	Laminar	1-200	2	Numerical (In-House code)	- Fluid flow and heat transfer with rotating cylinder
Wang et al. 2019	Turbulent	9,000	2	Experimental + Numerical (In-House code)	-The mean velocity, static pressure, Reynolds stresses, and the turbulent kinematic energy are investigated in different models
Luo 2019	Turbulent	5,100	1.2	Numerical (In-House code)	-The partially averaged Navier-Stokes (PANS) method was used in the simulation
Hussain and Ahmed 2019	Laminar	10 - 200	2	Numerical (In-House code)	-The forced convection flow of Fe3O4 H2O ferrofluids containing a rotating cylinder
Singh et al. 2020	Turbulent	7,000	2	Numerical (OpenFOAM)	-The assessment of several turbulent models including both Linear and Non-Linear eddy viscosity
Tahseen et al. 2020	Laminar	50, 100, 150, 200, 250	2	Numerical (Fluent)	-Fluid flow and heat transfer with three adiabatic cylinders
Min et al. 2020	Laminar	10 - 100	1.05	Numerical (In-House code)	-The study was focused on two-dimensional high Schmidt number mass transfer downstream of the step in a laminar flow, in which a nonreactive solute is initially confined to a region adjacent to the step
Loksupapaiboon and	Turbulent	15,500	1.43	Numerical	-Effects of the location of the passive disturbance to the

Suvanjumrat 2021				(OpenFOAM)	reattachment point behind the step were investigated with the presence of the rib.
Gaur et al. 2022	Turbulent	7,000	1.94	Numerical (OpenFOAM)	-The complex interactions between the vortices formed at the step edge, the upper wall, and the secondary vortices formed in the secondary re-circulation region.

It is widely acknowledged that the flow over the backward-facing step is controlled by the Reynolds number based on the inlet flow channel height (h) and the inlet flow velocity (U), the expansion ratio (ER) between the outlet flow channel height (H) and the inlet flow channel height (h), and the step angle. In laminar flow, the reattachment length increases as the expansion ratio and step-height Reynolds number increase. In turbulent flow, the reattachment length is independent of the step-height Reynolds number and increases as the step angle and the expansion ratio increase. The skin friction coefficient (Cf) is strongly dependent on the step-height Reynolds number (Tihon et al. 2001).

Two-equation eddy-viscosity models appear to be preferred among turbulence models because they incorporate significantly more turbulence physics and less special empiricism than algebraic models while avoiding numerical implementation difficulties and excessive computational cost when compared to other more complex models (Shu et al. 2006). For a long time, various Reynolds-Averaged Navier-Stokes (RANS) turbulence models have been used for investigating two-dimensional separating and reattaching flow (Smirnov et al. 2018).

Solving the RANS equations, such as the widely used k-model, is one common approach. Some research work has been done on different turbulence models in the reattachment length of backward-facing step flow (Anwar-ul-Haque et al. 2007, Araujo and Rezende 2017, Cruz et al. 2000, Kim et al. 1980, Shu et al. 2006). Recently, Wang et al. (2019), used k-ε and LES models for backward facing step at Reynolds number 9,000. The results showed that the LES model could not effectively simulate the boundary layer near the wall areas without extremely fine mesh, and it tends to overestimate separation at the top wall. These resulted in static pressure, mean velocity, and turbulent kinematic energy showing a larger peak value when compared to other methods.

Control methods for recirculation flow downstream of the backward-facing step have emerged in recent years. The controlling parameters of BFS may include various effects on separation, reattachment length, near-wall pressure coefficient, wall skin friction, velocity field, turbulent kinetic energy, and many others (Chen et al. 2018, HU et al. 2015, Nadge and Govardhan 2014, O'Malley et al. 1991). Controlling the BFSF with new geometric designs has been studied in recent years. A method based on suction or blowing downstream of the step has been studied by Uruba et al. (2007). Such geometric modifications reduced the length of the separation zone. More recently, the flow over an inclined step (Figure 2.2) has also been investigated (Bosnyakov et al. 2020, Chen et al. 2006b, Choi and Nguyen 2016, Iaccarino 2001, Louda et al. 2013, Mushyam et al. 2016, Prihoda et al. 2012, Ratha and Sarkar 2015, Ruck and Makiola 1993). Those studies showed that the size of the recirculation zone increased as the step angle increased.

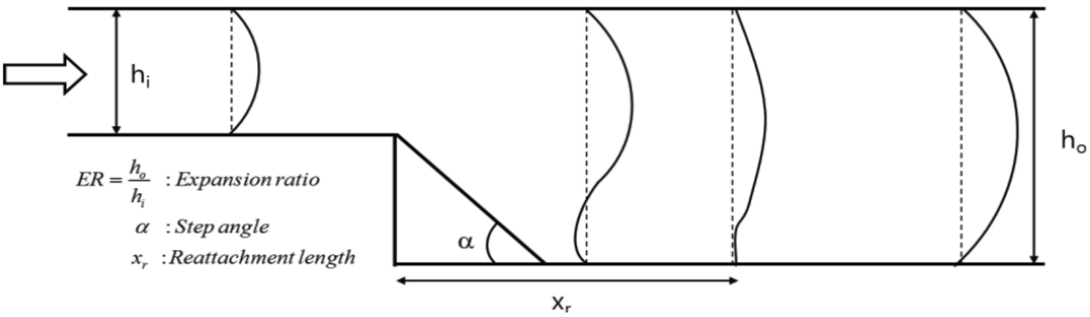

Figure 2.2. Geometry of the inclined backward-facing step flow studied by Choi and Nguyen (2016) with various step angles α = 10°, 15°, 20°, 25°, 30°, 45°, and 90°

The flow over a backward-facing step could be controlled using additional elements placed downstream or upstream of the step. As shown in Figure 2.3, the control of the separation region in the BFSF using rib upstream of the step was already studied (Barsukov et al. 2021, Loksupapaiboon and Suvanjumrat 2021, Terekhov et al. 2016). Those results demonstrated that a single rib upstream of the step is very effective in changing the average streamwise velocity profiles, and turbulent fluctuations, as well as in decreasing the reattachment length.

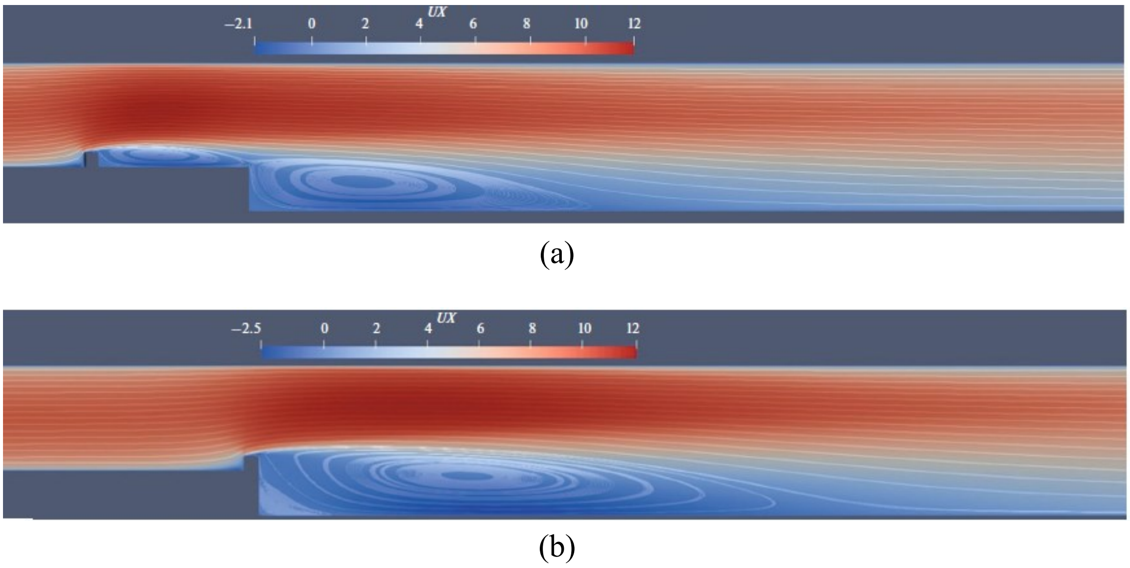

Figure 2.3. Streamwise velocity component for different locations of the rib studied by Barsukov et al. (2021) (a) rib installed upstream of step (b) rib installed over the step

In recent years, cylinders have also been used in the modification of BFS flows (Kumar and Dhiman 2012). Heat transfer and fluid flow characteristics over a backward or forward-facing step with the insertion of a cylinder have received some attention in the literature (Anguraj and Palraj 2018, Hussain and Ahmed 2019, Kumar and Dhiman 2012, Tahseen et al. 2020). Kumar and Dhiman (2012), studied the effect of a cylinder on separated forced convection at a BFSF. Their study focused on the heat transfer enhancement of BFSF laminar flow by using a single adiabatic circular cylinder. Chen et al. (2006a), designed a cylinder to test its effect on the temperature gradient in the BFSF. They applied the Lattice Boltzmann Method (LBM) in the Reynolds range limited to a maximum value of Re = 200. The results have shown that inserting the cylinder enhanced heat transfer and led to a reduction in the intersection angle between the velocity vector and the temperature gradient. Selimefendigil and Öztop (2014), (2015), designed a rotating cylinder in the BFS ferrofluid flow. Their results showed that the average heat transfer increased as the Reynolds number increased, and the rotating cylinder enhanced the heat transfer. Studies of a cylinder placed downstream of the step are mostly limited to heat transfer and magnetohydrodynamics. As emerged from the literature review, important gaps exist in the knowledge of the effect of different locations of a cylinder on the flow and turbulent characteristics of BFSF.

2.3. Flow past a cylinder (FPC)

The circular cylinder is a classic example of bluff body flow that has been studied extensively over the years. Several researchers have tried their strengths on this problem using different techniques. Steady flow past a solid sphere is important in many situations, both in the natural environment and in the world of technology, and it serves as a good reference case for an extension to more complicated situations, involving unsteady flows and/or non-uniform flows and/or non-spherical bodies.

Flow past a cylinder has been a traditional research subject of fluid dynamics as the flow field facilitates a variety of complex phenomena such as geometry-dependent vortex flow in the wake region, flow separation in the boundary layer, and flow transition from laminar to turbulent, despite its geometrical simplicity (Nguyen et al. 2021). The Reynolds number based on cylinder diameter D and the centerline velocity U is defined:

$$Re_D = \frac{\rho U D}{\mu} \tag{2.1}$$

The flow pattern around the cylinder changed as the Reynolds number increased (Catalano et al. 2003, Lienhard 1966, Mathupriya et al. 2018, Pereira et al. 2019). At low Reynolds numbers, the flow is laminar and steady, and the fluid moves smoothly around the cylinder without any significant disturbances. However, as the Reynolds number increases, the flow becomes unsteady. At high Reynolds numbers, the flow becomes fully turbulent, and the flow dynamics around the cylinder become even more complicated. In this regime, the flow exhibits strong fluctuations, which are characterized by the presence of large-scale structures that are associated with the formation of the boundary layer around the cylinder. The formation of these vortices is caused by the instability of the flow, which can be attributed to a feedback loop between the pressure field and the flow velocity. The vortices that are shed from the cylinder interact with each other, resulting in complex and intricate flow patterns. Figure 2.4 depicts flow patterns as the Reynolds number based on the cylinder diameter increases with increasing Reynolds numbers.

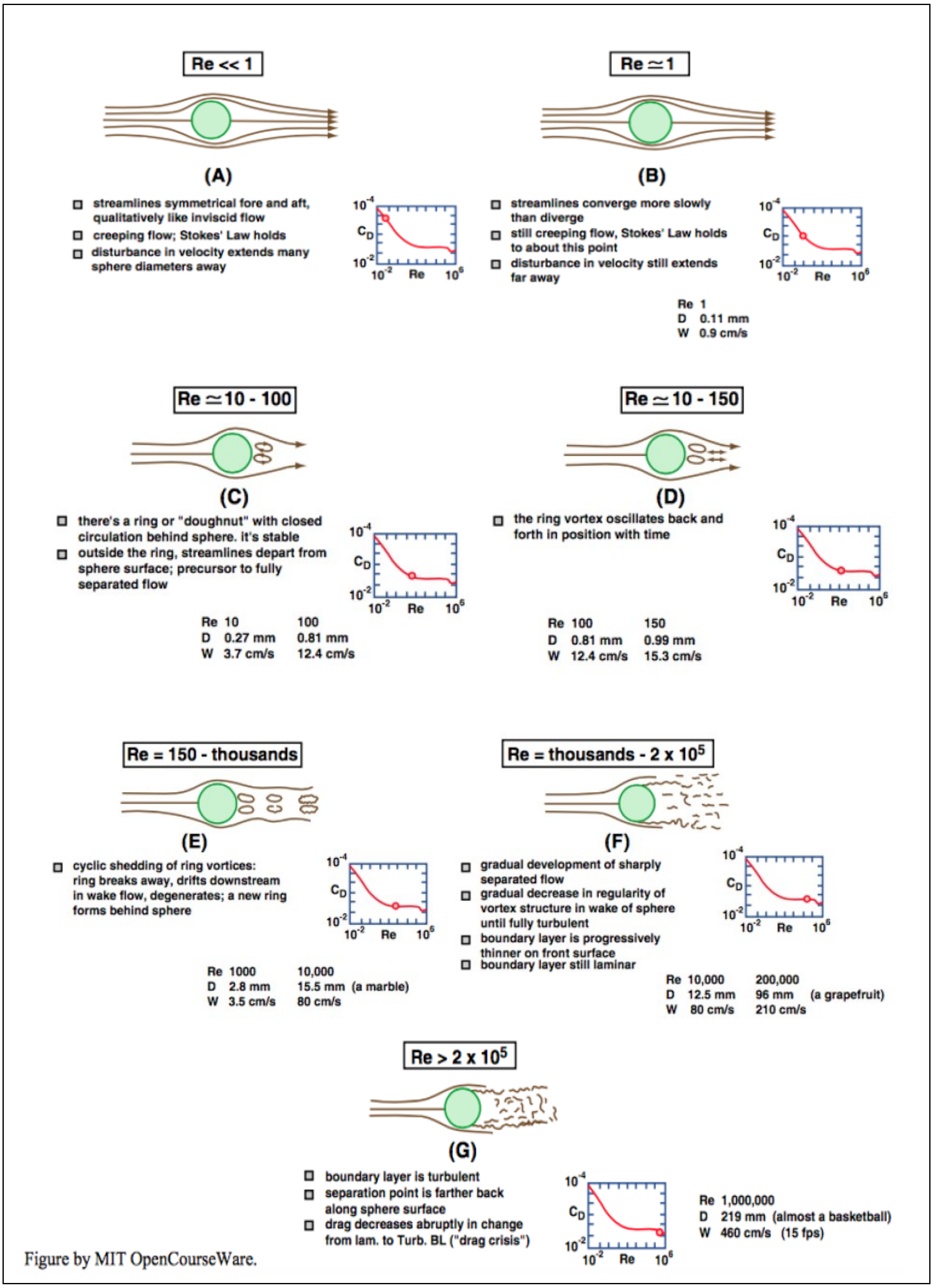

Figure 2.4. Flow patterns around a sphere at different Reynolds numbers (Southard 2000)

At very low Reynolds number, $Re_D < 1$ (Figure 2.4 - A), the flow pattern is symmetrical front to back. The flow lines are straight and uniform in the free stream far in front of the sphere, but they are deflected as they pass around the sphere. For a large distance away from the sphere the flow lines become somewhat more widely spaced, indicating that the fluid velocity is lower than the free-stream velocity. For $Re_D = 1$(Figure 2.4 - B), flow is the same as at lower Re_D, but streamlines converge more slowly back of the sphere than they diverge in front of the sphere. Corresponding to this change in the flow pattern, it is in about this range that the front-to-back pressure forces begin to increase more rapidly than predicted by Stokes' Law. Flow separation can be said to begin at a Re_D ~24. The point of separation is at first close to the rear of the sphere, and separation results in the formation of a ring eddy attached to the rear surface of the sphere. Flow within the eddy is at first quite regular and predictable (Figure 2.4 - C), thus not turbulent. As Re_D increases, the point of separation moves to the side of the sphere, and the ring eddy is drawn out in As the downstream direction and begins to oscillate and become unstable (Figure 2.4 - D). At Re_D values of several hundred, the ring eddy is cyclically shed from behind the sphere to drift downstream and decay as another form (Figure 2.2 - E). In this range of Re_c, turbulence begins to develop in the wake of the sphere. At first, turbulence develops mainly in the thin zone of strong shearing produced by flow separation and then spreads out downstream, but as Re reaches values of a few thousand the entire wake is filled with a mass of turbulent eddies (Figure 2.4-F).

In the range of Re_D from 1,000 to 200,000 (Figure 2.4 - F) the pattern of flow does not change much. The flow separates from the front stagnation point, and there is a fully developed turbulent wake. The drag is due mainly to the pressure distribution on the surface of the sphere, with only a minor contribution from viscous shear stress. The pressure distribution is as shown in Figure 2.4 and does not vary much with Re_D in this range, so the drag coefficient remains almost constant at about 0.5. At very high $Re_D > 200{,}000$, the boundary layer finally becomes turbulent before separation takes place, and there is a sudden change in the flow pattern (Figure 2.4 - G). The distinction here is between laminar separation, in which the flow in the boundary layer is still laminar where separation takes place, and turbulent separation, in which the boundary layer has already changed from laminar to turbulent at some point upstream of separation. The wake becomes contracted compared to its size when the separation is laminar, consequently, the very low pressure exerted on the surface of the sphere within the separation region acts over a smaller area (Southard 2000).

The circular cylinders in a crossflow have been a topic of research for over a hundred years, both in practical and fundamental importance. Practically, cylinders exist in many engineering and industrial applications, including offshore bridge piers and heat exchangers (Heseltine 2011).

CFD simulations have been widely used to study the flow past a cylinder. These simulations can provide detailed information about the flow structure and dynamics, including the formation and shedding of vortices, the evolution of the boundary layer, and the effects of various flow parameters, such as Reynolds number and cylinder shape. CFD simulations have shown that the flow past a cylinder is highly dependent on the Reynolds number, and that the shedding frequency of the vortices increases with the Reynolds number.

Numerous experimental and numerical investigations have been conducted on the flow over a circular cylinder in the past decades (Bishop and Hassan

1964, Brika and Laneville 1999, Kim and Choi 2005, Liaw 2005, Norberg 2003, Williamson 1996, Canuto and Taira 2015, Zafar and Alam 2019). A review of the different bluff-body wakes has been done by Derakhshandeh and Alam (2019).

Moreover, in environmental hydraulics, there are many aspects of flow around a cylinder that have interested researchers such as vegetation, plants, and wood.

Rigid cylinders could be used to represent the stems of plants in laboratory tests and numerical simulations. This section reviews the research efforts into selected aspects of this flow around a rigid cylinder representing the stem of a plant.

2.3.1. Flow around rigid cylinders representing the stem of a plant

Rigid cylinders have been used in laboratory experiments and numerical simulations to analyze the flow interaction in plant patches. The study of the flow around isolated cylindrical elements started in the early 1950s (Finn 1953, Triton 1959), but it was only 20 years later (Tollner et al. 1977) that arrays of cylinders were considered in laboratory experiments to simulate vegetation (Caroppi et al. 2018, Caroppi et al. 2021, Gualtieri et al. 2018, Gualtieri et al. 2004, Mihailović et al. 2017, Vargas-Luna et al. 2016). Figure 2.5 shows two examples of experimental modeling of plants carried out with rigid cylinders.

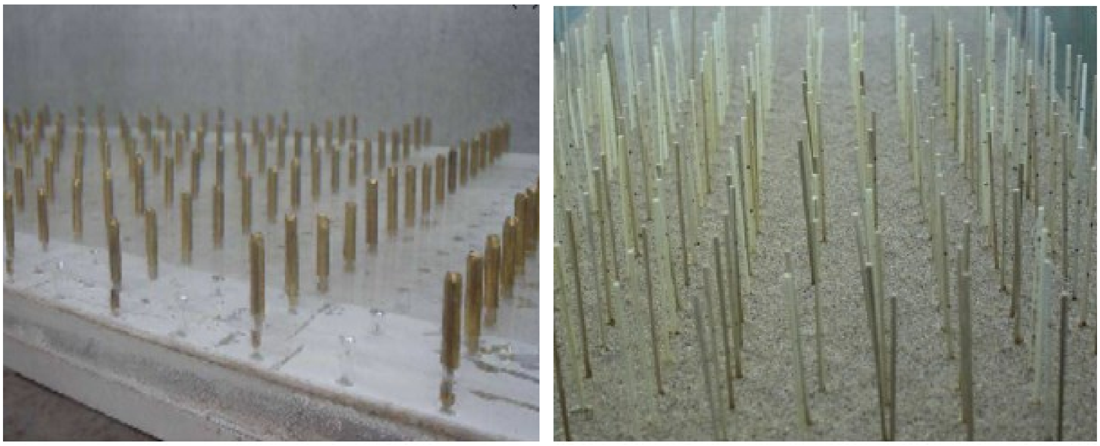

(a) (b)

Figure 2.5. Cylinders as the model of rigid vegetation (a) experimental set-up of Mihailović et al. (2017) (b) experimental set-up of Vargas Luna (2016)

Recently, numerical research on flow interaction has been carried out by simulating the stem of plant as rigid cylinders. For example, (Xiaohui and Li 2002, Marjoribanks et al. 2014, Zhao and Huai 2016, and Etminan et al. 2017) applied the Large Eddy Simulation (LES) technique for studying the turbulent flows in an open channel with the presence of cylinders. Zhang and Su (2008), applied the LES technique to studying turbulent flows in open channels with rigid and emergent cylinders. The model was validated by simulating flows in an open channel with vegetation at different densities and distributions, including full, partial, and isolated squares of vegetation. They found that the presence of vegetation, even at very low densities, had a pronounced influence on the dissipation of flow energy, both inside the vegetation domain and outside it, in the wake flow region. Cui and Neary (2008), studied turbulent flow with submerged cylinders using LES, with a focus on the role of turbulent structures on momentum transfer across the water–plant interface. Their results showed that, as for RANS models, LES models effectively simulated the effects of submerged cylinders on the mean flow field, and resolved turbulent structures observed in the flow field.

Li and Yan (2007), and Busari and Li (2015) employed the RANS model with the turbulence closure model to simulate flow interacting with rigid cylinders. Leu et al. (2008), applied the two-equation standard k-ε model for the closure of turbulence; Choi and Kang (2004), applied the multi-equation anisotropic Reynolds stress for the closure of turbulence. A standard k-ε model was implemented by Jahra et al. (2011), to clarify the mean velocity distributions and turbulent features in a compound channel with three different types of localized vegetation on the floodplain. They studied the effect, on the flow structure, of different types of cylinder arrangement on the floodplain. Their results showed a good agreement between numerical results and experimental observations relative to the mean velocity.

Gao et al. (2011), focused on the submerged and emergent vegetated flows using the RANS model. Their study aimed to acquire accurate velocity profiles without the more advanced two-equation turbulence models. They used a three-dimensional model with a simple two-layer mixing length. The velocity distribution predicted by the model were compared with laboratory measurements, with very good agreement. They found that the simple mixing length model could predict accurate complex velocity profiles with fewer coefficient data and less computational effort.

Stoesser et al. (2010), developed a LES model to resolve turbulent flow through emergent vegetation. They analyzed the effects of cylinder density and cylinder-diameter Reynolds number on the turbulence statistics and the instantaneous flow. They found good agreement between measured and simulated data confirming the great accuracy of the LES method. Huai et al. (2015), investigated steady uniform turbulent flows with an emergent rigid cylinder patch using LES. They focused on the effects of turbulence structures on the momentum transfer across the outer line of the vegetation region. Zhao and Huai (2016) analyzed the mean velocity profile and turbulence characteristics of flows through discontinuous rigid submerged patches of cylinders using LES. Moreover, they investigated the influence on the flow of cylinder density, Reynolds number, and distribution of the cylinders. They found that the coherent vortices, which were generated by the shear between the slower flow and the faster overlying flow, were associated with the velocity inflection and maximum Reynolds stress around the interface. These effects increased with high values of cylinder density and Reynolds number.

A two-dimensional Lattice Boltzmann Model (LBM) was developed to simulate the flow-vegetation interactions in an open channel with submerged rigid cylinders by Yang et al. (2017). It was found that the presented model was able to correctly simulate vegetated open channel flows. Tsai et al. (2017) investigated the moving effect of coastal vegetation on the damping of the tsunami wave with solitary waves passing over a group of emergent rigid cylinders using a numerical simulation with RNG k-ε turbulence model. Their numerical model was first validated using both previous laboratory data and numerical results of surface elevation evolution along the stationary cylinders. They found that the wave height was lower for moving cylinders than for stationary cylinders.

The RANS was adopted by Anjum et al. (2018), where the turbulent flow features through heterogeneous cylinder configuration were investigated utilizing CFD code FLUENT. The velocity was lower than in the vegetation areas (cylinder area), while the influence of patch distribution was not visible in the surface layer. The mean streamwise velocity considerably increased at the top of the vegetation and was almost constant inside the larger and shorter vegetation.

Cheng et al. (2019), simulated flow through suspended and submerged cylinders incorporating the interaction between the fluid field and the vegetation or structures. The numerical model was established based on RANS equations with additional cylinder drag terms. Turbulence was modeled using the two-equation k-ε model which considers the effect of cylinders by an approximation of dispersive fluxes using the drag force produced by the cylinder.

Ahmad et al. (2020), simulated flow properties by investigating the detailed velocity distribution and turbulence characteristics under varying conditions of submergence for short and tall vegetation over floodplains. The simulations were conducted using FLUENT based on the RSM. The flow velocities were significantly reduced in the floodplains due to resistance exerted by the vegetation. In general, the spatial distribution of mean flow and turbulence characteristics was considerably affected near the floodplain and main channel interfaces. A summary of these investigations is presented in Table 2.2.

Table 2. 2. Review of some recent studies in vegetation flow

Reference	Type of vegetation	Computational method	Cross section
Fischer-Antze et al. 2001	Submerged / Rigid	Standard k-ε (In-House code)	Rectangular/ Compound
Xiaohui and Li 2002	Emergent / Rigid	k-l, LES (In-House code)	Rectangular
Choi and Kang 2006	Submerged / Rigid	RSM (In-House code)	Rectangular
Dworak and Schwartz 2007	Woody Bank Vegetation	Standard k-ε (Flow -3D)	The 6.5-m wide channelized reach
Zhang and Su 2008	Emergent / Rigid	LES (In-House code)	Rectangular
Cui and Neary 2008	Submerged / Rigid	LES (In-House code)	Rectangular
Stoesser et al. 2010	Emergent / Rigid	LES (Hydro3D-GT)	Rectangular
Dimitris and Panayotis 2011	Submerged / Rigid	Standard k-ε, and RSM (In-House code)	Rectangular
Jahra et al. 2011	Emergent / Rigid	Standard k-ε (In-House code)	Compound
Stamou et al. 2011	Submerged / Rigid	Standard k-ε (ANSYS CFX)	Rectangular
Marjoribanks et al. 2014	Submerged/Flexible	LES (In-House code)	Rectangular
De Lima et al. 2015	Emergent / Rigid	Standard k- ε (Fluent)	Rectangular (sediment)
Huai et al. 2015	Emergent / Rigid	LES (In-House code)	Rectangular
Tsakiri et al. 2016	Emergent / Rigid	RNG k-ε (Fluent)	Rectangular
Yan et al. 2016	Submerged-Emergent / Rigid	Experimental Numerical (SA)	Rectangular

Zhao and Huai 2016	Submerged / Rigid	LES (In-House code)	Rectangular
Yang et al. 2017	Submerged / Rigid	LBM (In-House code)	Compound
Etminan et al. 2017	Emergent / Rigid	LES (In-House code)	Rectangular
Marjoribanks et al. 2017	Submersed aquatic vegetation	RNG k-ε (In-House code)	The River Browney in Durham
Zhao et al. 2017	Suspended canopies Rigid	Standard k-ε (Delft 3D)	Rectangular
Al-Asadi and Duan 2017	Submerged	Standard k-ε (Delft 3D)	Mississippi River and southwest of New Orleans
Tsai et al. 2017	Emergent / Rigid	RNG k-ε (Flow -3D)	Rectangular
Anjum et al. 2018	Submerged / Rigid	RSM (Fluent)	Rectangular
Lu and Dai 2018	Submerged / Flexible	LES (In-House code)	Rectangular (Sediment)
Kim et al. 2018	Emergent / Rigid	Standard k-ε (Fluent)	Rectangular (Suspended sediment deposition)
Zhou and Venayagamoorthy 2019	Suspended canopies	LES (In-House code)	Rectangular
Jing et al. 2019	Emergent / Rigid	LBM (In-House code)	Rectangular

Lera et al. 2019	Submersed aquatic vegetation	Standard k-ε Delft 3D	Field study in Chesapeake Bay (USA).
Cheng et al. 2019	Submerged / Flexible	k- ε (In-House code)	Rectangular
Ghani et al. 2019	Submerged / Rigid	RSM (Fluent)	Rectangular
Chen and Zou 2019	Submerged / Flexible	Standard k- ε (OpenFOAM)	Rectangular
Sonnenwald et al. 2019	Submerged and Emergent (Artificial/ Real)	Standard k-ε (Fluent)	Rectangular
Hemavathi et al. 2019	Submerged / Flexible	Standard k-ε (Flow -3D)	Rectangular
Huai et al. 2019	Emergent / Flexible	Experimental	Rectangular
Farzadkhoo et al. 2019	Emergent / Rigid	Experimental	Compound
Rahimi et al. 2020	Submerged / Rigid	Realizable k-ε (Fluent)	Rectangular
Ahmad et al. 2020	Submerged and Emergent / Rigid	RSM (Fluent)	Compound
Taheri Fard (2020)	Emergent / Rigid	RNG and LES (Flow -3D)	Compound
Kalinowska et al. 2020	Submerged / Rigid	SKM (CCHE2D)	Rectangular

Anjum and Tanaka 2020a	Submerged-Emergent / Rigid	RSM (Fluent)	Rectangular
Anjum and Tanaka 2020b	Submerged-Emergent / Rigid	RSM (Fluent)	Rectangular
Liu et al. 2021	Submerged / Rigid	LES (In-House code)	Rectangular
Zhang et al. 2022	Emergent / Rigid	Two-phase model (OpenFOAM)	Rectangular
Zhang and Zhang 2023	Emergent / Rigid	Standard k- ω (OpenFOAM)	Rectangular

LES: Large Eddy Simulation, VLES: Very Large Eddy Simulation, LBM: Lattice Boltzmann Model, RANS: Reynolds Averaged Navier–Stokes, RNG: Re-Normalization Group, RSM: Reynolds Stress Model, SAS: Scale Adaptive Simulation, SKM: Shiono and Knight Model (k-ε) k: is the turbulent kinetic energy, ε: is the rate of dissipation of turbulent kinetic energy

In smaller rivers, wood often lay in a spanwise and perpendicular orientation to the flow. The idealized prototype for this setup can be found in horizontal cylinders. Recently, circular cylinders have been used to investigate flow around horizontal wood. A numerical and experimental program on the flow around horizontal cylinders as large wood prototypes was studied by Bomers et al. (2020). They studied the effect of gap width underneath the cylinder on the transition from a mixing layer to a wake flow regime. Experimental data is used to benchmark numerical models with a focus on engineering e.g., statistical properties of the flow field, retention of particles in the wake, and drag-based flow resistance. Penna et al. (2020) studied the turbulence characteristics of horizontal cylinders in different conditions of submergence, to deepen the knowledge investigating the flow-structure interactions with a mobile bed. The results revealed that suspended and laid on cylinders behave differently from half-buried cylinders if subjected to the same hydraulic conditions. In the latter case, vortex shedding downstream of the cylinder is suppressed by the presence of the bed surface that causes an asymmetry in the development of the vortices. This implies that strong turbulent mixing processes occur downstream of the uncovered cylinders, whereas in the case of half-buried cylinders they are confined within the scour hole

Recently, Schalko et al. (2021) experimentally studied the flow and wake characteristics of a cylinder representing large wood. Different wood placements were tested (Figure 2.6). Physical model tests were used to explore how the wood position and submergence level (discharge) affect wake structure, and, hence, the resulting habitat. As a result, emergent logs placed at the channel center resulted in ten times higher turbulent kinetic energy compared to submerged logs. In addition, both spatial variations in time-mean velocity and turbulence level increased with increasing log length and decreasing submergence level. Submerged logs and logs placed at the channel side created a greater velocity deficit and a longer recirculation zone, both of which can increase the residence time in the wake and can lead to the deposition of organic matter and nutrients. The results demonstrated that variation in log size and degree of submergence can be used as a tool to vary habitat suitability for different fish preferences.

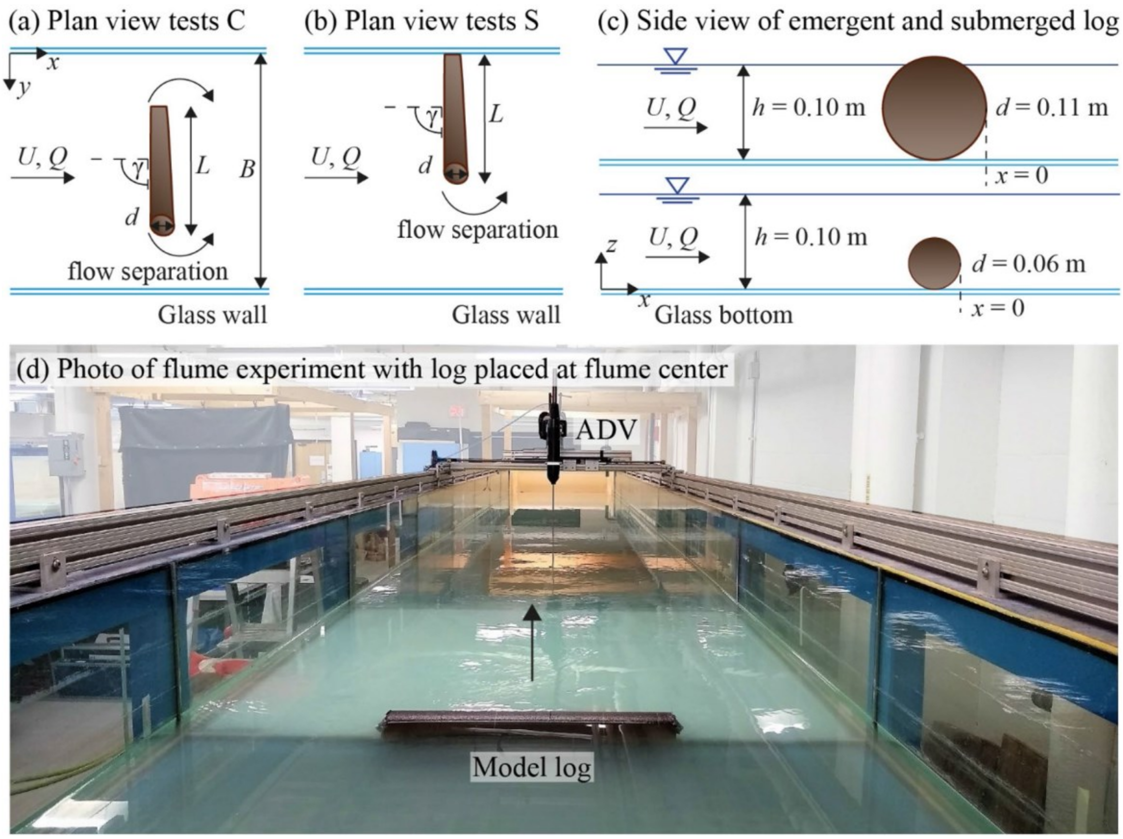

Figure 2.6. (a) Plan view of test setup with log positioned at channel center, (b) side, denoted by "S", with U = cross-sectional averaged flow velocity, Q = discharge, d = log diameter, L = log length, γ = log orientation angle, B = channel width, and h = flow depth; (c) side view of emergent and submerged log; (d) photo of flume experiment looking downstream. Note that x = 0 was defined at the downstream trailing edge of the log (Schalko et al. 2021)

A significant amount of research was carried out on the flow through woody plants, with many studies using rigid cylinder. The rigid cylinder model allows describing the main effects of the presence of an obstruction in the flow. Additionally, both experimental and numerical studies have been conducted on the flow past a rigid cylinder. However, there is a lack of research on the interaction between a backward-facing step and a cylinder in the same flow field. The absence of such results has motivated the current study to investigate this gap in the literature. By studying the combination of flow over a backward-facing step and flow past a cylinder, the research aims to provide new insights into the complex nature of flow around complex geometries and shed light on the effects of different cylinder positions, and Reynolds numbers on the flow field. Furthermore, the study could contribute to the development of more accurate and efficient numerical models for predicting fluid flow around complex geometries, which could be applied in various fields such as environmental engineering and fluid mechanics. Therefore, it is essential to investigate the interaction between a backward-facing step and a cylinder in the same flow field to advance the understanding of complex flows and their applications.

2.4. Solute transport

As pointed out, morphological irregularities such as cavities, steps, and dead zones can produce recirculating flows that occur on different scales on both the riverbanks and the riverbed (Gualtieri 2010). An obstacle plays a significant role in the sustainable development of streams and rivers, and it has important effects on the flow characteristics such as the velocity distributions, turbulence structures, and the process of concentration transport. Thus, the study of concentration transport through a recirculation zone is essential to understand the physical processes involved, which will provide important information for proper water environment and resource management. Numerous studies on solute transport in dead zone flow (Gualtieri 2008, Gualtieri 2010, Gualtieri et al. 2010, Lees et al. 2000, Sokáč et al. 2018, 2019, Wu and Yu 2021); cavities flow (Chang et al. 2007, Gualtieri 2009b); step channel (Min et al. 2020) have been conducted.

A scalar equation that is linked to the momentum transport equations, to provide the spatial distribution of concentration. The advection-diffusion equation (ADE) is widely applicable in a variety of physical, chemical, and biological processes that involve both turbulent diffusion and advection The ADE has been used as a model equation in many engineering problems such as the dispersion of tracers in porous media, nutrient transport in rivers and streams, the dispersion of dissolved material in estuaries and coastal seas, concentration dispersion in shallow lakes, long-range transport of pollutants in the atmosphere, thermal pollution in river systems, and flow in porous media (Gurarslan et al. 2013).

In this study, the concentration transport was investigated in laminar flow as a fundamental study. The ADE equation in the two-dimensional case for laminar flow is defined as (Herleman and Rumer 1963):

$$\frac{\partial C}{\partial t}+u\frac{\partial C}{\partial x}+v\frac{\partial C}{\partial y}=D_m\left[\frac{\partial^2 C}{\partial x^2}+\frac{\partial^2 C}{\partial y^2}\right] \tag{2.2}$$

where the molecular diffusion coefficient or molecular diffusivity along the x-axis (D_m) is 1×10^{-9} (m^2/s) and C is the concentration.

The insight gained from the tracer snapshots enhances the qualitative understanding, but it is still difficult to make quantitative comparisons between different models. A technique that is often used is to inject a tracer at the inlet and monitor the outlet tracer concentration over time (Hart 1979). The simplest way to determine the residence time distribution is to measure the system response for a short tracer pulse. If the system is closed, i.e., no back-mixing occurs at the process entrance and exit, the measured tracer concentration curve, when scaled to unity, is the residence time distribution

(RTD). The RTD is commonly measured by tracer injection into the feed stream at time t=0 and then the tracer concentration C is measured in the exit stream as a function of time. In a pulse input, an amount of tracer is injected into the system in a short time interval. The outlet concentration is then measured as a function of time. The concentration of the tracer is recorded at the outlet until it recedes sufficiently close to zero. This results in the flow-through curve (FTC) of the system. By using the transient tracer concentration at the outlet of system C_{out}, the Danckwerts *F* cumulative curve was obtained (Danckwerts, 1953):

$$F(t)=\frac{C_{out}(t)}{\sum_{i=1}^{n} C_{out\text{-}i}} \tag{2.3}$$

where *F(t)* represents the cumulative distribution function. *F* curve reaches the asymptotic value of 1 for very long times. The residence time distribution (RTD) function could then be calculated as (Danckwerts, 1953):

$$E(t)=\frac{dF(t)}{dt} \tag{2.4}$$

where *E(t)* is calculated using an average of the forward and backward derivative of the *F(t)* values at a particular time.

Important variables and relationships can be obtained directly from FTC curve. As the relationship between a cumulative distribution and probability density functions, the RTD curve may be obtained from the FTC by the following relationship between the two (Carlston 2015):

$$RTD(t)=\frac{1}{T_r}\int_0^t FTC(t)dt \tag{2.5}$$

where *Tr* is the release time for the pulse input.

Although the performance of the unit can be assessed directly from the comparison of FTC curves, the direct interpretation of these functions is not always a simple task. Therefore, some hydraulic indexes are usually extracted from these functions so that the analysis can become less qualitative. The hydraulic indexes are usually used as short-circuiting and mixing indicators. The indicators used are used to assess the hydraulic efficiency of the system are listed in Table 2.3.

Table 2. 3. The indicators commonly used for the evaluation of RTD curves (Demirel and Aral 2018, Nuruzzaman et al. 2021, Teixeira and do Nascimento Siqueira 2008)

Phenomena	Performance Indicator	Description of indicator
Short-circuiting	θ_{10}	θ_{10} denotes the time in which 10% of the injected tracer has reached the outlet. A low θ_{10} value is normally associated with a short circuit between the inlet and the outlet.
	θ_{25}	θ_{25} denotes the time in which 25% of the injected tracer has reached the outlet.
	θ_{50}	The time necessary for 50% of the mass of the tracer that was injected at the inlet section to reach the outlet of the unit
	θ_{75}	θ_{75} denotes the time in which 75% of the injected tracer has reached the outlet.
	θ_{90}	θ_{90} denotes the time in which 90% of the injected tracer has reached the outlet. Large stagnant zones are normally associated with high θ_{90} values.
	θ_f	Time at which the tracer is first observed at the outlet
	S_{10}	Short-circuiting index, $S_{10}=1-\frac{t_{10}}{t_{HRT}}$
	S_{50}	Short-circuiting index, $S_{50}=1-\frac{t_{50}}{t_{HRT}}$
	t_{HRT}	Nominal hydraulic residence time (Theoretical residence time), $t_{HRT}=\frac{V_m}{Q}$, (V_m = volume of water body, Q = inflow rate)
Mixing	M_{90-10}	Time elapsed between t_{10} and t_{90}, $M_{90}-M_{10}=\frac{t_{90}-t_{10}}{t_{HRT}}$

$M_{75\text{-}25}$	Time elapsed between t_{25} and t_{75}, $M_{75}-M_{25}=\frac{t_{75}\text{-}t_{25}}{t_{HRT}}$
MI	The ratio between the time necessary to 10% and 90% of the mass of the tracer that was injected at the inlet section to reach the outlet of the unit, ($MI=\frac{\theta_{90}}{\theta_{10}}$)

While those indicators were widely applied to study flow and concentration field in chemical, water and wastewater engineering (Teixeira and do Nascimento Siqueira 2008, Demirel and Aral 2018, Nuruzzaman et al. 2021), it is difficult to identify a standard value of those indicators for the BFSF. In this study, modeling the flow and concentration transport in step-like geometries with the presence of cylindric obstacles is carried out to understand the transport process.

The transport of solute in complex geometries such as a backward-facing step and a cylinder is an important area of research. While many studies have investigated the flow and turbulence characteristics of these geometries, there has been limited attention given to solute transport. However, the motion of pollutants or nutrients in aquatic environments is of great concern in environmental hydraulics. Understanding the transport processes in these geometries is critical for predicting the impact of solute transport on aquatic ecosystems and the effectiveness of mitigation strategies.

As highlighted in the literature review, there are important gaps in the knowledge of the hydrodynamic processes related to the presence of a cylinder in recirculating zones. Past studies have mostly focused on heat transfer and magnetohydrodynamics, with limited attention given to the transport of solutes. Furthermore, the presence of cylindric obstacles, such as plants, in simple rectangular channels has been extensively studied, but the transport of substances in these geometries has not been fully investigated.

The importance of solute transport in environmental hydraulics is underscored by its relevance in various applications, such as the management of pollutants in rivers, lakes, and coastal zones. Understanding the transport processes in complex geometries can lead to the development of more effective and efficient mitigation strategies for environmental problems. Therefore, investigating the transport of solutes in the presence of a backward-facing step and a cylinder is an important research area that requires further attention. The concentration fields and their evolution over time are critical for predicting the impact of solute transport on aquatic ecosystems and the effectiveness of mitigation strategies

Chapter 3 Materials and Methods

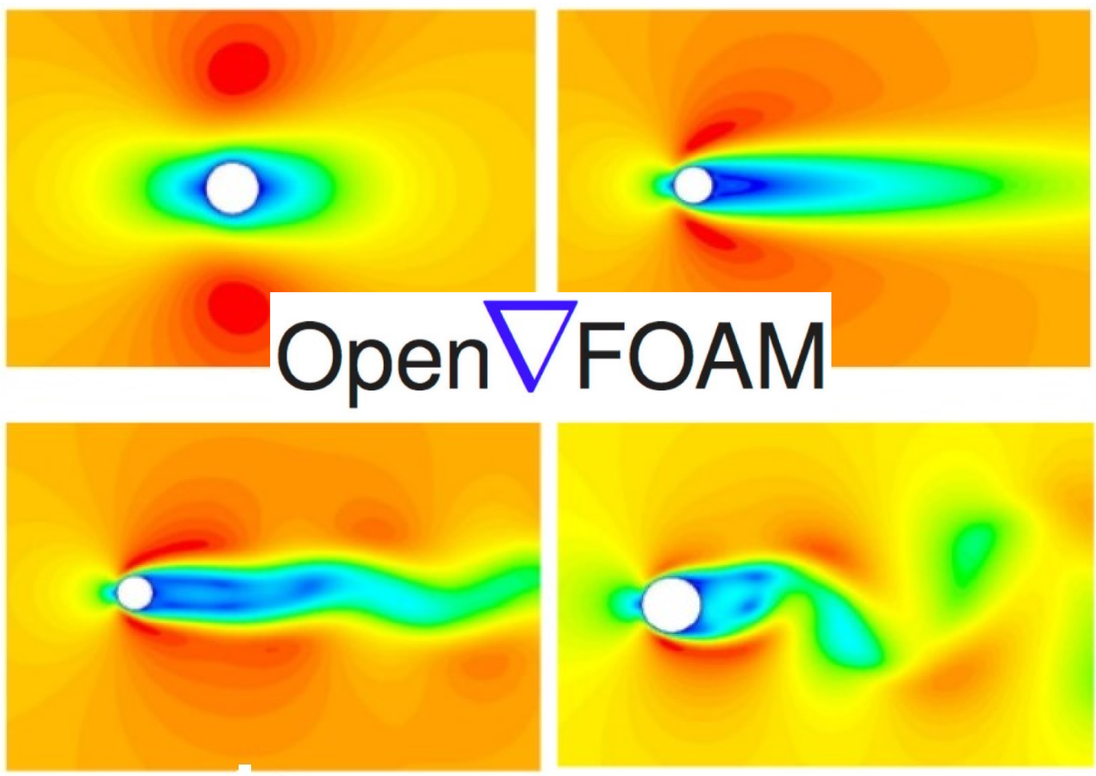

This chapter describes a numerical model used in this thesis. Numerical simulations were carried out with the open-source CFD toolbox OpenFOAM.

3.1. Numerical model

Computational Fluid Dynamics (CFD) is increasingly used to study a wide variety of complex Environmental Fluid Mechanics (EFM) processes. However, the accuracy and reliability of CFD modeling and the correct use of CFD results can easily be compromised (Blocken and Gualtieri 2012). OpenFOAM (Open-Source Field Operation and Manipulation) offers considerable advantages for CFD simulations. It is open source; therefore, the user has access to the source code and can modify the code for individual use. Numerical simulations were performed using OpenFOAM V-2112. It is a library of object-oriented software written in the C++ programming language. It is free of charge, and the ability to run in parallel over large processor arrays makes it attractive for simulations. The (initial) disadvantages of the software, however, are that there is limited documentation (other than access to the code itself), and for a user, without prior knowledge of C++, there is a steep learning curve. One of the strengths of OpenFOAM is that new solvers and utilities can be created by its users with some pre-requisite knowledge of the underlying method, physics, and programming techniques involved. In addition to the solvers, OpenFOAM also has a large number of utilities for pre-processing and post-processing of results. The overall structure of OpenFOAM is shown in Figure 3.1.

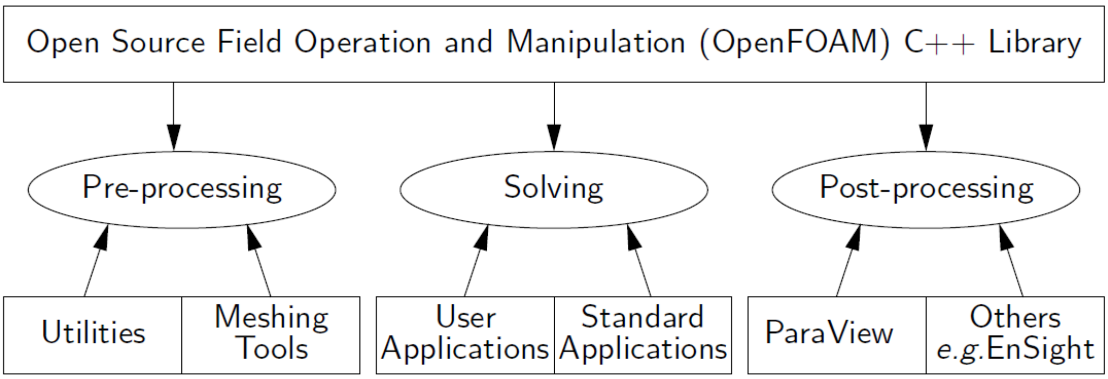

Figure 3.1. Overview of OpenFOAM structure (user guide OpenFOAM V-2112)

In the present study, several numerical simulations were performed. The overall steps of numerical modeling of this study are illustrated in Figure 3.2.

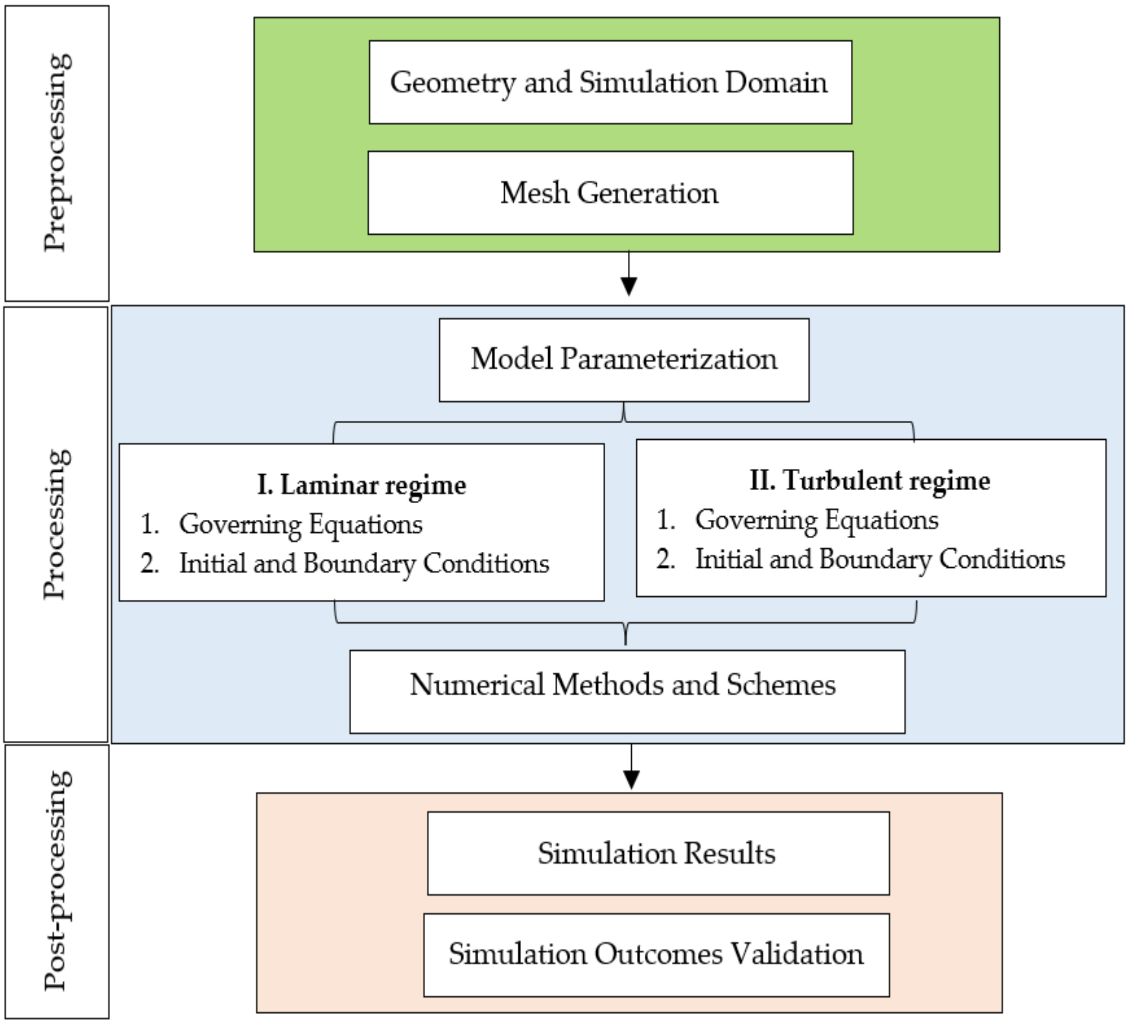

Figure 3.2. Flowchart of the numerical modeling procedures in this study.

3.2. Geometry and simulation domain

During the preprocessing phase of the CFD modeling, the geometry and domain for the mesh were created. In OpenFOAM, geometries for internal flows are typically created using a meshing tool, known as blockMesh, which creates fully structured hexahedral meshes.

In this study, for validation, a two-dimensional classical backward-facing step namely BFSF 1, was considered, following the geometry experimentally studied by Armaly et al. (1983) and Wang et al. (2019) with an expansion ratio ($ER=h_2/h_1=2$). The computational domain of the present study consists of a total longitudinal length of 56h (L_u=6h, L_d=50h), and L_u and L_d are respectively, the length upstream and downstream of the step. Based on Biswas et al. 2004, the distance of five times the channel height upstream of the step ($L_u \geq 5h_1$, $h_1=h$) was verified to be sufficient. At the outlet of the computational domain, the flow was fully developed. The sketch of the BFSF is presented in Figure 3.3.

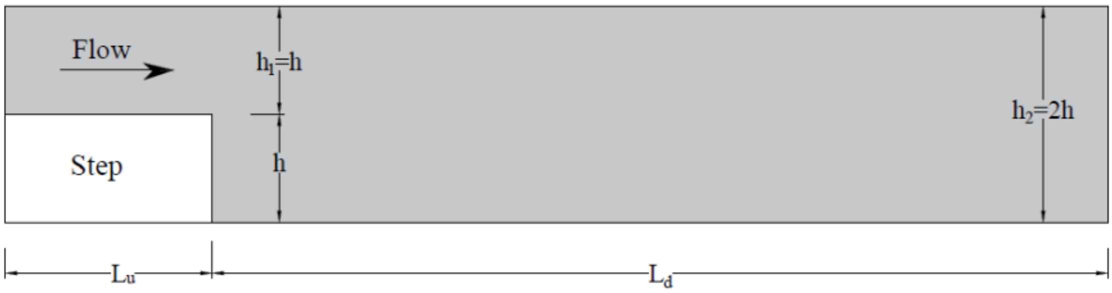

Figure 3.3. Sketch of backward-facing step (BFSF) (not to scale). h, h_1, and h_2 represent the step height, inlet-section height, and outlet-section height, respectively. L_u and L_d are length upstream of step and downstream of step.

In this study, the structured rectangular hexahedral mesh was considered. Structured meshing is generally more straightforward to implement, faster to execute, and tends to be more accurate than unstructured ones (Biswas and Strawn 1998). Moreover, structured meshes require more regular memory access; consequently, the latency during simulations is lower (Keyes et al. 2000). To ensure the validity and accuracy of the solution scheme, several grid sizes were examined. Mesh independence was assessed and validated using experimental data. Meshes of different sizes were applied, and the reattachment lengths were compared to the corresponding experimental data (Armaly et al. 1983). The sensitivity of the model to certain parameters was extensively discussed. The test of the grid independence was performed by computing the dimensionless reattachment length (Lr/h), in a Re_h =544 for five different grids (see Table 3.1). It was found that the computed results were independent of the number of grid points and the relative error between the fourth and fifth grid was very small and could be neglected to decrease effort and computational time. When predicting the reattachment length, it was noted that the difference between Mesh 5 and Mesh 4 was only 0.5%, which was relatively small. However, when compared to the experimental data, the difference was much larger, reaching 15%. Given the accuracy and duration of the computation, a total number of 129,200 cells were selected.

Table 3. 1. Grid independence test results

Grid No.	Number of cells	Lr/h	Differences with experimental data
Mesh 1	86,000	10.77	22.95 %
Mesh 2	95,200	11.2	19.9 %
Mesh 3	104,000	11.5	17.76 %
Mesh 4	129,200	11.81	15.56 %
Mesh 5	132,000	11.82	15.49 %

The cell size near the walls and step was fine to have enough resolution. The mesh was gradually refined toward the bottom and step, as shown in Figure 3.4, to enhance the accuracy near the bottom wall to ensure that the dimensionless distance (y+) remained within the viscous sublayer. As well, the mesh was refined near the cylinder to resolve properly the separation of boundary layers.

Figure 3.4. General view of the grid and zoom of the grid near the bottom wall

In this study, the classical BFSF geometry was modified by adding a cylinder placed at different locations downstream of the step in the laminar and turbulent flow. A two-dimensional backward-facing step with a cylinder, namely BFSF 2, was considered following the geometry of BFSF 1.

As the BFSF 1, the structured rectangular hexahedral mesh was considered for BFSF 2. Figure 3.5 shows the computational mesh with decreasing cell size towards the walls and near the cylinder.

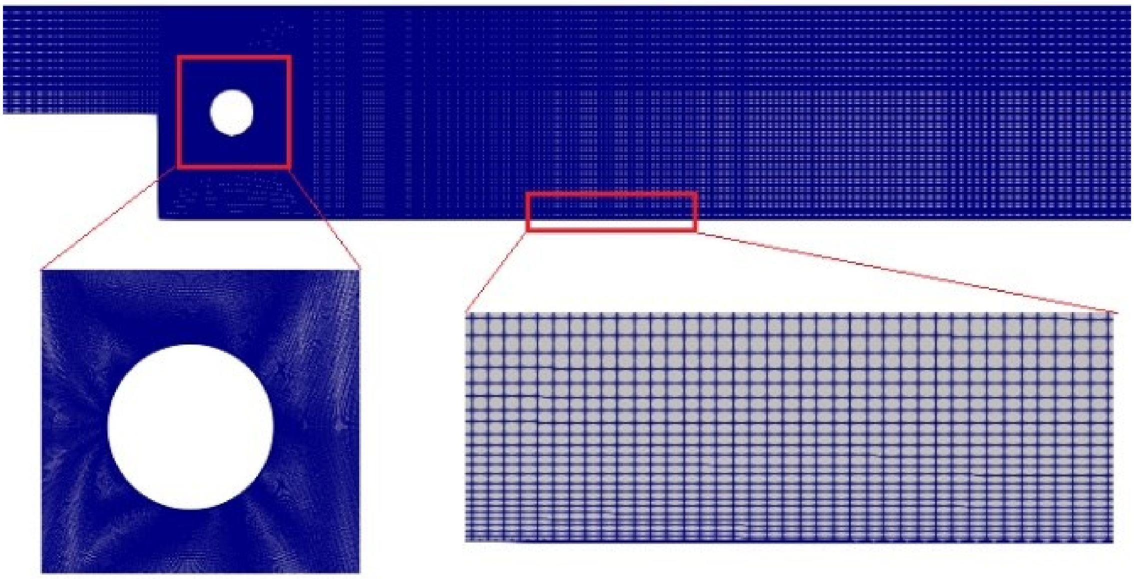

Figure 3.5. The general view of the grid and zoom of the grid in the vicinity of the cylinder and bottom wall

Mesh independence was checked for BFSF 2 by comparison of the dimensionless reattachment lengths Lr_1/h and Lr_3/h, in a Re_h =544 at five different sizes (see Table 3.2). It was found that the computed results were independent of the number of cells. The aim was to keep the cell numbers of BFSF 2 close to that of BFSF1 (129,200). The mesh resolution of BFSF 1 was chosen to account for the cylinder and provide consistent results for comparison. A total number of 129,600 cells was selected.

Table 3. 2. Grid independence test results for BFSF 2 (Lr_1 and Lr_3 are primary and third reattachment lengths at bottom wall)

Grid No.	Number of Cells	Lr_1/h	Lr_3/h
Mesh 1	72,000	0.815	17.15
Mesh 2	104,400	0.832	17.30
Mesh 3	129,600	0.855	17.50
Mesh 4	132,600	0.860	17.55
Mesh 5	148,500	0.865	17.60

3.3. Model parameterization

For the simulation, water with density ρ=997 kg/m^3 and dynamic viscosity (μ) 8.905×10^{-4} Pa.s was selected as fluid. The Reynolds number based on the step height (h) was defined as $Re_h = \frac{Uh}{\upsilon}$. According to Armaly et al. (1983), in the BFSF, the laminar flow occurs for step-height Reynolds numbers $Re_h < 900$, the transitional flow is in the range $900 < Re_h < 4{,}950$, and the turbulent flow is $Re_h > 4{,}950$. The present study was carried out in the Reynolds number range covering laminar and turbulent flows.

3.4. Laminar flow

3.4.1. Governing equations

Mass and momentum equations for two-dimensional (2D) laminar flow for an incompressible fluid isothermal fluid (with constant density) can be written as:

Mass equation

$$\frac{\partial u}{\partial x}+\frac{\partial v}{\partial y}=0 \tag{3.1}$$

Momentum equation

$$\begin{aligned}\left(\frac{\partial u}{\partial t}+u\frac{\partial u}{\partial x}+v\frac{\partial u}{\partial y}\right) &= g_x-\frac{1}{\rho}\frac{\partial p}{\partial x}+\upsilon\left(\frac{\partial^2 u}{\partial x^2}+\frac{\partial^2 u}{\partial y^2}\right)\\ \left(\frac{\partial v}{\partial t}+u\frac{\partial v}{\partial x}+v\frac{\partial v}{\partial y}\right) &= g_y-\frac{1}{\rho}\frac{\partial p}{\partial y}+\upsilon\left(\frac{\partial^2 v}{\partial x^2}+\frac{\partial^2 v}{\partial y^2}\right)\end{aligned} \tag{3.2}$$

where υ = kinematic viscosity; p = pressure; u and v = velocity components in the x and y directions; and g = acceleration of gravity.

3.4.2. Initial and boundary conditions

Boundary conditions were assigned at the inlet, the outlet, and the walls. A parabolic velocity profile was assigned to the inlet. A summary of these boundary conditions which were used for the laminar flow is given in Figure 3.6.

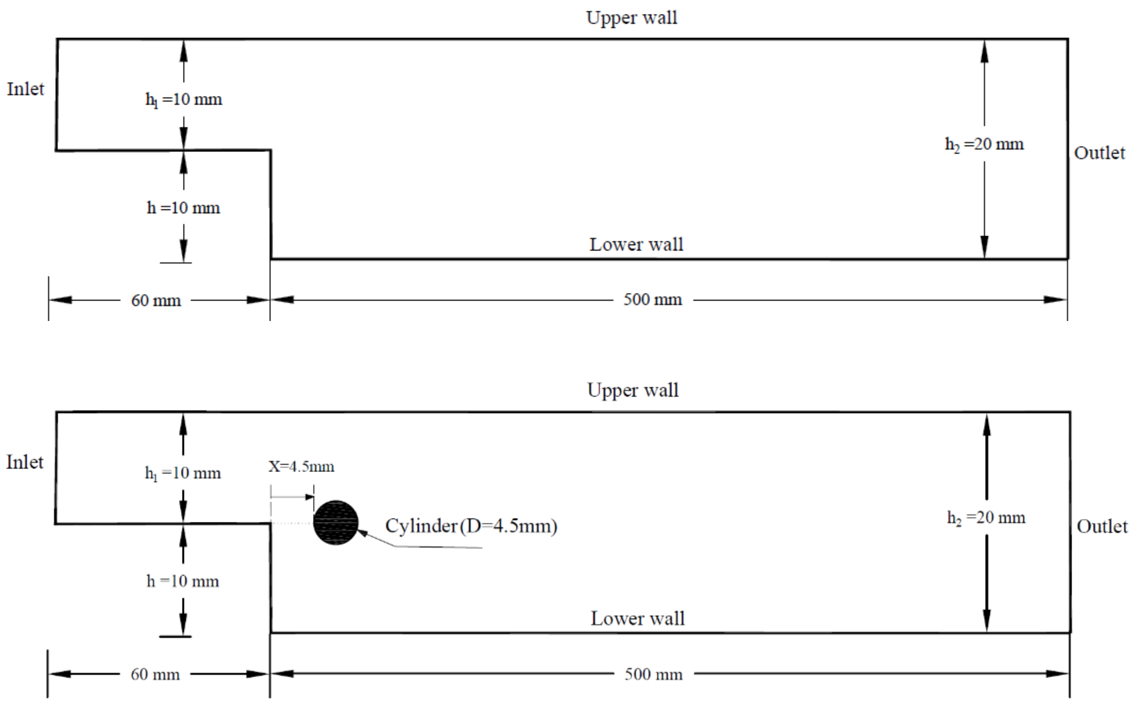

Boundary type description	inlet	outlet	Wall (upper wall, bottom wall, cylinder)
Pressure (p)	zeroGradient	fixedValue	zeroGradient
Velocity (u)	fixedValue	zeroGradient	noSlip

Figure 3.6. Boundary conditions of the backward-facing step in the laminar flow

3.4.3. Numerical methods and numerical schemes

A transient solver icoFoam was used for the laminar flow. The governing equations were discretized based on the finite-volume method (FVM). The numerical integration was conducted by using the pressure-implicit with the splitting of operators (PISO) algorithm. PISO is a pressure-velocity calculation procedure for the Navier–Stokes equations. The time term was discretized by using second-order backward and Euler schemes. In the laminar flow, the terms of the equations are discretized by using a Gaussian linear scheme in all cases. To ensure convergence to the numerical solutions, all residuals were required to be dropped below a value of 10^{-6}. Moreover, to ensure the stability of simulations, time steps were automatically modified, so that maximum Courant numbers always remained below 0.8.

3.5. Turbulent flow

3.5.1. Governing equations and turbulence modeling

The most widely applied approach to simulate a turbulent flow is based on the time averaging, herein, Reynolds-Averaging Navier-Stokes (RANS) equations. OpenFOAM offers a large range of methods and models to simulate the turbulence, including the RANS. RANS mass and momentum conservation laws for two-dimensional flow for an incompressible isothermal fluid (with constant density) can be written as:

Mass equation

$$\frac{\partial \bar{u}}{\partial x} + \frac{\partial \bar{v}}{\partial y} = 0 \tag{3.3}$$

Momentum equation

$$\begin{aligned} \frac{\partial \bar{u}}{\partial t} + \bar{u}\frac{\partial \bar{u}}{\partial x} + \bar{v}\frac{\partial \bar{u}}{\partial y} &= g_x - \frac{1}{\rho}\frac{\partial \bar{p}}{\partial x} + \upsilon\nabla^2\bar{u} + \frac{\partial}{\partial x}(\upsilon_t\frac{\partial \bar{u}}{\partial x}) + \frac{\partial}{\partial y}(\upsilon_t\frac{\partial \bar{u}}{\partial y}) \\ \frac{\partial \bar{v}}{\partial t} + \bar{u}\frac{\partial \bar{v}}{\partial x} + \bar{v}\frac{\partial \bar{v}}{\partial y} &= g_y - \frac{1}{\rho}\frac{\partial \bar{p}}{\partial y} + \upsilon\nabla^2\bar{v} + \frac{\partial}{\partial x}(\upsilon_t\frac{\partial \bar{v}}{\partial x}) + \frac{\partial}{\partial y}(\upsilon_t\frac{\partial \bar{v}}{\partial y}) \end{aligned} \tag{3.4}$$

where $\bar{p}$ = mean fluid pressure; $\bar{u}$ and $\bar{v}$ = mean velocity components; υt = turbulent eddy kinematic viscosity.

The simplest RANS models are based on the concept of the eddy viscosity (υ_t) introduced by Boussinesq in 1887 (Nguyen et al. 2018), giving a relation between the Reynolds stress tensor and the average velocity gradient tensor (Viti et al. 2018). Different turbulence models estimate υ_t based on different turbulent variables. In this study, four RANS turbulence models, such as standard k-ε, RNG k-ε, standard k-ω, and SST k-ω were comparatively applied.

The standard k-ε model is the most widely applied turbulence model. It is a two-equation model that includes two extra transport equations to represent the turbulent properties of the flow: the turbulent kinetic energy (k) and the turbulent energy dissipation (ε), together with a specification for the eddy viscosity (υ_t). Its formulation is presented as (Launder and Spalding 1972):

$$\frac{\partial k}{\partial t}+\bar{u}_j\frac{\partial k}{\partial x_j}=\frac{\partial}{\partial x_j}[(\upsilon+\frac{\upsilon_t}{\sigma_k})\frac{\partial k}{\partial x_j}] - \upsilon_t\frac{\partial \bar{u}_i}{\partial x_j}(\frac{\partial \bar{u}_i}{\partial x_j}+\frac{\partial \bar{u}_j}{\partial x_i})-\varepsilon \tag{3.5}$$

$$\frac{\partial \varepsilon}{\partial t}+\bar{u}_j\frac{\partial \varepsilon}{\partial x_j}-\frac{\partial}{\partial x_j}[(\upsilon+\frac{\upsilon_t}{\sigma_\varepsilon})\frac{\partial \varepsilon}{\partial x_j}]= C_1\frac{\varepsilon}{k}\upsilon_t\frac{\partial \bar{u}_i}{\partial x_j}(\frac{\partial \bar{u}_i}{\partial x_j}+\frac{\partial \bar{u}_j}{\partial x_i})-C_2\frac{\varepsilon^2}{k} \tag{3.6}$$

$$\upsilon_t = \rho C_\mu\frac{k}{\varepsilon} \tag{3.7}$$

where k = turbulent kinetic energy; ε = turbulent kinetic energy dissipation rate, whereas C_1, C_2, C_μ, σ_k, and σ_ε are constants, and their values are listed in Table 3.3 (Launder and Spalding 1972).

Table 3.3. Values of the constants of the standard k-ε model (Launder and Spalding 1972)

Constant	C_1	C_2	C_μ	σ_k	σ_ε
Value	1.44	1.92	0.09	1	1.3

The RNG k-ε model was developed using Re-Normalization Group (RNG) methods by Yakhot and Orszag (1986) to renormalize the Navier-Stokes equations. The RNG version adds a term for the ε equation, which is known to be responsible for differences in its performance. It is a two-equation transport model for k and ε. The RNG k- ε model formulation differs from that of the standard k- ε in the values of the parameters. The standard k-ω model is a two-equation model developed by Wilcox in 1998, with an approach similar to the k-ε model. It applies the same expression for the turbulent kinetic energy k but it considers the rate of dissipation of energy per unit volume and time, called the specific dissipation rate ω, instead of the turbulent energy dissipation (ε). In the k-ω model, the turbulent viscosity is computed by (Wilcox 1998):

$$\upsilon_t = \frac{k}{\omega} \tag{3.8}$$

The shear stress transport (SST) k-ω model is a two-equation eddy-viscosity model. It is similar to the standard k-ω although the former includes several improvements and other constant variables. It is a hybrid model combining the k-ω and the k-ε models. This method effectively blends the accurate formulation of the k-ω model in the near-wall region with the free-stream independence of the k-ε model in the far-field region, away from the wall. The SST formulation switches to a k-ε behavior in the free-stream and thereby avoids the common k-ω problem that the model is too sensitive to the inlet free-stream turbulence properties.

3.5.2. Initial and boundary conditions

In turbulent flow, the standard k-ε, RNG k-ε, standard k-ω, and SST k-ω turbulence models were employed. The Reynolds number based on the step height (h) was Re_h=9,000.

The initial values of turbulent kinetic energy (k) and dissipation rate (ε) can be estimated by Launder and Spalding (1972):

$$k = \frac{3}{2} \left(|u_{reff}| T_i\right)^2 \tag{3.9}$$

$$\varepsilon = \frac{0.09^{0.75} k^{1.5}}{l} \tag{3.10}$$

where u_{reff} = inlet flow velocity (m/s); l = 0.07L (L = characteristic inlet scale (m)); T_i = turbulent intensity (5%). In omega-based models, the initial value of the specific dissipation rate ω can be estimated by:

$$\omega = \frac{k^{0.5}}{0.09^{0.25} l} \tag{3.11}$$

Initial values for pressure (p = 0) and velocity (U = 0.801 m/s) were used. Also, the initial values of turbulence quantities were calculated using equations 3.9-3.11: k = 0.002406 m^2/s^2, ε = 0.0277 m^2/s^3, ω = 124.82 l/s.

Boundary conditions were assigned at the inlet, the outlet, and the walls. A summary of these boundary conditions which were used for the turbulent flow is given in Table 3.4.

Table 3. 4. Boundary conditions of the BFSF 1 and BFSF 2 in the turbulent flow

Boundary type description		**inlet**	**outlet**	**upper wall / bottom wall / cylinder**
Pressure	P (kg /s.m2)	zeroGradient	fixedValue	zeroGradient
Velocity	u (m/s)	fixedValue	inletOutlet	noSlip
Turbulence fields	k (m^2/s^2)	fixedValue	zeroGradient	kqRWallFunction
	ε (m^2/s^3)	fixedValue	zeroGradient	epsilonWallFunction
	ω (1/s)	fixedValue	zeroGradient	omegaWallFunction

3.5.3. Numerical methods and numerical schemes

A transient solver pisoFoam was used for the laminar flow. The governing equations were discretized based on the finite-volume method (FVM). The numerical integration was conducted using the PISO (Pressure-Implicit with

Splitting of Operators) algorithm. The time term was discretized using second order backward and Euler schemes. The discretization schemes for the turbulence kinetic energy (k), turbulent kinetic energy dissipation rate (ε), and specific dissipation rate (ω) were implemented using a Gauss upwind scheme. To ensure convergence to the numerical solutions, all residuals were required to be dropped below a value of 10^{-6}. Also, to ensure the stability of simulations, time steps were automatically modified, so that, maximum Courant numbers always remained below 0.8.

3.6. Summary of numerical simulation models

In this study, the Reynolds number based on the step height (h) was defined as $Re_h = \frac{Uh}{\upsilon}$ (where h is step height, U is inlet velocity) and the Reynolds number based on cylinder diameter (D) was calculated as $Re_D = \frac{UD}{\upsilon}$. The present study was carried out for a step-height Reynolds number in the range of 75 to 9,000, covering both laminar and turbulent flow (Figure 3.7). Table 3.5 lists the values of Reynolds numbers that were tested in this study.

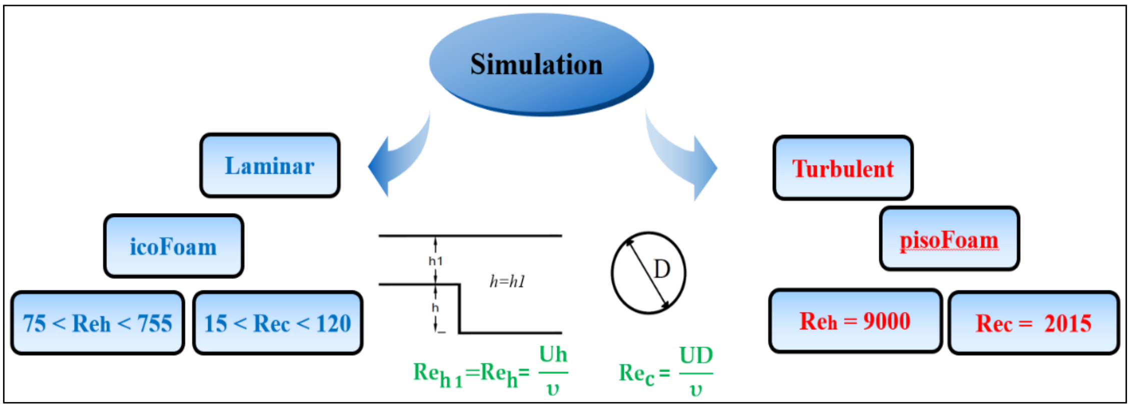

Figure 3.7. Flowchart of the numerical simulations

Table 3. 5. The range of Reynolds numbers based on step height (Re_h) and cylinder diameter (Re_D)

Reh (step height)	75	158	336	420	544	672	755	9,000
Re_D (cylinder diameter)	15	28	55	70	87	108	120	2,015

3.6.1. Laminar flow tests

Laminar backward-facing step flow was investigated for a wide range of step-height Reynolds numbers $75 \leq Re_h \leq 755$. Table 3.6 shows all Runs for classical backward-facing step flow.

Table 3. 6. Runs and Reynolds numbers based on step height (Re_h) and cylinder diameter (Re_D) in the classical backward-facing step laminar flow

Run	**Re_h (step height)**	**Re_D (cylinder diameter)**
BFSF 1 – L1	75	15
BFSF 1 – L2	158	28
BFSF 1 – L3	336	55
BFSF 1 – L4	420	70
BFSF 1 – L5	544	87
BFSF 1 – L6	672	108
BFSF 1 – L7	755	120

A cylinder with a diameter (D) was set at one cylinder-diameter distance from the step edge (x=D) in the x-direction. The top half of the cylinder was above the top surface (mid-plane) of the step. The sketch of BFSF with a cylinder in the laminar flow is presented in Figure 3.8. Table 3.7 lists all Runs in laminar flow over backward-facing step flow.

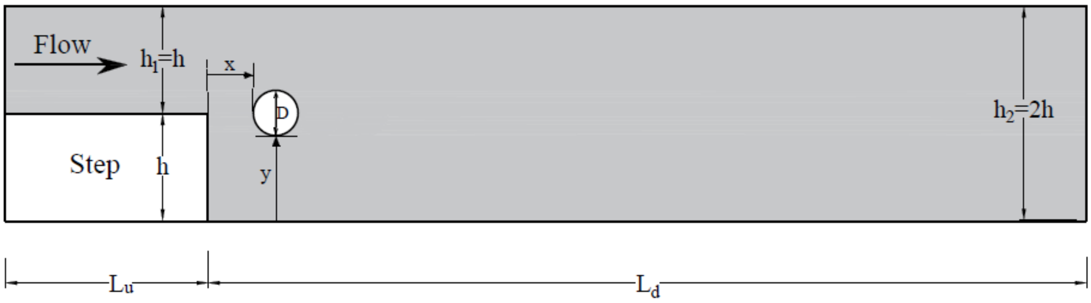

Figure 3.8. Sketch of BFSF with a cylinder in laminar flow simulations (BFSF 2) (not to scale). D is cylinder diameter and its location from step. x represents the distance of cylinder from step in x-direction and y represents the distance of cylinder from bottom wall in y-direction.

Table 3. 7. Runs and Reynolds numbers based on step height (Reh) and cylinder diameter (ReD) in laminar flow in the backward-facing step flow with a cylinder.

Run	Re_h (step height)	Re_D (cylinder diameter)	x	y
BFSF 2 – L1	75	15	1 D	$h-\frac{D}{2}$
BFSF 2 – L2	158	28		
BFSF 2 – L3	336	55		
BFSF 2 – L4	420	70		
BFSF 2 – L5	544	87		
BFSF 2 – L6	672	108		
BFSF 2 – L7	755	120		

3.6.2. Turbulent flow tests

In turbulent flow, the standard k-ε, RNG k-ε, standard k-ω, and SST k-ω turbulence models were employed. The Reynolds numbers based on the step height (h) and cylinder diameter (D) were Re_h=9,000 and Re_D=2,015, respectively. Table 3.8 lists all Runs in turbulent flow over backward-facing step flow.

Table 3. 8. Runs of turbulent flow over the classical backward-facing step at different turbulence models.

Run	Re_h (step height)	Turbulence model
BFSF 1 – T1	9,000	Standard k-ε
BFSF 1 – T2	9,000	RNG k-ε
BFSF 1 – T3	9,000	Standard k-ω
BFSF 1 – T4	9,000	SST k-ω

The standard k-ε model was used for the study of the effect of a cylinder placed downstream of the step. To understand the effect of a cylinder on step flow, a cylinder at different horizontal and vertical locations downstream of the step was considered. Two series of numerical tests were carried out. In series (I), a cylinder with a diameter (D) was set at a different distance from the step edge, in the x-direction. The top half of the cylinder was above the top surface (mid-plane) of the step. In series (II), a cylinder was set at one cylinder-diameter distance from the step edge at different locations in the y-direction. The sketch of the BFSF and its configurations in the turbulent flow is presented in Figure 3.9. Table 3.9 shows Runs of turbulent flow over backward-facing step flow with the cylinder.

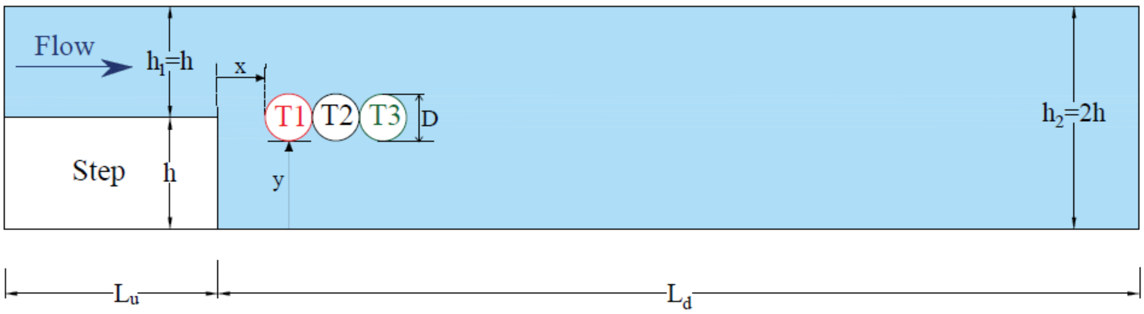

(a)

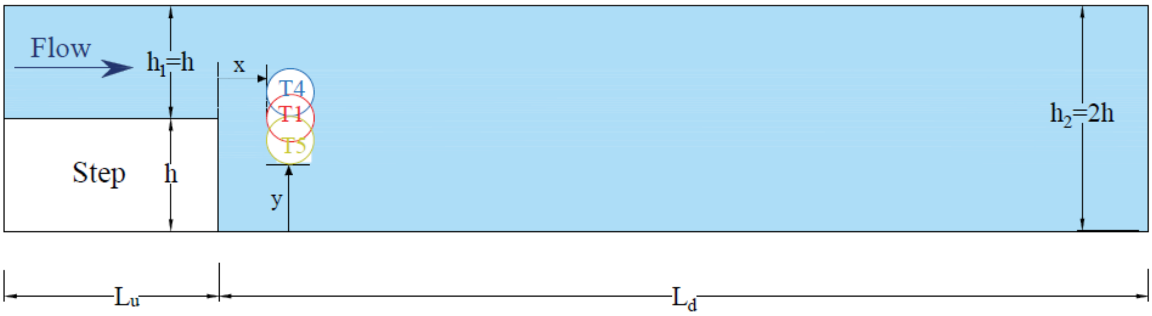

(b)

Figure 3.9. Sketches of the BFSF with a cylinder in turbulent flow simulations (not to scale). (a) Cylinder was set at a different distance from the step edge in the x-direction (b) Cylinder was set at one cylinder-diameter distance from the step edge at different locations in the y-direction

Table 3. 9. Configurations and Runs of turbulent flow over backward-facing step with cylinder. x represents the distance of cylinder from step in x-direction and y represents the distance of cylinder from bottom wall in y-direction.

Run	**Re_h (step height)**	**Re_D (cylinder diameter)**	x	y
BFSF 2 – T1	9,000	2,015	1 D	$h-\frac{D}{2}$
BFSF 2 – T2	9,000	2,015	2 D	$h-\frac{D}{2}$
BFSF 2 – T3	9,000	2,015	3 D	$h-\frac{D}{2}$
BFSF 2 – T4	9,000	2,015	1 D	h
BFSF 2 – T5	9,000	2,015	1 D	h-D

Chapter 4 Validation of the Numerical Simulations

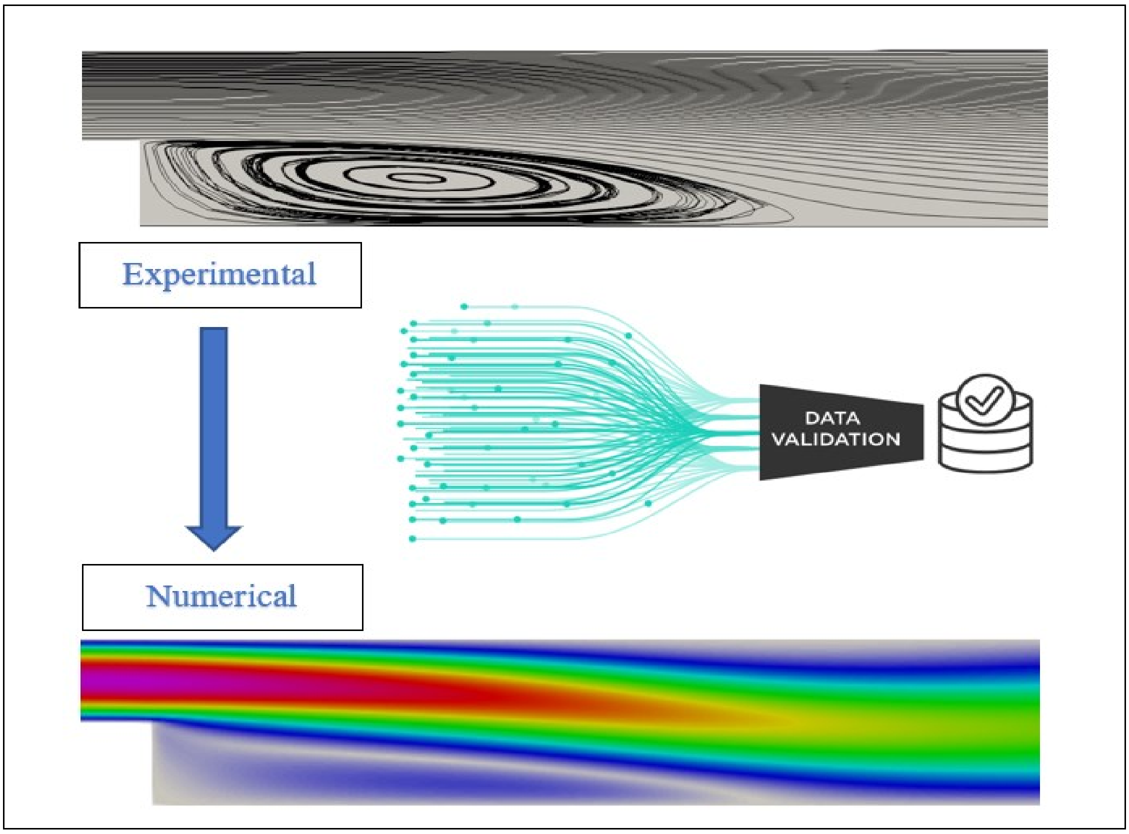

In this chapter, the classical two-dimensional classical backward-facing step is validated with available literature data using CFD code OpenFOAM.

4.1. Introduction

During the last decades, computer simulations of physical processes have been used in scientific research and the analysis and design of engineered systems. Computational fluid dynamics (CFD) simulations are used to improve understanding of fluid physics. Nowadays, computational simulation is used to solve problems not only to find a solution but also to ensure quality. Validation is the assessment of the accuracy and reliability of a computational simulation by comparison with experimental data (Roache 1997, 2009). Several experimental studies have been performed to examine the influence of backward-facing step geometry in laminar and turbulent flow. In the present study, two-dimensional numerical simulations were performed using the open-source code OpenFOAM. This chapter presents a validation procedure for CFD simulations of flow over a backward-facing step (BFSF). Flow characteristics such as reattachment, recirculation zone, velocity profile, skin friction coefficient, and pressure coefficient were validated in laminar and turbulent flow using available experimental data.

4.2. Laminar flow

4.2.1. Recirculation zone and reattachment length

The most important characteristics of the backward-facing step flow are separation and reattachment. The adverse pressure gradient due to the sudden expansion at the edge of the step caused flow separation. A sketch of the 2D backward-facing step flow is shown in Figure 4.1.

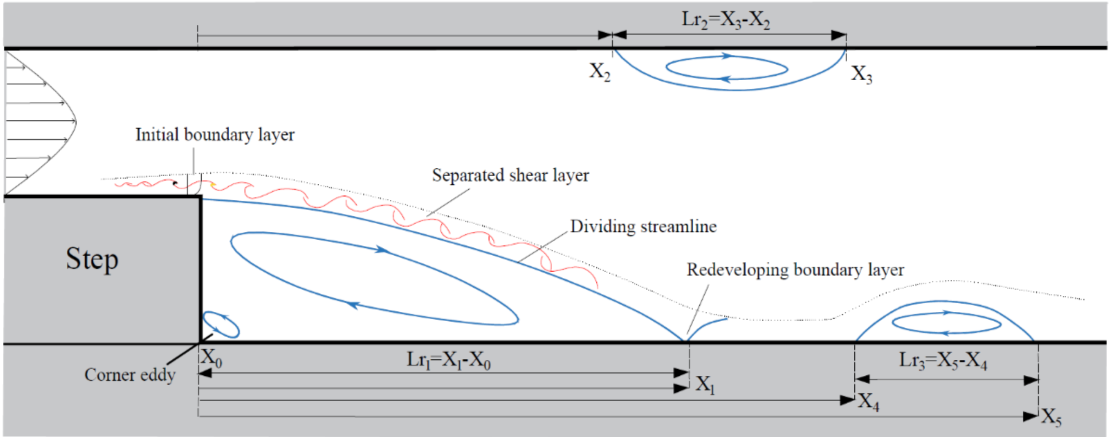

Figure 4.1. Sketch of the flow over the classical backward-facing step

In the classical BFSF, the flow pattern involves several different flow regions: initial boundary layer, separated free shear layer, corner eddy, primary recirculation zone on the bottom wall, second recirculation zone on the upper wall, redeveloping boundary layer, and third recirculation zone on the bottom wall, as shown in Figure 4.1. The physics of separation regions could be described as follows: flow separated at the step (X_0) and reattached to the bottom wall (X_1). This is the primary recirculation zone having a length of Lr_1, which increased as Re_h increased. In addition to the primary recirculation zone (Lr_1), a second recirculation zone (Lr_2) near the upper wall for $Re_h > 300$ was reported in previous studies (Armaly et al. 1983). Point X_2 shows the starting location of the second recirculation zone and point X_3 is its corresponding end on the upper wall. Erturk (2008), found that with an expansion ratio of 2 for $Re_h > 1{,}275$, a third recirculating zone (Lr_3) was observed between points X_4 and X_5 with length Lr_3. Its length Lr_3 increased as Re_h increased. However, Armaly et al. (1983) found that the third recirculation region (Lr_3) was in the early part of the transitional flow, and it was not observed for $Re_h > 1{,}725$. Cherdron et al. (1978) and Sparrow and Kalejs (1977), suggested that the third recirculation zone was caused by vortex shedding from the edge of the step. These vortices were thought to approach the wall, and the third recirculation zone might be due to the sharp change of flow direction that eddies experience (Armaly et al. 1983). Table 4.1 lists the value of the normalized location of starting and ending recirculation zones in the BFSF.

Table 4. 1. The reattachment and separation points of the recirculation zones in laminar flow (X_1 is a point that primary recirculation reattached to the bottom wall, X_2 is starting point of the second recirculation zone at upper wall and X_2 is ending point of second recirculation zone at upper wall)

Run	X_1/h	X_2/h	X_3/h
BFSF 1–L1	2.88	-	-
BFSF 1–L2	5.25	-	-
BFSF 1–L3	9.15	7.8	10.65
BFSF 1–L4	10.4	8.65	14.15
BFSF 1–L5	11.5	8.9	18.6
BFSF 1–L6	12.5	10.2	21.5
BFSF 1–L7	13.37	10.62	23.1

Figure 4.2 compares the primary recirculation zone (Lr_1) with experimental data of Armaly et al. (1983); Lee and Mateescu (1998) and Tihon et al. (2012) as well as numerical studies of Gualtieri (2005) and Erturk (2008).

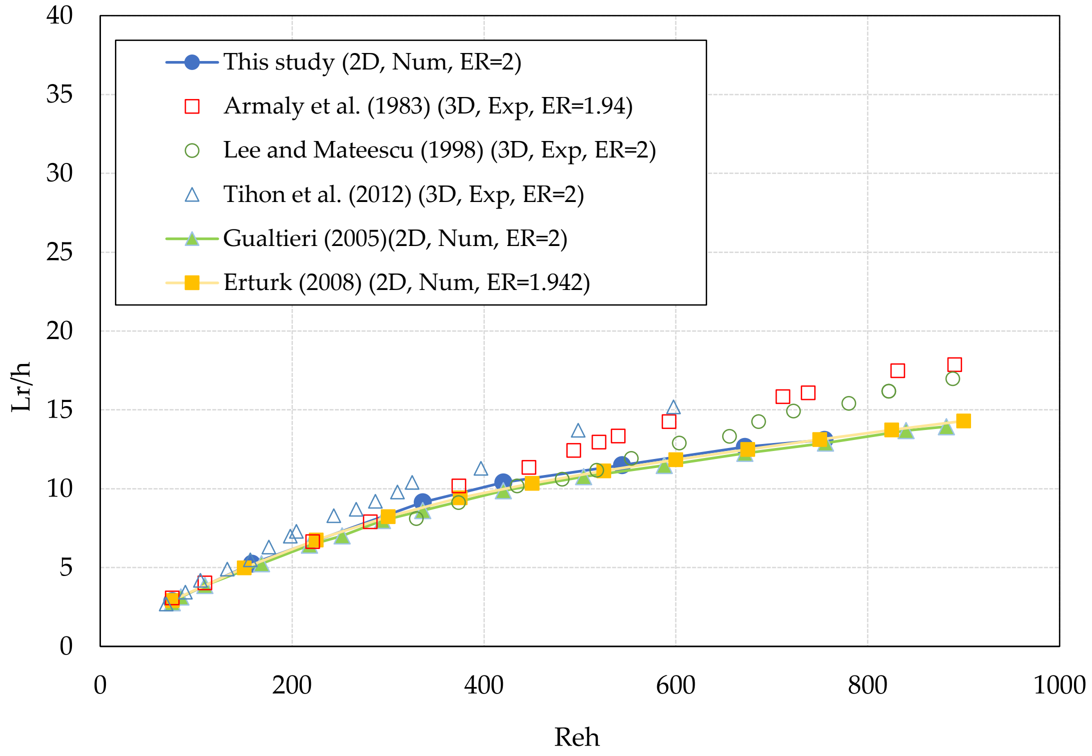

Figure 4.2. Dimensionless primary reattachment length L_{r1}/h vs. step-height Reynolds number Re_h in laminar flow (Exp: Experimental study; Num: Numerical study; 2D: two-dimensional; 3D: three-dimensional; ER: expansion ratio)

The present two-dimensional computational results diverge from the reported three-dimensional experimental and numerical data from the literature and tend to underestimate the increase of the primary reattachment length with increasing Re_h. Gualtieri (2005), reported that for $Re_h>300$, the onset of three-dimensional flow produces a disagreement between physical and computational results. Table 4.2 shows the average error in predicting reattachment length in comparison with literature data. The average error between the present numerical results and literature numerical and experimental data was lower than 18% and 5%, respectively. It is noted that the error was calculated for each Reynolds number, and finally their average was derived.

Table 4. 2. Average error (%) between numerical results of the reattachment lengths with literature data

References	Armaly et al. (1983)	Lee and Mateescu (1998)	Tihon et al. (2012)	Gualtieri (2005)	Erturk (2008)
Average error	< 18 %	<13%	<13%	<5%	<3%

4.2.2. Vertical profiles of the streamwise velocity

Figure 4.3 shows the distribution of the velocity for the two-dimensional BFSF at various Reynolds numbers in laminar flow. As expected in a backward-facing step flow, a recirculation zone formed behind the step in the expansion zone, where the fluid flowed from the upstream to the downstream. The flow followed the upper convex corner without revealing a flow separation.

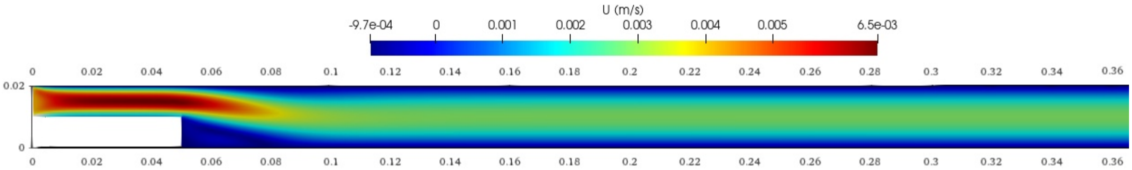

(a)

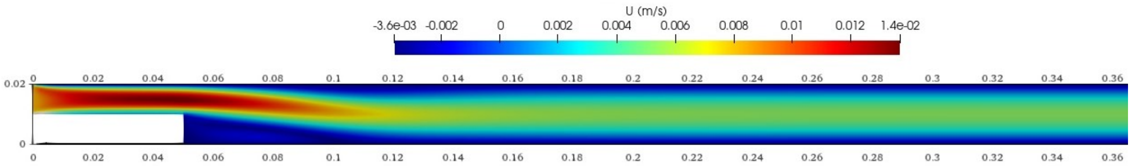

(b)

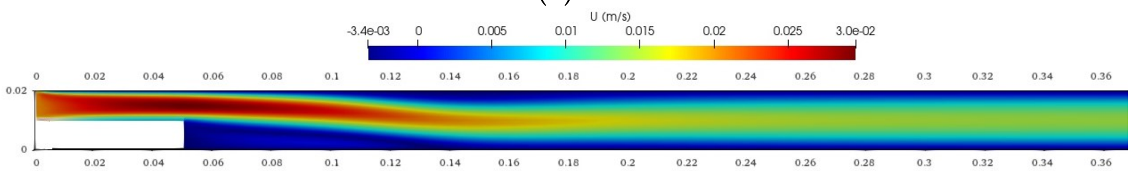

(c)

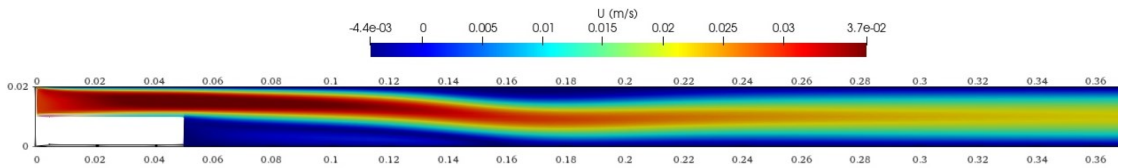

(d)

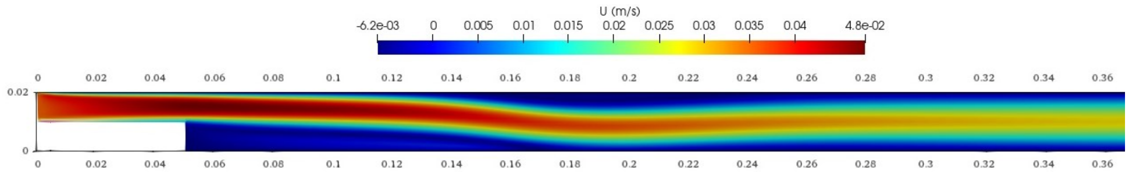

(e)

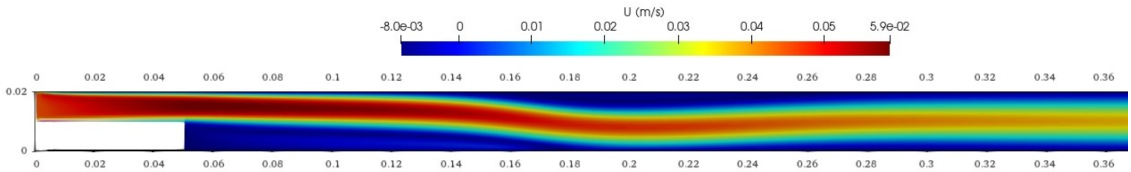

(f)

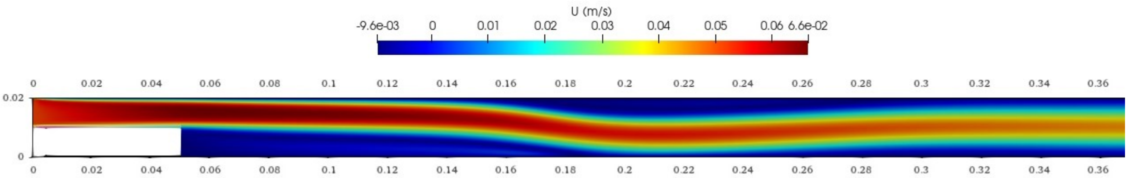

(g)

Figure 4.3. Velocity distribution in the backward-facing step at different Reynolds numbers of laminar flow (a) Re_h = 75 (b) Re_h = 158 (c) Re_h = 336 (d) Re_h = 420 (e) Re_h = 544 (f) Re_h = 672 (g) Re_h = 755

The dimensionless u-velocity distributions (u/U_{max}, where U_{max} is the maximum inlet velocity) profiles at different Reynolds numbers were compared quantitatively with available literature data. As examples, two vertical velocity profiles at Re_h =75 and 672 are presented in Figures 4.4 and 4.5.

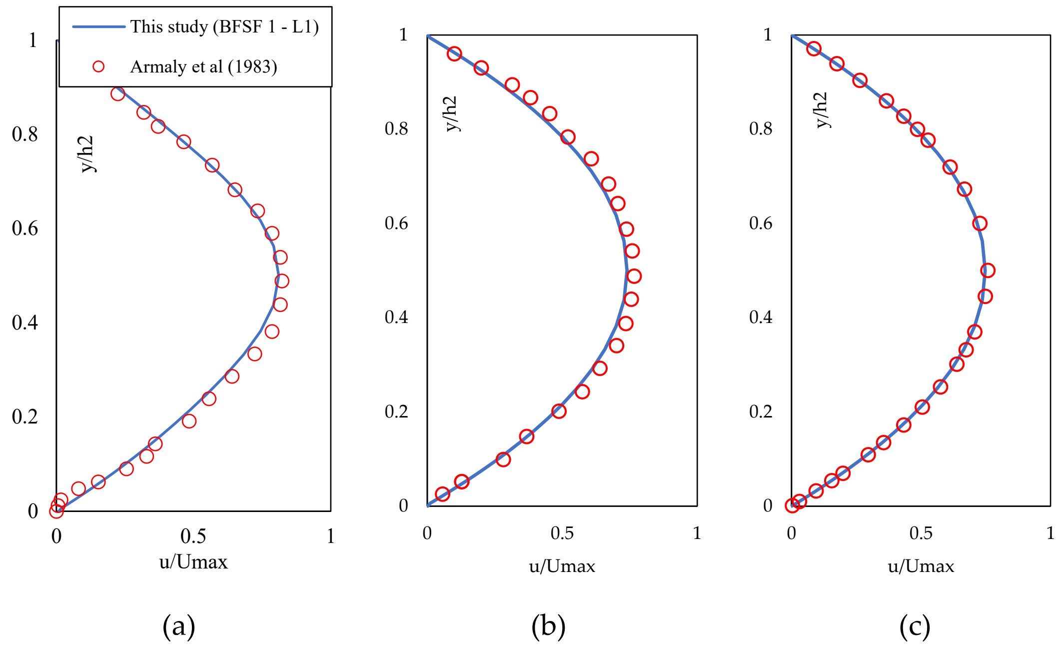

Figure 4.4. Dimensionless u-velocity profiles (u/U_{max}, where U_{max} is the maximum inlet velocity) at different streamwise locations in Re_h = 75 with experimental data of Armaly et al. (1983). (a) x/h = 4.8, (b) x/h = 12.04, (c) x/h = 30.31

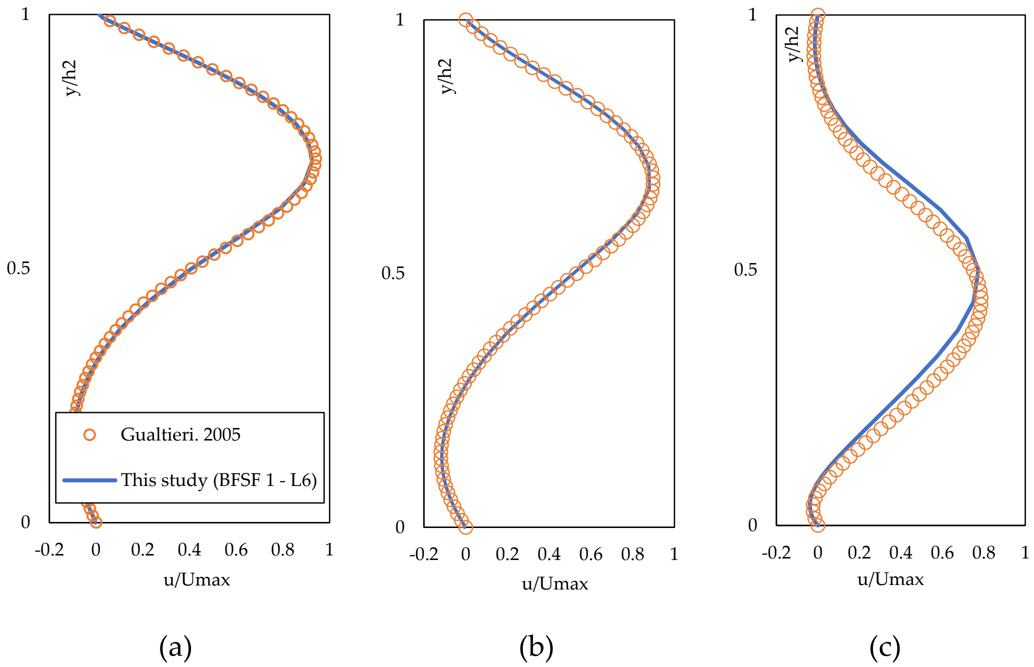

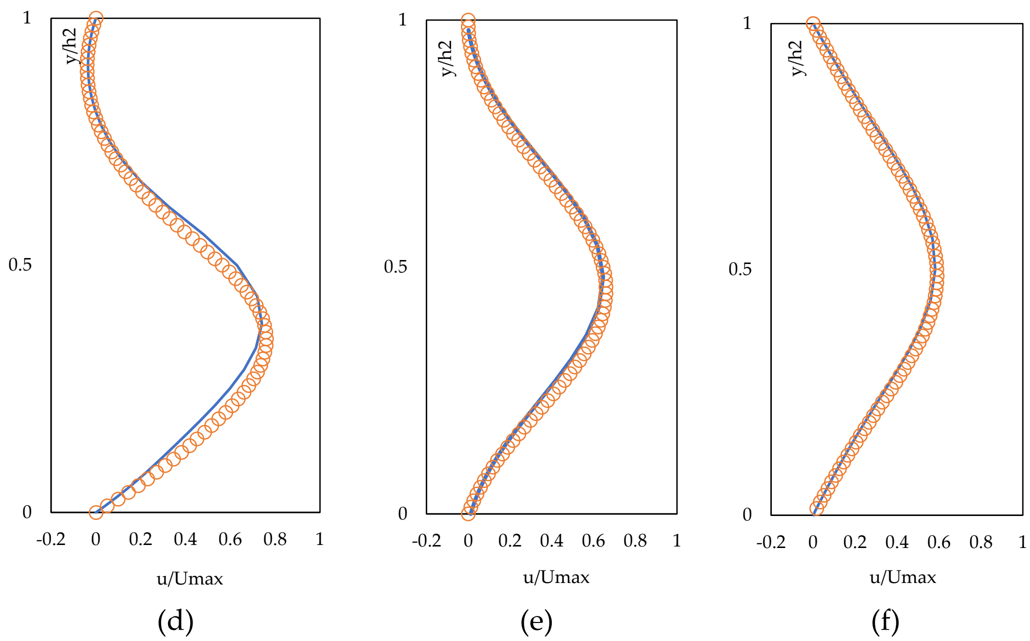

Figure 4.5. Dimensionless u-velocity profiles (u/U_{max}, where U_{max} is the maximum inlet velocity) at different streamwise locations in Re_h = 672 with numerical results of Gualtieri (2005). (a) x/h=5, (b) x/h=7.5, (c) x/h=12, (d) x/h=15, (e) x/h=22.5, (f) x/h=30

The locations were chosen at different locations including recirculation zones at the upper and bottom walls. The u-velocity profiles showed that the flow separated at the step, resulting in recirculation regions downstream of the step, and then redeveloped into a fully developed parabolic velocity profile in the larger channel. This coincides with data reported in the literature (Armaly et al. 1983). The u-velocity distributions were compared quantitatively at different locations of the domain downstream of the step with the experimental data of Armaly et al. (1983), and the numerical results of Gualtieri, (2005). The results were consistent with the literature data and the average error between numerical and literature data for ranges of Reynolds numbers were lower than 8.1%.

4.2.3. Skin friction distribution

The boundary layer is associated with important characteristics such as the skin friction coefficient. The skin friction coefficient, C_f, is a dimensionless quantity derived from the averaged wall shear stress (τ_w) as (Anderson 2011):

$$C_f = \frac{2\tau_w}{\rho u^2} \tag{4.1}$$

The distribution of the skin friction coefficient (C_f) at the bottom wall was calculated. The minimum value of the skin friction coefficient ($C_{f,\,min}$) compared with the experimental data and numerical results of Tihon et al. (2012) in Figure 4.6. For comparison, in Figure 4.6, due to difference expansion ratio and step-heightو the Reynolds numbers of present study were normalized by the Reynolds numbers of Tihon et al. (2012).

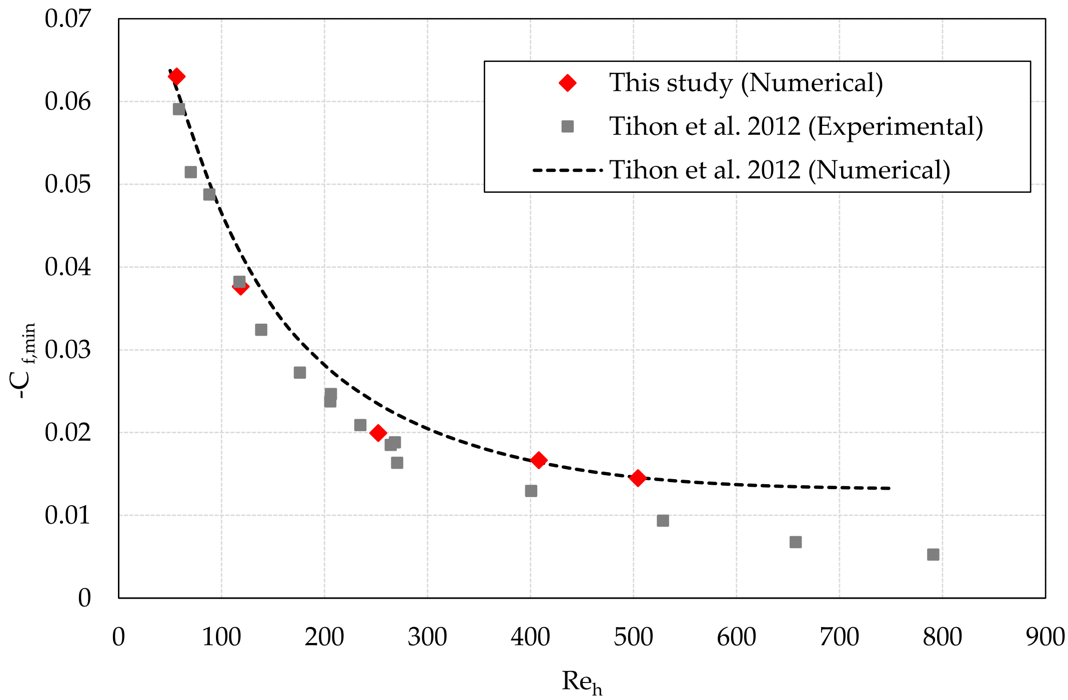

Figure 4.6. Dimensionless minimum value of the skin friction coefficient ($C_{f,\,min}$) vs. step-height Reynolds number Re_h in laminar flow

The minimum value of the skin friction coefficient ($C_{f,\ min}$) was observed inside the primary recirculation zone. The average error between the numerical results of this study and the literature experimental and numerical results) Tihon et al. 2012) were lower than 20% and 8.5 %, respectively.

4.3. Turbulent flow

4.3.1. Recirculation zone and reattachment length

As in laminar flow, the flow separated at the sharp corner of the step and reattached downstream at the bottom wall. The reattachment lengths of the BFSF in four turbulence models (standard k-ε, RNG k-ε, standard k-ω, and SST k-ω,) were evaluated (Table 4.3) and compared with literature experimental data (Armaly et al. 1983, Chandrsuda and Bradshaw 1981, Jovic and Driver 1994, Wang et al. 2019, Yao 2000) and numerical results (Barri et al. 2010, Dange 2010, Darmawan and Tanujaya 2019, Jongebloed 2008, Kopera et al. 2011, Krishnamoorthy 2007, Le et al. 1997, Ratha and Sarkar 2015, Togun et al. 2014, Wang et al. 2019). The data were plotted in Figure 4.7 as the normalized reattachment length by the step height against the Reynolds number (Re_h).

In the turbulent flow over the backward-facing step, the reattachment length is independent of the step-height Reynolds number and is mostly between 5 and 8 times the step height. This is consistent with the present study. The present numerical results were compared with experimental data and numerical results from Wang et al. (2019) at Reh=9,000 and ER=2. Table 4.3 lists the value of the reattachment lengths in the BFSF.

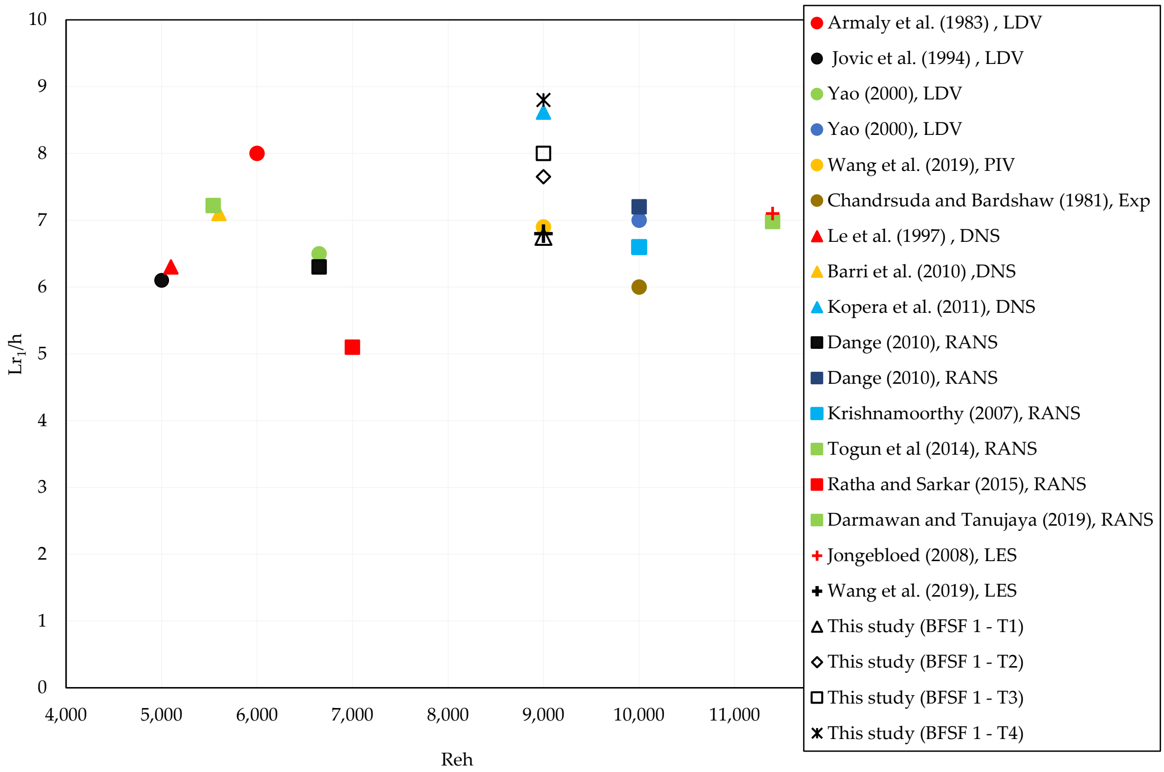

Figure 4.7. Dimensionless primary reattachment length (Lr_1/h) at different step-height Reynolds numbers Re_h with literature experimental and numerical results in the turbulent flow

Table 4. 3. Reattachment length in past numerical and experimental studies (Exp: Experimental study; Num: Numerical study; 2D: two-dimensional; 3D: three-dimensional)

Case	Re_h	ER	Lr_1/h	Remarks
This study (BFSF 1 – T1)	9,000	2	6.75	Num, 2D
This study (BFSF 1 – T2)	9,000	2	7.65	Num, 2D
This study (BFSF 1 – T3)	9,000	2	8	Num, 2D
This study (BFSF 1 – T4)	9,000	2	8.8	Num, 2D
Kopera et al. 2011	9,000	2	8.62	Num, 3D
Araujo and Rezende 2017	9,000	2	6.34	Num, 2D
Wang et al. 2019	9,000	2	6.9	Exp, 3D
Wang et al. 2019	9,000	2	6.7	Num, 2D

The average error between the standard k-ε model with the experimental and two-dimensional numerical results (Wang et al. 2019) was lower than 3% and 6 %, respectively. The most accurate model in predicting Lr_1 was the standard k-ε, followed by RNG k-ε, standard k-ω, and SST k-ω.

4.3.2. Vertical profiles of the streamwise velocity

The distribution of the velocity for the two-dimensional BFSF at various turbulence models of turbulent flow are shown in Figure 4.8.

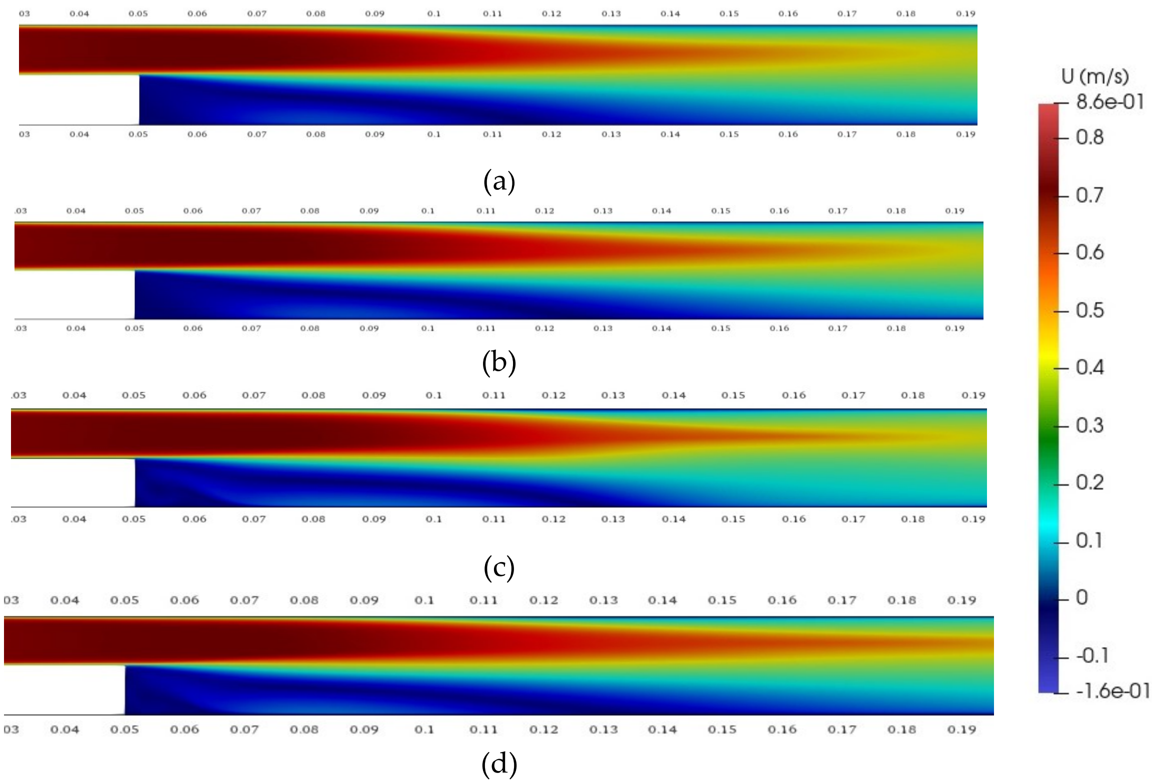

Figure 4.8. Velocity distribution in the backward-facing step at different turbulence models of turbulent flow. (a) Standard k-ε (b) RNG k-ε (c) Standard k-ω (d) SST k-ω

The distribution of the u-velocity of the 2D BFSF in different turbulence models was compared with previous studies (Kopera et al. 2011, Wang et al. 2019) at different locations (Figure 4.9).

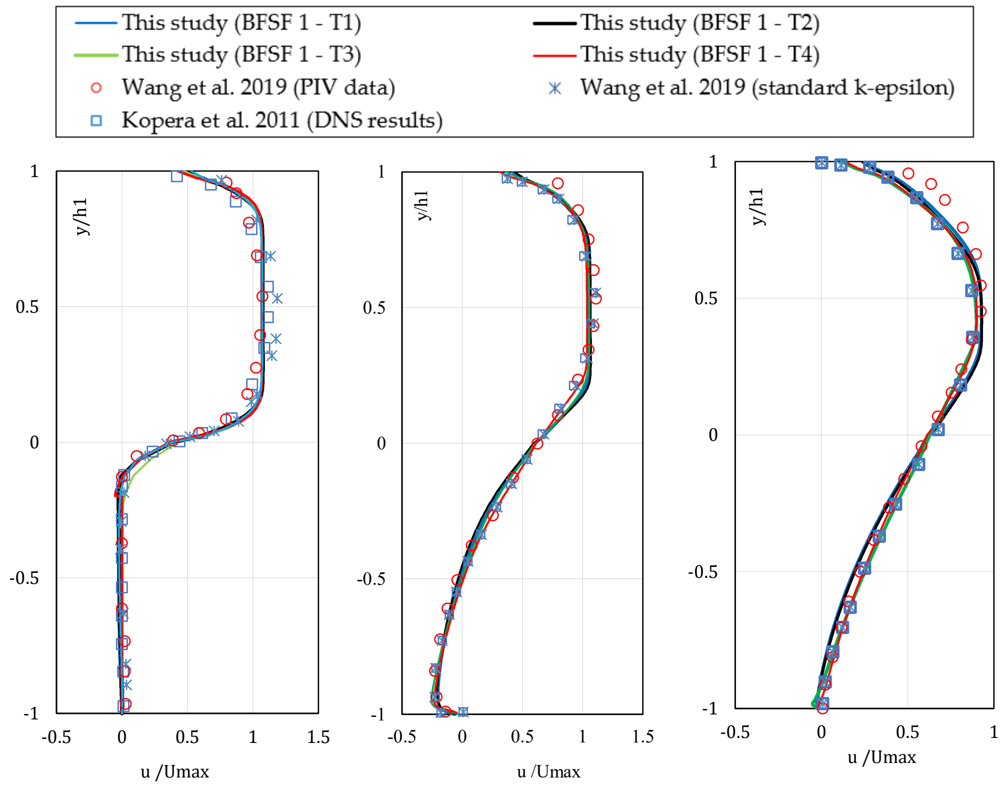

(a) (b) (c)

Figure 4.9. Dimensionless u-velocity (u/Umax, where U_{max} is the maximum inlet velocity) at different streamwise locations (a) x/Lr1=0.06 (b) x/Lr_1=0.46 (c) x/Lr_1=0.93

The first location (x/Lr_1 = 0.06) velocity was found near the step, consistent with the PIV data by Wang et al. (2019). The negative velocity in location x/Lr_1 = 0.46, represented the presence of reverse flow in the primary recirculation zone. In x/Lr_1 = 0.93, the standard k-ω, SST k-ω, and RNG k-ε models presented negative velocity because their Lr_1 was the largest among all models. The average error between the present numerical results and literature experimental data (Wang et al. 2019) is shown in Table 4.4.

Table 4. 4. Average error (%) at different locations in BFSF domain between present numerical results and experimental data of Wang et al. (2019)

Turbulence models	u-velocity profiles				Average error %
	x/Lr=0.06	x/Lr=0.46	x/Lr=0.93	x/Lr=2.32	
Standard k-ε	10.47	10.05	10.1	8.9	9.88
RNG k-ε	10.37	11.46	9.9	8.5	10.05
Standard k-ω	10.10	11.67	6.34	9.13	9.31
SST k-ω	10.23	11.97	4.67	8.45	8.83

The average error between numerical results and PIV data obtained by Wang et al. (2019) in all u-velocity profiles was ranging from 8.8 % to 10.05%. As shown in Table 4.5, the numerical results were compared with the DNS results of Kopera et al. (2011). The average error in predicting u-velocity profiles compared with the DNS results (Kopera et al. 2011) ranged from 7.8 % to 10.6%.

Table 4. 5. Average error (%) at different locations in BFSF domain between present numerical results and DNS results of Kopera et al. (2011)

Turbulence models	u-velocity profiles				Average error %
	x/Lr=0.06	x/Lr=0.46	x/Lr=0.93	x/Lr=2.32	
Standard k-ε	6.96	7.85	13.9	13.7	10.6
RNG k-ε	6.5	11.44	12.72	11.6	10.5
Standard k-ω	9.22	7.24	5.6	11.65	8.43
SST k-ω	7.4	7.14	5.3	11.46	7.82

The average error of velocity profiles for different turbulence models between the present numerical results and literature experimental data (Wang et al. 2019) numerical results (Kopera et al. 2011) is shown in Table 4.6.

Table 4. 6. Average error (%) between the present numerical results of the u-velocity profiles with experimental data (Wang et al. 2019) and numerical results (Kopera et al. 2011)

Turbulence models error		Standard k-ε	RNG k-ε	Standard k-ω	SST k-ω
References	Wang et al. 2019	< 9.88 %	<10.05%	<9.31%	<8.8%
	Kopera et al. 2011	< 10.6 %	<10.5%	<8.43%	<7.82%

With comparison results with experimental data (Wang et al. 2019), the error was from 8.8 % to 9.88%. The most accurate model in predicting velocity profiles was the SST k-ω, followed by the standard k-ω, standard k-ε and RNG k-ε. The SST k-ω model was already recommended for cases with adverse pressure gradient and flow separation because it combines the advantages of the standard k-ω and standard k-ε models (Araujo and Rezende 2017).

4.3.3. Skin friction distribution

The distribution of skin friction coefficient (C_f) at the bottom wall for different turbulence models was compared with literature data (Adams and Johnston 1988b, Jovic and Driver 1995, Kopera et al. 2011, Spazzini et al. 2001) in Figure 4.10.

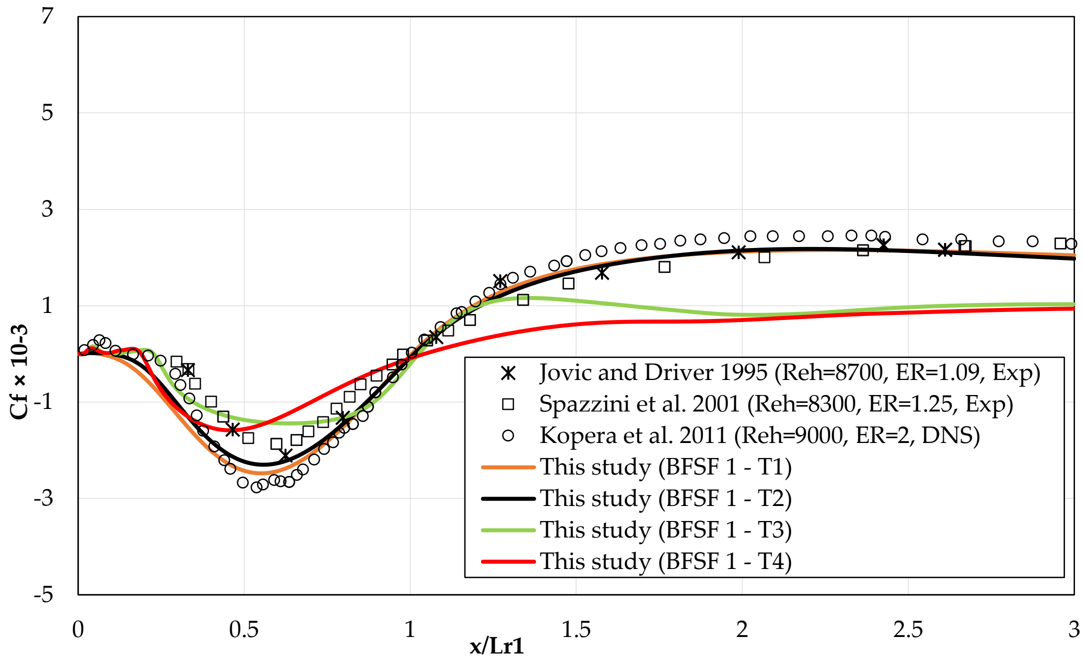

Figure 4.10. Longitudinal distribution of skin friction coefficient (C_f) at the bottom wall downstream of the step

The results were compared with the available numerical result Kopera et al. (2017) at Re_h=9,000 and ER=2. The distribution of skin friction in the standard k-ε and RNG k-ε turbulence models was consistent with that of the literature experimental data (Jovic and Driver 1995, Spazzini et al. 2001) and numerical results (Kopera et al. 2011). The average error was lower than 17.5%. The most accurate model in predicting skin friction coefficient was the standard k-ε, followed by RNG k-ε, standard k-ω, and SST k-ω. The standard k-ω, and SST k-ω were not good to capture the skin friction coefficient near the bottom wall. Based on Robertson et al. (2015), different boundary conditions (the direct-wall and wall-function boundary conditions) can be used for walls. The standard implementation of OpenFOAM provides only a wall-function implementation of the omega and epsilon boundary conditions. In this study, for the prescription of the epsilon and omega near walls, epsilonWallFunction and omegaWallFunction were used with the default form that was presented in OpenFOAM. The noted differences may be due to the various wall-function treatments.

As a laminar flow, the C_f decreased and reached the minimum value in the recirculation zone and gradually recovers to positive values downstream of the reattachment point corresponding to the fully developed flow. A minimum value of the skin friction coefficient was observed within the recirculating region. Tihon et al. (2001), found that the minimum value of skin friction inside of the recirculation zone was Reynolds number dependent as (Tihon et al. 2001):

$$C_{f,min} = -\,0.38\ Re_h^{-0.57} \qquad (4.2)$$

The minimum value of skin friction $C_{f,\,min}$ obtained from the standard k-ε model was compared with the experimental data (Jovic and Driver 1995, Tihon et al. 2001) and numerical results (Kim and Moin 2010, Smirnov et al. 2018) (Figure 4.11). The present numerical results fitted well with equation 4.2 and the literature data.

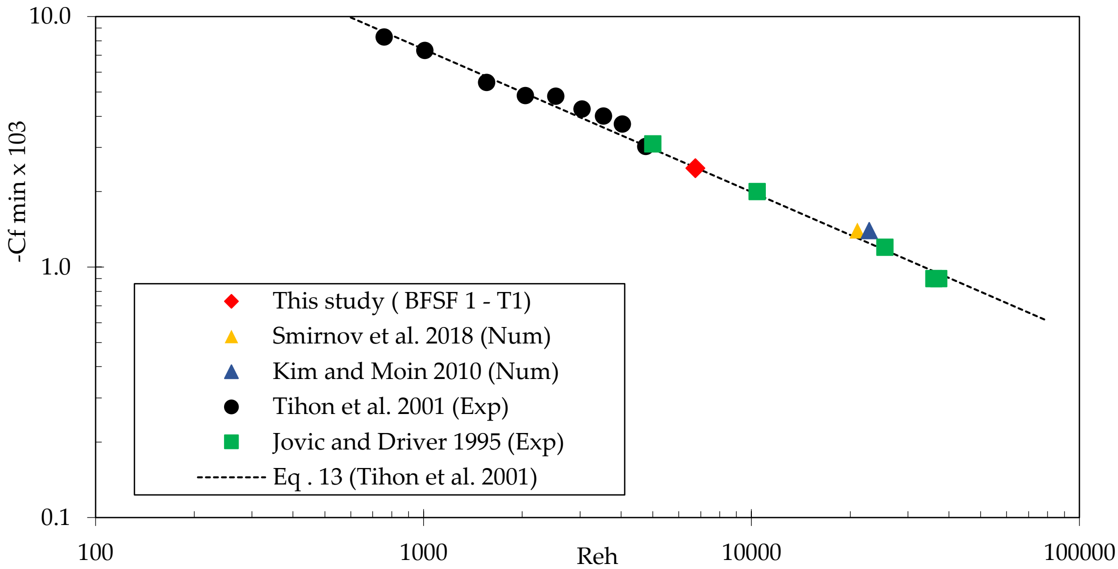

Figure 4.11. Dimensionless minimum value of the skin friction coefficient ($C_{f,\,min}$) vs. step-height Reynolds numbers Re_h

4.3.4. Static pressure coefficient

One of the most important characteristics of the bottom wall is the pressure coefficient. The wall static pressure coefficient is defined as (Clancy 1975):

$$C_p = \frac{P - P_0}{0.5 \rho u^2} \tag{4.3}$$

where P is the wall static pressure in any location and P_0 is the reference wall static pressure measured at x= - 4h, y = 1.5h (h is step height) upstream of the step as suggested by Kopera et al. (2011).

The static pressure increased starting from the corner of the bottom wall. The distribution of pressure farther downstream of the step remained relatively stable in the flow recovery process. According to Kim et al. (1980), to normalize the variations due to the different expansion ratios of BFSF, the normalized pressure coefficient (C^*_p) was defined as (Kim et al. 1980):

$$C^*_p = \frac{C_p - C_{p,\,min}}{C_{p,\,Bc} - C_{p,\,min}} \tag{4.4}$$

where $C_{p,\,min}$ is the minimum pressure coefficient and $C_{p,\,BC} = \frac{2}{ER}\left(1 - \frac{1}{ER}\right)$ is Borda-Carnot pressure coefficient (Kim et al. 1980). The normalized pressure coefficients (C^*_p) against the location scaled with the reattachment position, were compared in Figure 4.12.

The C^*_p values computed by the different turbulence models at the bottom wall agreed with literature experimental data (Driver and Seegmiller 1985, Kim et al. 1980, Westphal et al. 1984) and numerical results (Kopera et al. 2011).

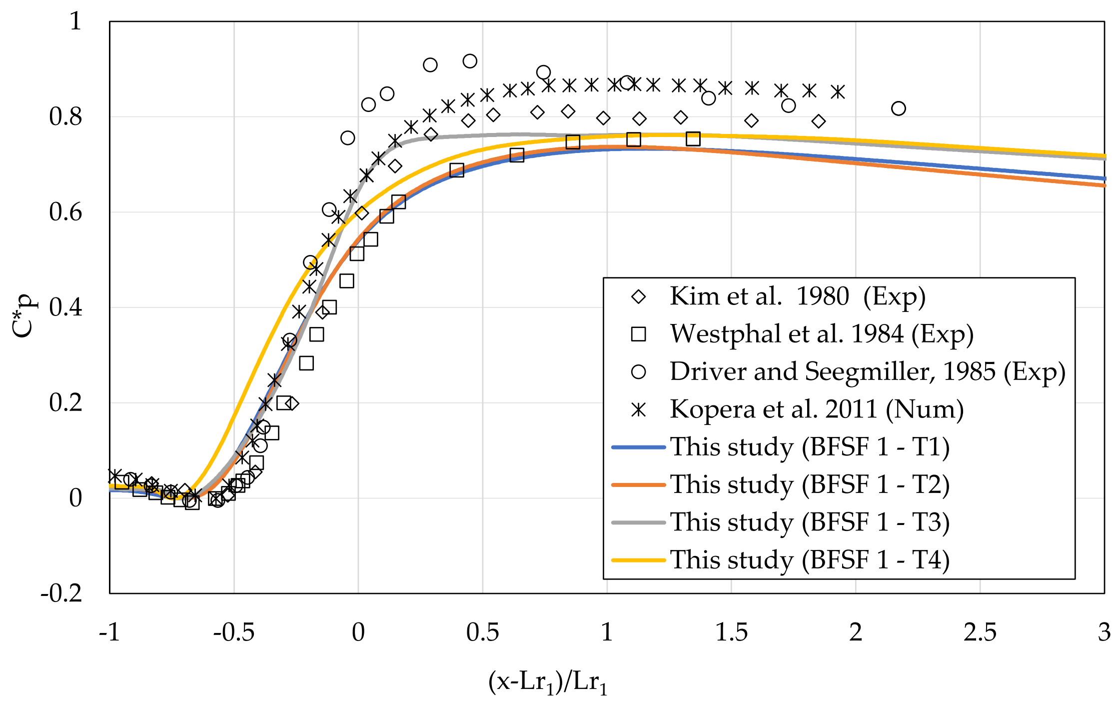

Figure 4.12. Longitudinal normalized pressure coefficient (C*p) at the bottom wall downstream of the step

A sharp increase of pressure was observed in the reattachment zone (from x=3h to x=7h), consistently with the literature results (Driver and Seegmiller 1985, Kim et al. 1980, Kopera et al. 2011, Westphal et al. 1984). The distribution of pressure farther downstream remained relatively stable in the flow recovery process. The most accurate model in predicting normalized pressure coefficients was the standard k- ε followed by standard k- ω, RNG k-ε, and SST k-ω with an average error lower than 20.5%.

4.4. Discussion

Flow over a backward-facing step could be found in many engineering applications where there is a recirculation zone or sudden change in pressure. In this chapter, laminar and turbulent flow over a backward-facing step (BFSF) were studied. To validate the results herein, several study cases were conducted, and the numerical results were compared with literature numerical and experimental data. The following conclusions can be drawn:

- Laminar backward-facing step flow was investigated for a wide range of Reynolds numbers $75 \leq Re_h \leq 755$ and the simulated reattachment lengths, velocity profiles, and skin frictions were compared with the available literature data. The average error between the present numerical results and literature numerical and experimental data for reattachment lengths and velocity profiles was lower than 8.1% and 18%, respectively. In addition, the average error in predicting the skin friction coefficient was lower than 20%.
- In turbulent flow, the simulated reattachment lengths, velocity profiles, skin friction coefficients, and pressure coefficient from several RANS models, standard k-ε, RNG k-ε, standard k-ω, SST k-ω, were compared with the available literature data. The most accurate model for predicting reattachment lengths, skin friction coefficient, and pressure coefficients was the standard k-ε model with an average error lower than 6, 17.5, and 20.5%, respectively.

Chapter 5 Analysis of results – Part1: Flow and turbulent characteristics

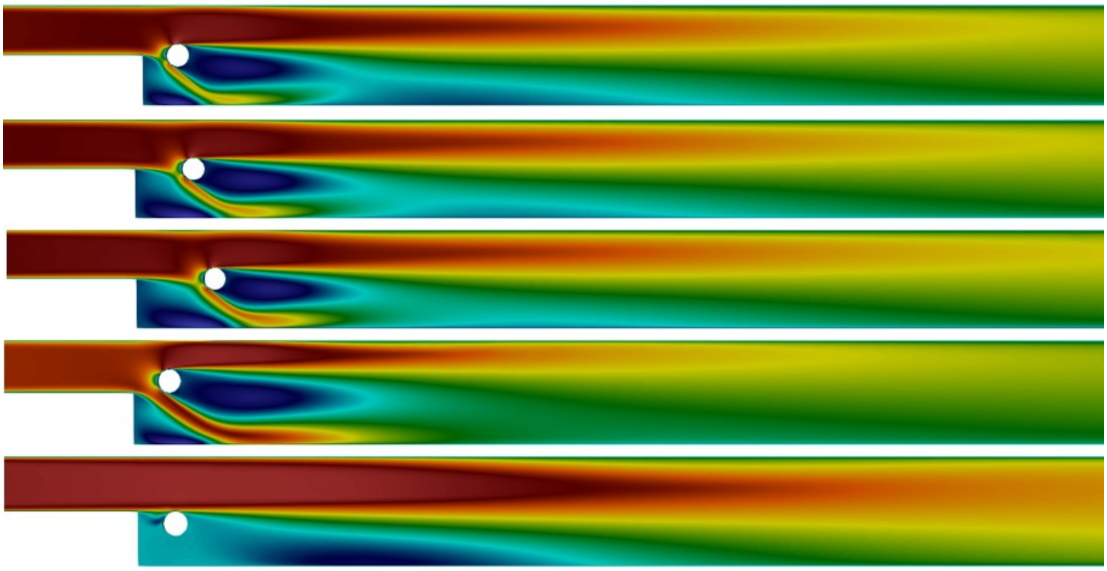

In this chapter, the effect of a cylinder on the flow and turbulent characteristics over the step are presented.

5.1. Introduction

Flow downstream of the step is complex and the presence of a cylinder creates ed-dies, transverse flows, velocity gradients, and other spatial flow patterns. A better understanding of how the cylinder interacts the flow downstream of the step leads to the quantification of its features. In the present study, two geometries were comparatively considered, namely the classical BFSF (BFSF 1) and a BFSF with a cylinder placed downstream of the step (BFSF 2), in both laminar and turbulent flow to investigate how the cylinder modifies the classical BFS flow structure.

5.2. Laminar flow

5.2.1. Recirculation zone and reattachment length

The most important characteristics of flow over the step are flow separation and reattachment (Gualtieri 2005). The adverse pressure gradient is due to the sudden expansion at the edge of the step, induced flow separation (Armaly et al. 1983). A sketch of the BFSF 2 in laminar flow is shown in Figure 5.1.

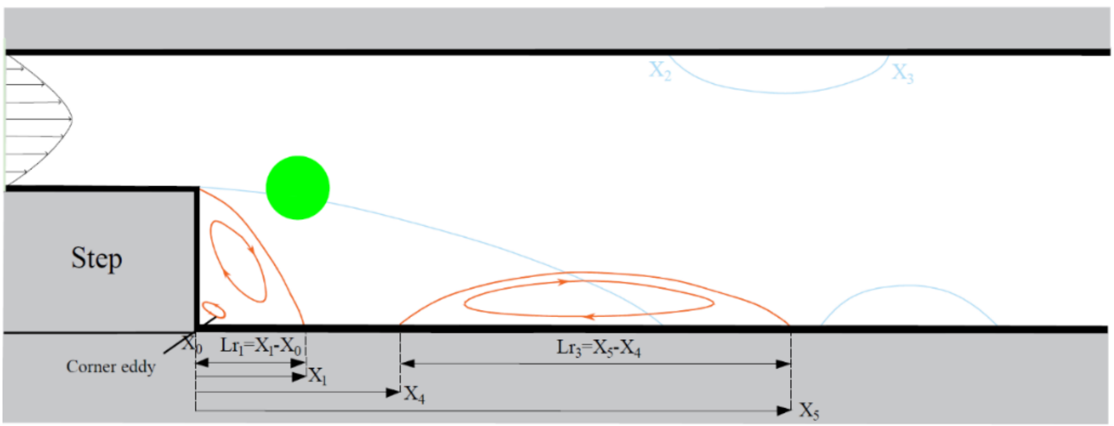

Figure 5.1. Sketch of the flow in the BFSF 2 in laminar flow (Blue lines show the recirculation zones for BFSF 1). Lr_1 and Lr_3 represent the length of primary and third recirculation zone at bottom wall.

For the BFSF 2, the flow separated at the step, but the dividing streamline was deviated by the cylinder to the bottom wall and the reattachment point X_1 was found to be upstream than for the BFSF 1 (Figure 5.1). In addition, the second recirculation zone on the upper wall was missing, while the third recirculation zone was observed even at $75 < Re_h \leq 755$ (Table 5.1), and it was upstream than in the BFSF 1. For the BFSF 2, Lr_1 and Lr_3 increased as Re_h increased. It is important to point out that for the BFSF 2, none of the recirculation zones was observed at Re_h=75. Table 5.1 lists the value of the normalized location of starting and ending recirculation zones in the BFSF 1 and BFSF 2. For the BFSF 2, while X_4 was unchanged, X_5 as the X_5/h increased as Re_h increased. The cylinder pushed the primary recirculation region upstream to the corner of the step and, hence, at each Re_h, Lr_1 was generally lower than that of the BFSF 1.

Table 5. 1. Reattachment and separation points of the recirculation zones at different step-height Reynolds number Re_h in laminar flow. (X_1 is a point that primary recirculation reattached to the bottom wall, X_2 is starting point of the second recirculation zone at upper wall and X_2 is ending point of second recirculation zone at upper wall. X4 and X5 are starting and ending points of third recirculation zone at bottom wall)

	X_1/h		**X_2/h**		**X_3/h**		**X_4/h**		**X_5/h**	
Re_h	BFSF1	BFSF2	BFSF1	BFSF2	BFSF1	BFSF2	BFSF1	BFSF2	BFSF1	BFSF2
75	2.88	-	-	-	-	-	-	-	-	-
158	5.25	0.45	-	-	-	-	-	4.4	-	5.26
336	9.15	0.7	7.8	-	10.65	-	-	2.3	-	12.15
420	10.4	0.8	8.65	-	14.15	-	-	2.25	-	15.1
544	11.81	0.85	8.9	-	18.6	-	-	2.1	-	19.5
672	12.65	0.9	10.2	-	21.5	-	-	2.1	-	23.65
755	13.37	0.9	10.62	-	23.1	-	-	2.05	-	26.3

Figure 5.2 compares the normalized location of X_5 point between the BFSF 2 of the numerical results of present study and the numerical results of the BFSF 1 from Erturk (2008) in various Reynolds numbers.

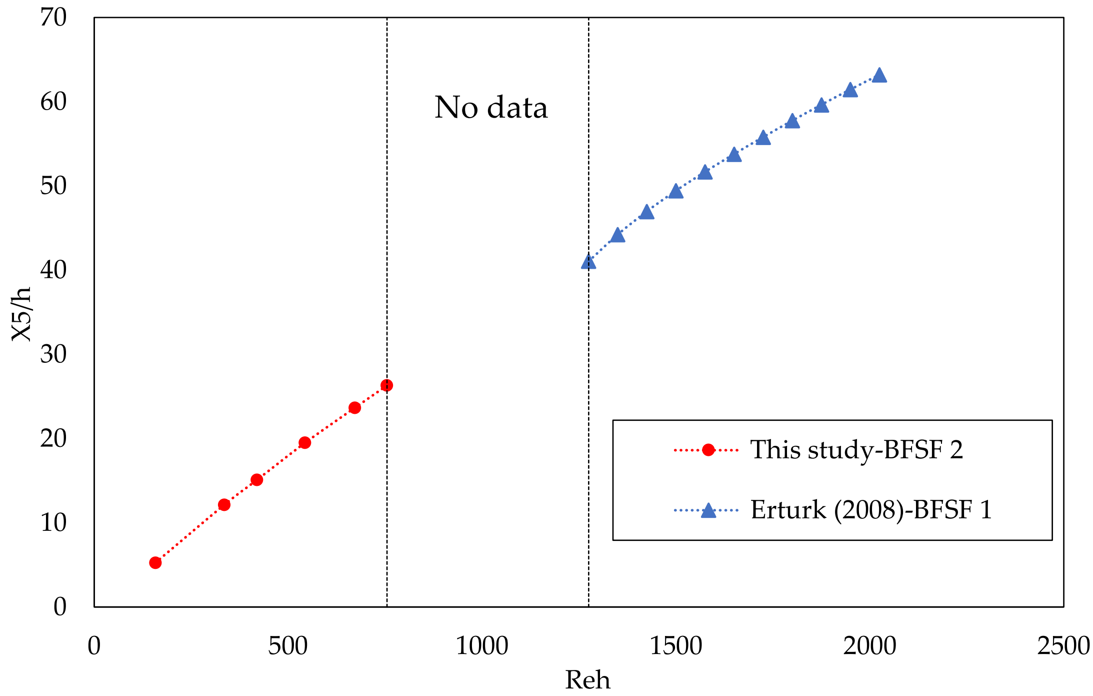

Figure 5.2. Dimensionless reattachment point of the third recirculation region (X_5/h) at different step-height Reynolds numbers Re_h of this study and numerical results of Erturk (2008)

As pointed out, the ending points of the third recirculation zone is denoted by X5. According to Figure 5.2, the laminar flow in the present study revealed the presence of the third recirculation zone in BFSF 2. In contrast, Erturk's (2008) numerical simulation observed this region in the flow of BFSF 1 at Reh = 1275, which continued to expand as the Reynolds number increased.

5.2.2. Cylinder wake

The flow past a cylinder creates a large drag due to the periodic separation and causes some differences in the pressure between downstream and upstream. Attention was particularly focused on the effect of the cylinder on the flow structure over the backward-facing step. In laminar flow, the structure of the flow past a single cylinder depends on the cylinder-diameter Reynolds number (Re_D) (Lienhard 1966). Figure 5.3 shows two-dimensional flow patterns past a cylinder at Reynolds numbers based on cylinder diameter.

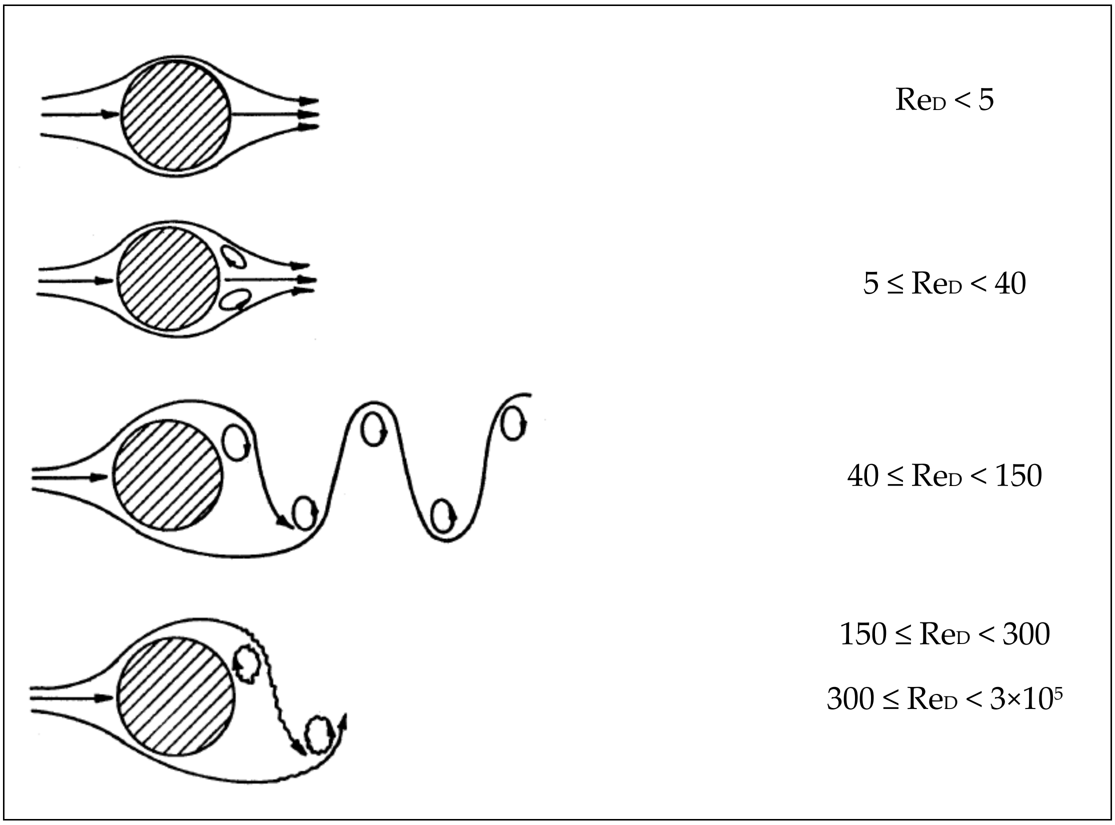

Figure 5.3. Various flow patterns over a 2D cylinder with increasing Reynolds number based on cylinder diameter. (Lienhard 1966)

At a low Reynolds number ($Re_D < 5$), the flow remains attached to the cylinder, no separation occurs, and viscous forces are dominant, thereby no wake is formed. For the range $5 \leq Re_D < 40$, a change takes place in the flow patterns and the flow separates from both sides of the cylinder. Two symmetric and stable vortices at both sides are formed and remain attached to the body. As the Reynolds number increased about $40 \leq Re_D < 150$, the flow pattern is developed. The wake becomes unstable, and one of the two vortices is break away and then the second is shed alternately from the cylindrical body. This phenomenon, known as Karman Vortex Street, happens because of the flow oscillation and the nonsymmetrical pressure in the wake zone. As Reynolds number is increased in the range $150 \leq Re_D < 300$, periodic irregular disturbances start in the wake with a gradual transition to turbulent in the vortex wake. Figure 5.4 depicts a variety of flow patterns downstream of a cylinder in the backward-facing step as the Reynolds number of the fluid increased.

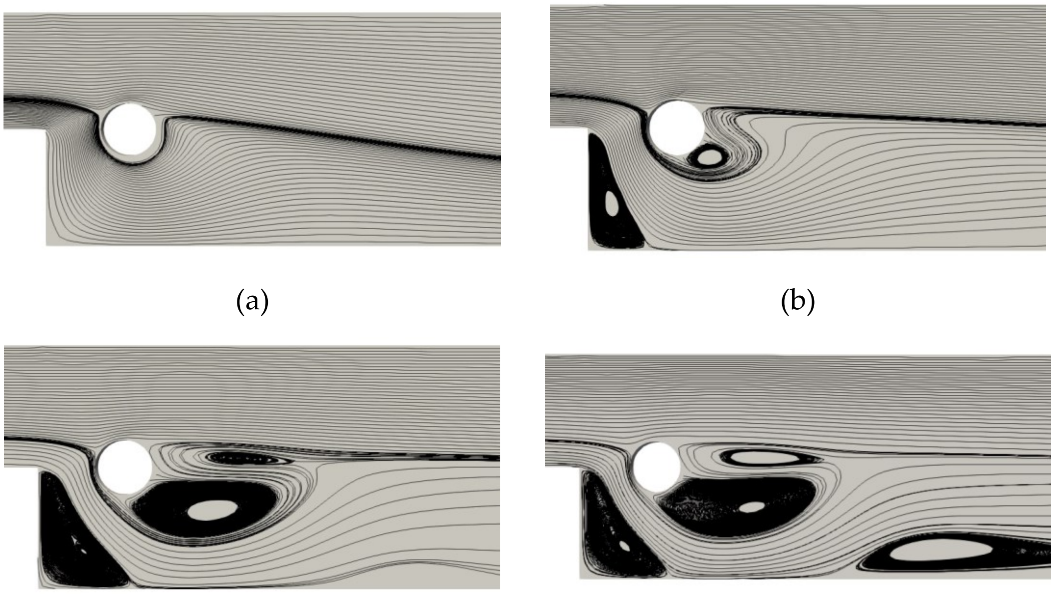

(a) (b) (c) (d)

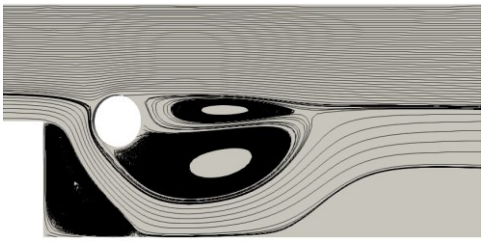

(e)

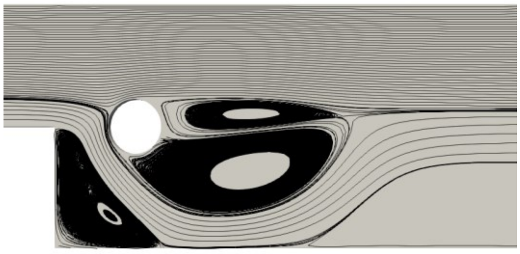

(f)

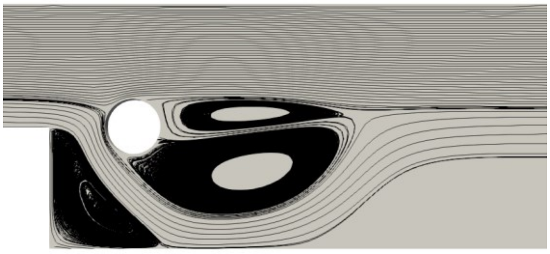

(g)

Figure 5.4. Streamlines of the flow behind a cylinder in the BFSF 2 at different cylinder diameter Reynolds number (Re_D). (a) BFSF 2 – L1 (b) BFSF 2 – L2 (c) BFSF 2 – L3 (d) BFSF 2 – L4 (e) BFSF 2 – L5 (f) BFSF 2 – L6 (g) BFSF 2 – L7

At low Reynolds number Re_D=15(BFSF 2 – L1), the flow was not noticeably affected by the presence of the cylinder and vortices did not form behind the cylinder. In the BFSF 2 – L2 (Re_D =28), the streamlines showed one vortex. However, for the range of Reynolds number $5 \leq Re_D < 40$, two symmetric and stable vortices behind a single cylinder were found. For the Reynolds number range $Re_D > 40$ (BFSF 2 – L3, BFSF 2 – L4, BFSF 2 – L5, BFSF 2 – L6, and BFSF 2 – L7), two asymmetric vortices found behind the cylinder in different sizes, and a large portion of these vortices shifted toward the below cylinder. However, for flow past a single cylinder in the Reynolds number range ($40 \leq Re_D < 150$), periodic irregular disturbances in the wake of a cylinder were observed. As a cylinder was placed downstream of the step, the step affected the near wake of the cylinder by changing the dynamics of the vortex generation.

5.2.3. Vertical profiles of the streamwise velocity

The distribution of the velocity for the two-dimensional BFSF at various turbulence models of turbulent flow is shown in Figure 5.5.

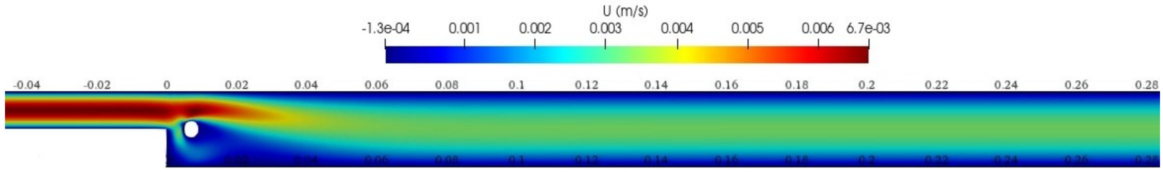

(a)

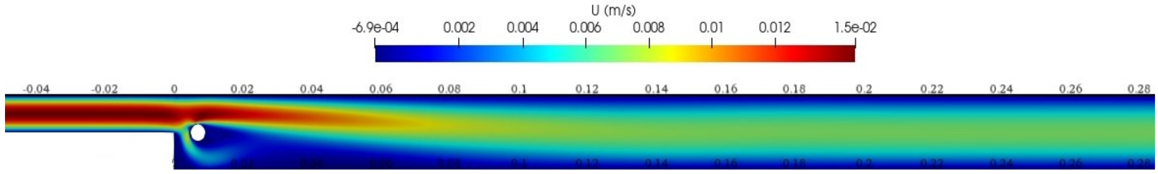

(b)

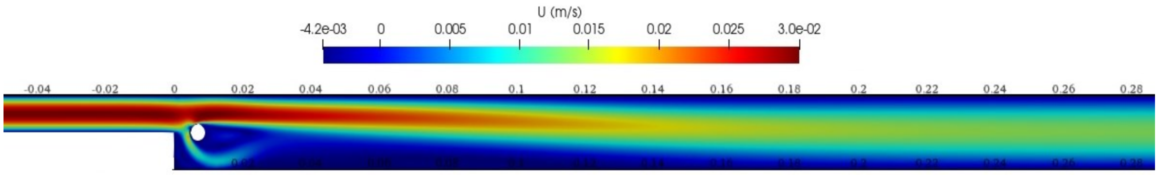

(c)

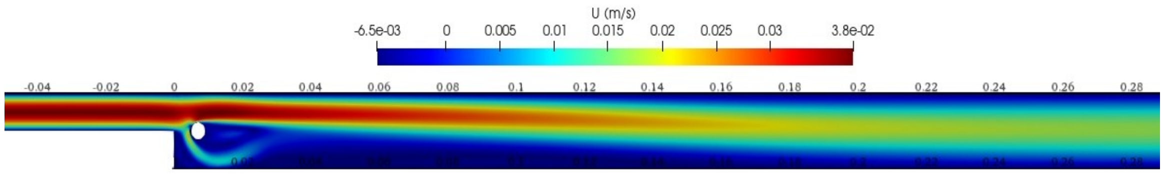

(d)

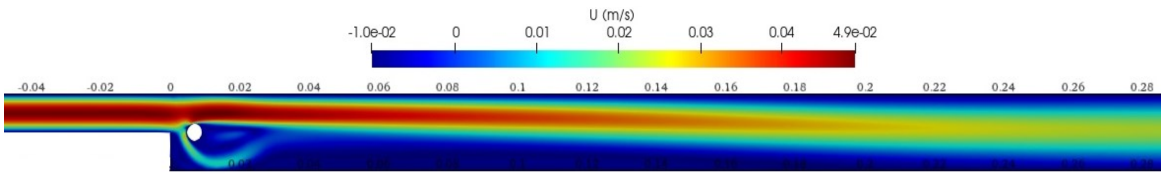

(e)

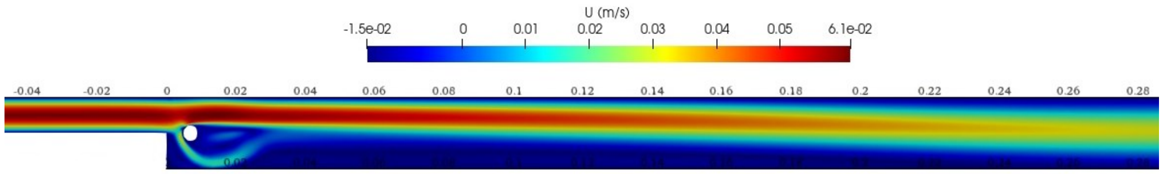

(f)

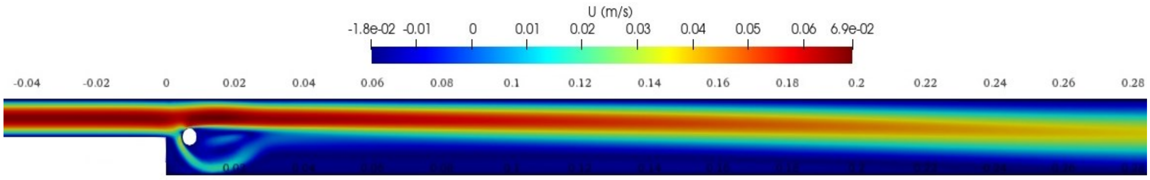

(g)

Figure 5.5. Velocity distribution in the BFSF 2 for different Reynolds numbers in laminar flow. (a) BFSF 2 – L1 (b) BFSF 2 – L2 (c) BFSF 2 – L3 (d) BFSF 2 – L4 (e) BFSF 2 – L5 (f) BFSF 2 – L6 (g) BFSF 2 – L7

The dimensionless u-velocity (u/U_{max}, where U_{max} is the maximum inlet velocity) profiles of the BFSF 1 and BFSF 2 Runs, are shown in Figure 5.6.

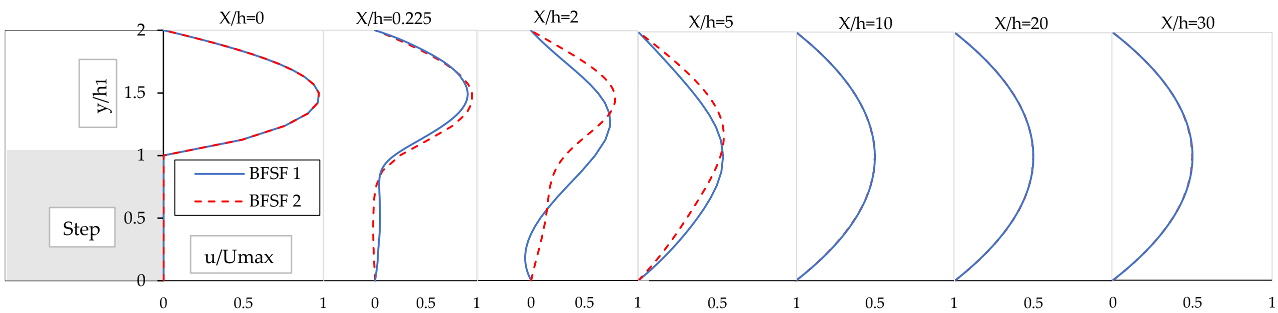

(a)

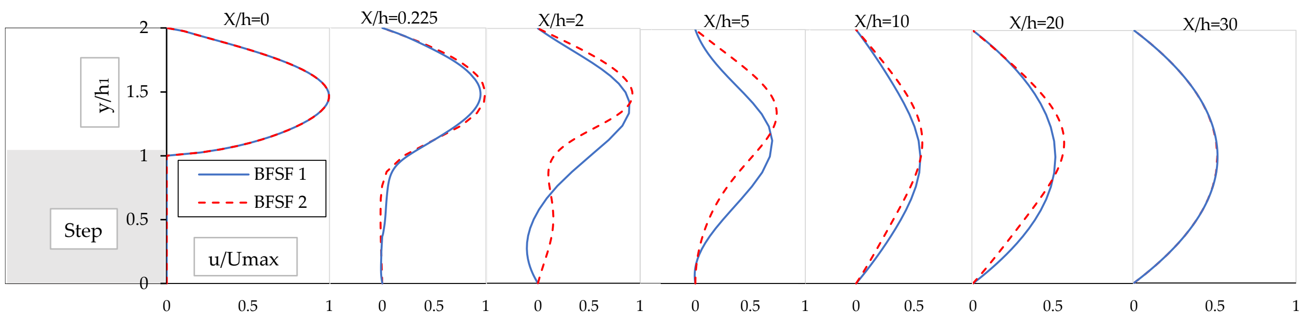

(b)

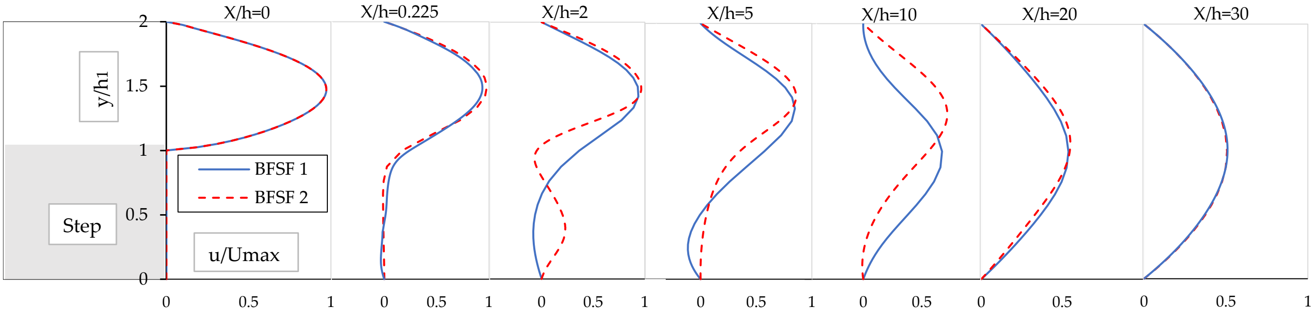
X/h=0
X/h=0.225
X/h=2
X/h=5
X/h=10
X/h=20
X/h=30
y/h1
Step
BFSF 1
BFSF 2
u/Umax

(c)

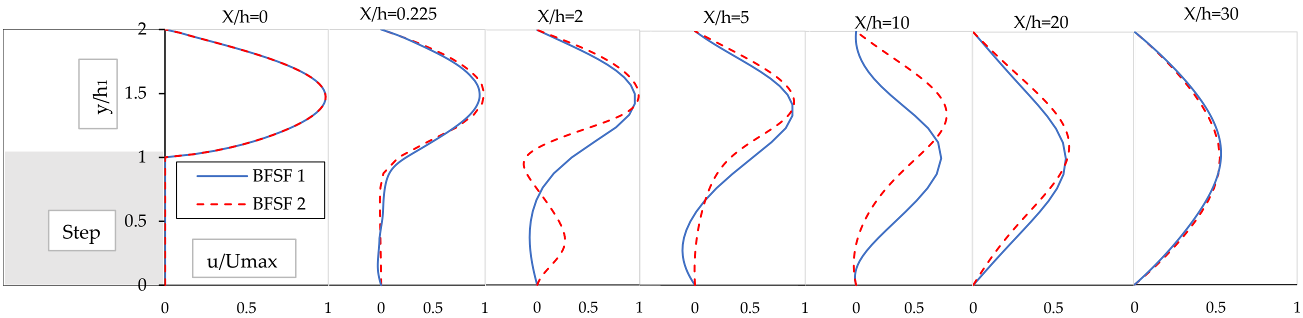
X/h=0
X/h=0.225
X/h=2
X/h=5
X/h=10
X/h=20
X/h=30
y/h1
Step
BFSF 1
BFSF 2
u/Umax

(d)

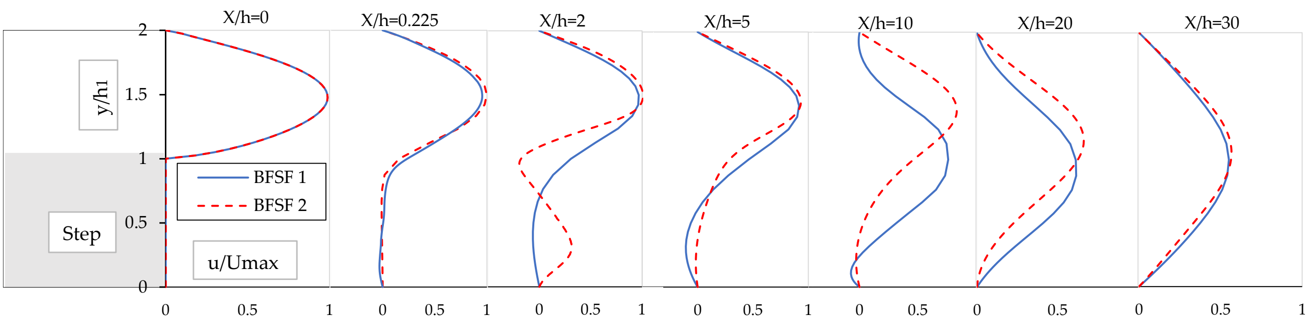
X/h=0
X/h=0.225
X/h=2
X/h=5
X/h=10
X/h=20
X/h=30
y/h1
Step
BFSF 1
BFSF 2
u/Umax

(e)

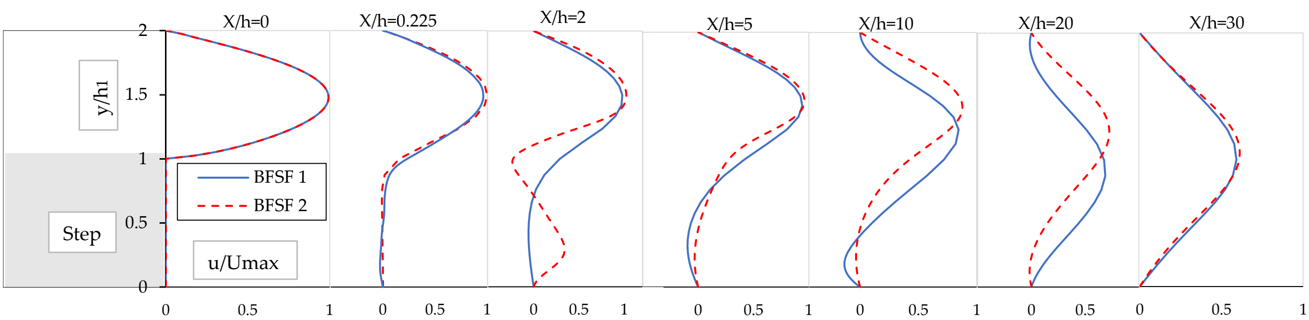
X/h=0
X/h=0.225
X/h=2
X/h=5
X/h=10
X/h=20
X/h=30
y/h1
Step
BFSF 1
BFSF 2
u/Umax

(f)

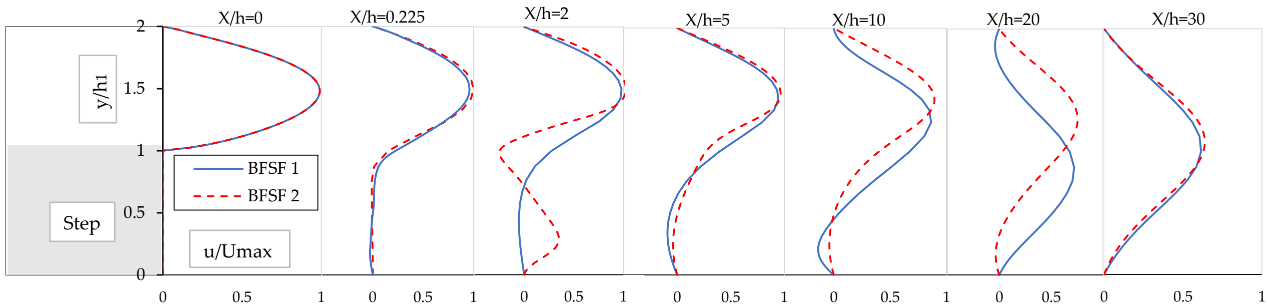

(g)

Figure 5.6. Dimensionless u-velocity profiles (u/U_{max}, where U_{max} is the maximum inlet velocity) at different Reynolds numbers for BFSF 1 and BFSF 2 Runs (a) BFSF 1 – L1 Vs. BFSF 2 – L1 (b) BFSF 1 – L2 Vs. BFSF 2 – L2 (c) BFSF 1 – L3 Vs. BFSF 2 – L3 (d) BFSF 1 – L4 Vs. BFSF 2 – L4 (e) BFSF 1 – L5 Vs. BFSF 2 – L5 (f) BFSF 1 – L6 Vs. BFSF 2 – L6 (g) BFSF 1 – L7 Vs. BFSF 2 – L7

In the BFSF 2, with the incident flow toward the cylinder, the regular patterns of the vortex shed rear of the cylinder. The maximum velocity for the BFSF 2 Runs was a bit higher than that of the BFSF 1 and the location of the maximum velocities shifted toward the upper wall. But, more importantly, the cylinder increased the skewness of the velocity profiles. The skewness of velocity profiles was calculated for both the BFSF 1 and the BFSF 2 in the following locations: x/h = 2 where the primary recirculation occurred; x/h = 5, x/h = 10 was downstream of the cylinder and at x/h = 30 where the flow developed and reached the outlet of the geometry. For the BFSF 2, the percentage of increasing skewness were 15, 185, 110, and 10 % at x/h = 2, x/h = 5, x/h = 10, and x/h = 30, respectively. The results indicated that the skewness of the velocity profile was near the cylinder larger than in other locations.

5.2.4. Skin friction distribution

The distribution of the skin friction coefficient (C_f) at the bottom wall was calculated. As shown in Figure 5.7, the skin friction coefficients of the BFSF 1 and BFSF 2 for different step-height Reynolds numbers were compared. In Figure 5.7, the vertical dotted line shows the position of the cylinder center.

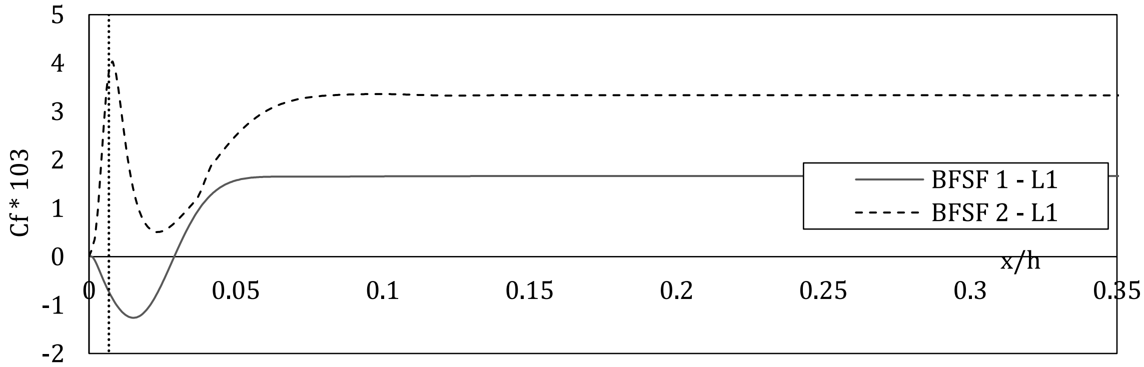

(a)

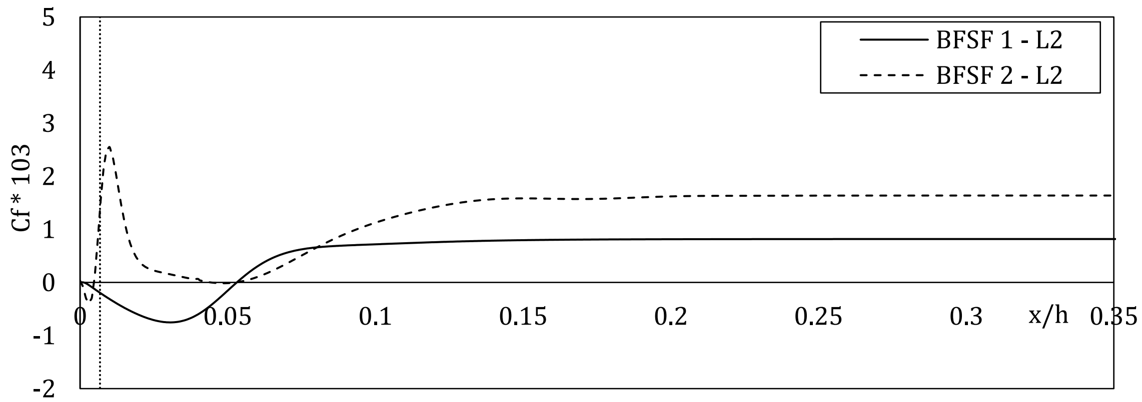

(b)

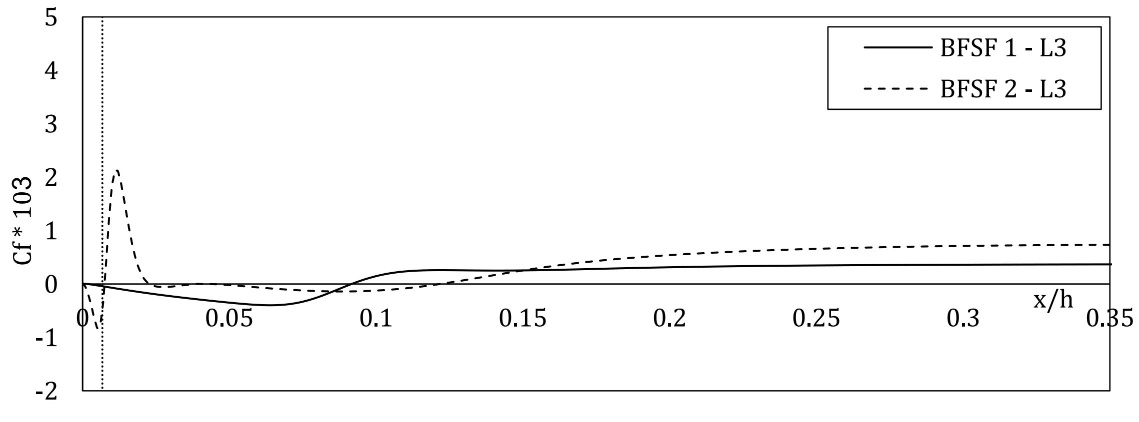

(c)

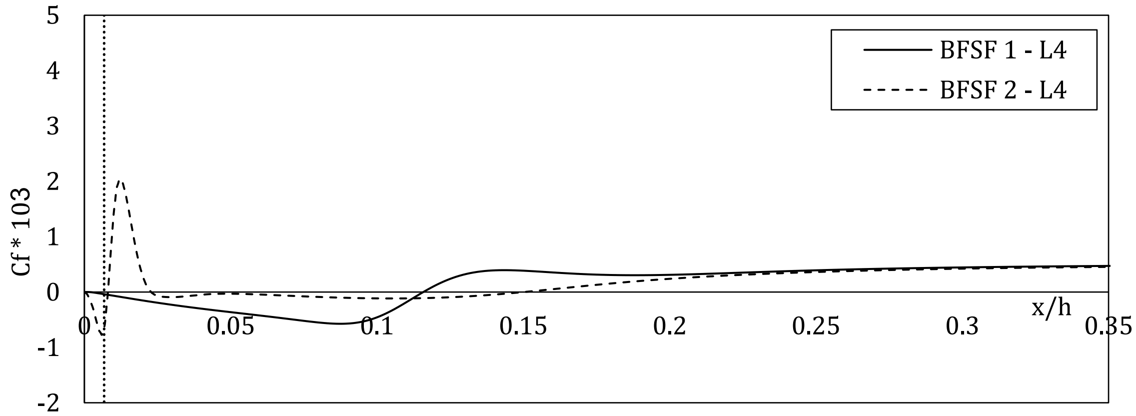
BFSF 1 - L4
BFSF 2 - L4
Cf* 103
x/h
5
4
3
2
1
0
-1
-2
0
0.05
0.1
0.15
0.2
0.25
0.3
0.35

(d)

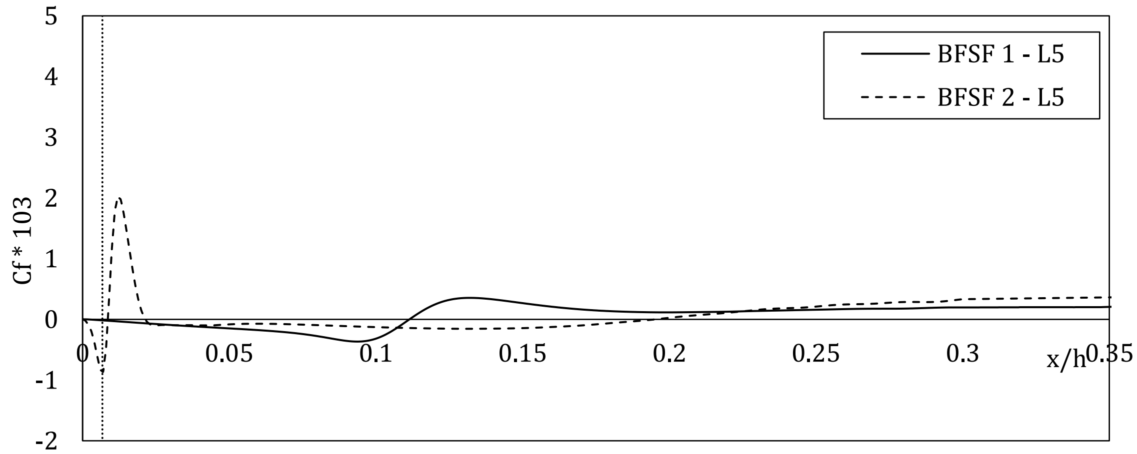
BFSF 1 - L5
BFSF 2 - L5
Cf* 103
x/h
5
4
3
2
1
0
-1
-2
0
0.05
0.1
0.15
0.2
0.25
0.3
0.35

(e)

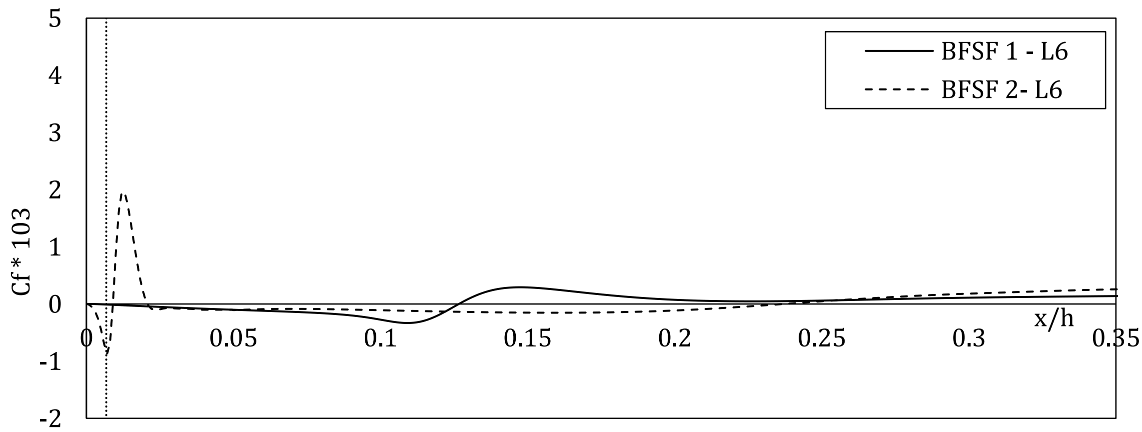
BFSF 1 - L6
BFSF 2- L6
Cf* 103
x/h
5
4
3
2
1
0
-1
-2
0
0.05
0.1
0.15
0.2
0.25
0.3
0.35

(f)

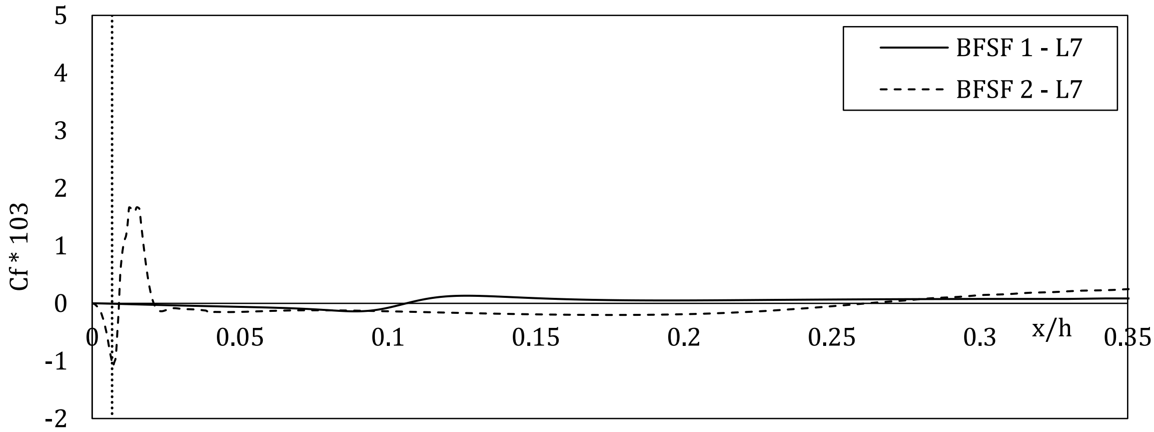

(g)

Figure 5.7. Longitudinal distribution of skin friction coefficient (C_f) at the bottom wall downstream of the step in the BFSF 1 and BFSF 2 at different Re_h (a) BFSF 1 – L1 Vs. BFSF 2 – L1 (b) BFSF 1 – L2 Vs. BFSF 2 – L2 (c) BFSF 1 – L3 Vs. BFSF 2 – L3 (d) BFSF 1 – L4 Vs. BFSF 2 – L4 (e) BFSF 1 – L5 Vs. BFSF 2 – L5 (f) BFSF 1 – L6 Vs. BFSF 2 – L6 (g) BFSF 1 – L7 Vs. BFSF 2 – L7.

In the BFSF 1 Runs, the C_f decreased and reached the minimum values in the recirculation zone and gradually recovers to positive values downstream of the reattachment point. The constant value skin friction coefficient downstream showed a fully developed channel flow. In the BFSF 2, two minimum values of $C_{f,\,min}$ were observed. As previously pointed out, two recirculation zones (Lr_1 and Lr_3) were observed at the bottom wall of the BFSF 2 in laminar flow. The minimum value of the skin friction coefficient ($C_{f,\,min}$) occurred due to the recirculating flow where the velocity distribution changed. For the BFSF 2 – L1, the minimum value of the skin friction coefficient ($C_{f,\,min}$) was not observed for Re_h=75, revealing the influence of the cylinder on flow features and hence demonstrating that the recirculation zone was not formed at this Reynolds number. In the other BFSF 2 Runs, the value of $(C_{f,\,min})_1$ increased while its position was found to be upstream than for the BFSF 1. The second minimum value $(C_{f,\,min})_2$ was observed far away from the primary one at the bottom wall and its value was smaller than that of the primary $(C_{f,\,min})_1$.

5.3. Turbulent flow

5.3.1. Recirculation zone and reattachment length

In turbulent flow, the cylinder was installed at different locations downstream of the step (Table 3.9). Table 5.2 lists the value of the reattachment length for the BFSF 1 and BFSF 2 at different locations of cylinder. The size of the primary recirculation zone increased as the distance of the cylinder increased in the x-direction. Further, it was observed that for BFSF 2 – T1, a small third recirculation region (Lr_3) formed far away from the primary one on the bottom wall. As previously pointed out, Armaly et al. (1983), reported that the third recirculation zone was not found in their study for $Re_h > 1725$. However, for the BFSF 2 – T1, the third recirculation zone was observed even for Re_h =9,000.

Table 5. 2. Reattachment lengths of the BFSF 2 at different locations of cylinder in the turbulent flow compared with that of BFSF 1

	BFSF 1–T1	BFSF 2–T1	BFSF 2–T2	BFSF 2–T3	BFSF 2–T4	BFSF 2–T5
Lr_1/h	6.75	1.1	1.54	1.90	1.46	7.81
Lr_3/h	-	1.56	-	-	-	-

The cylinder pushed the primary recirculation zone upstream to the corner of the step and its length decreased. As previously pointed out, the third recirculation zone was caused by vortex shedding from the edge of the step. In BFSF 2 – T1 the flow directly incident cylinder, these vortices were thought to approach the wall, and the third recirculation zone was formed due to the sharp change of flow direction that eddies. In the other Runs, the third recirculation zone was missing.

5.3.2. Flow patterns

For the range of cylinder-diameter Reynolds number range 300 < Re_D < 3×10^5, the flow past a single cylinder developed, and the boundary layers separated from the front stagnation point. A fully developed turbulent wake downstream of the cylinder in this range of Reynolds number in flow past a cylinder, the vortex shedding process becomes fully turbulent in the wake and vortex street formed. For Re_D = 2,015, as the cylinder was placed at different locations downstream of the step, the step affected the near wakes of the cylinder by changing the dynamics of the vortex generation. As shown in Figure 5.8, at different locations of cylinders in the horizontal direction (BFSF 2 – T1, BFSF 2 – T2–, and BFSF 2 – T3) and in a location of the cylinder above the mid-plane of step (BFSF 2 – T4) two recirculation bubbles were observed downstream of the cylinder, with the size of the lower wake recirculation bubble being larger than that of the upper one. As the distance of the cylinder from the edge increased, two vortices behind the circular cylinder were slightly directed downwards. For BFSF 2 – T4 Run, the size of these vortices increased. For BFSF 2 – T5 Run, the flow coming from upstream of the step was not noticeably affected the cylinder and the step did not affect the near wake of the cylinder. Therefore, the separation streamlines from the top corner of the step resembled the counterpart for the unobstructed case.

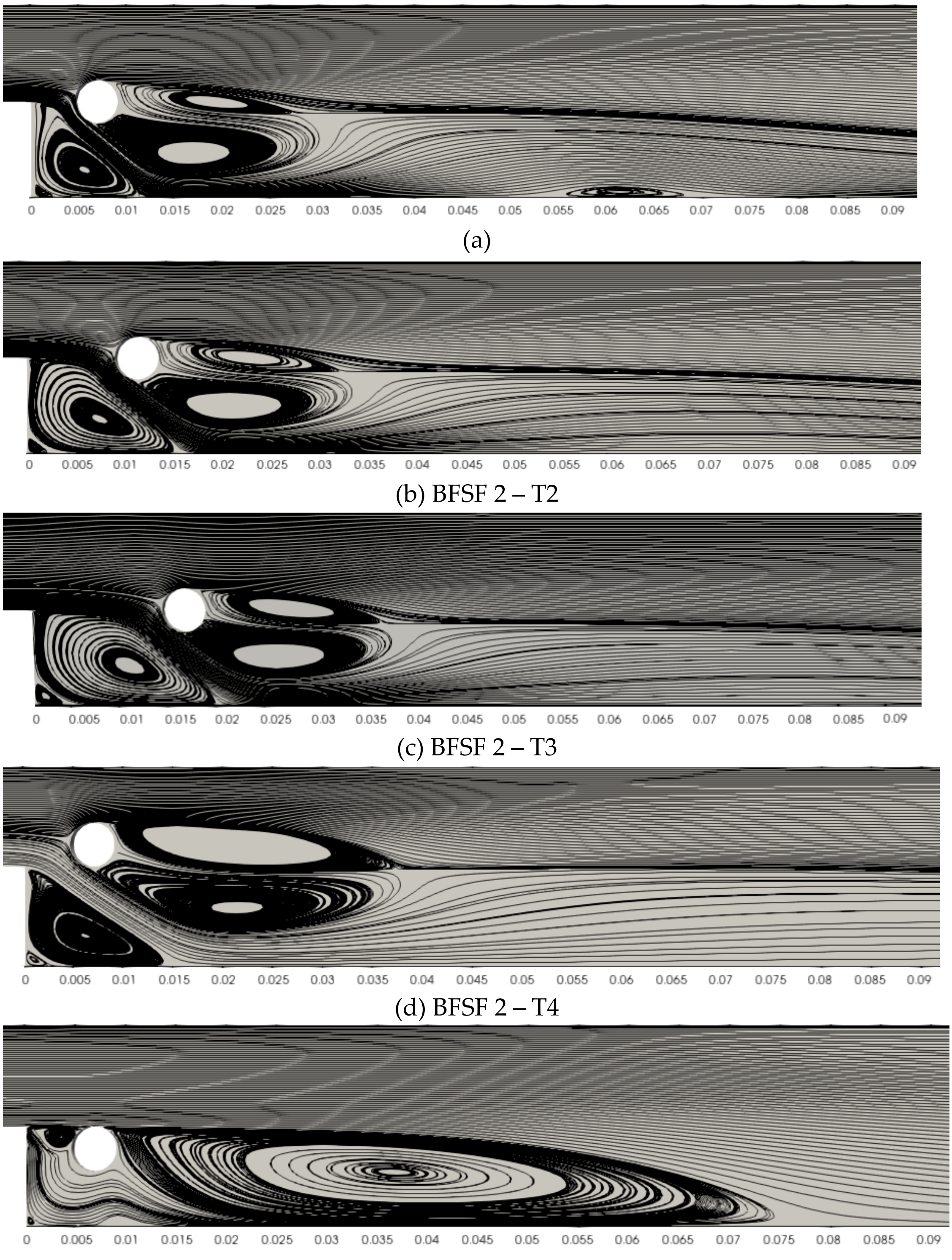

Figure 5.8. Streamlines of the flow in BFSF 2 for Re_D=2,015 (Re_h= 9,000) at different locations of cylinder (a) BFSF 2 - T1 (b) BFSF 2 – T2 (c) BFSF 2 – T3 (d) BFSF 2 – T4 (e) BFSF 2 – T5

5.3.3. Vertical profiles of the streamwise velocity

The distribution of the velocity for the two-dimensional BFSF at various turbulence models of turbulent flow is shown in Figure 5.10.

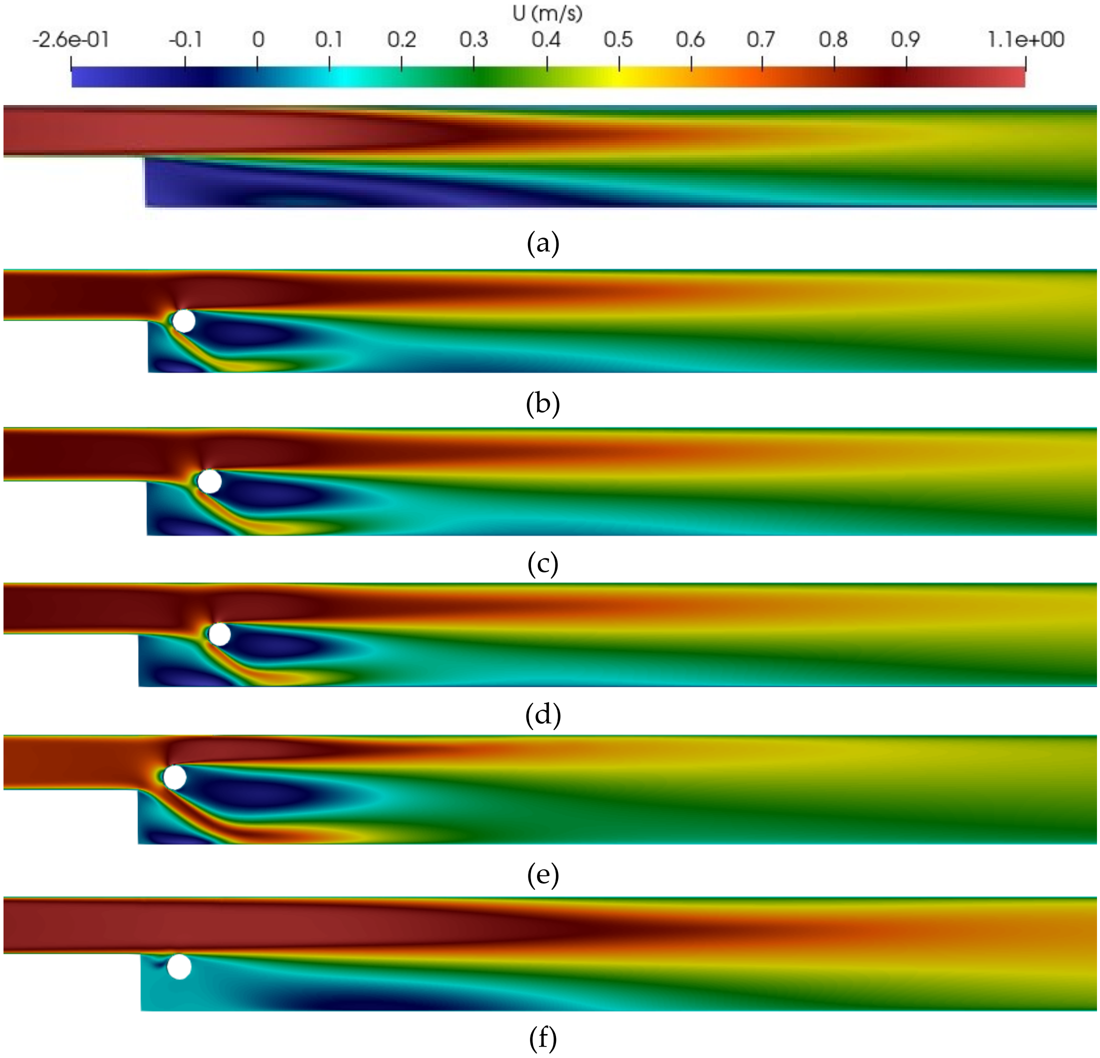

(a) (b) (c) (d) (e) (f)

Figure 5.9. u-Velocity distribution in BFSF2 at different locations of the cylinder compared with that of BFSF 1 (a) BFSF 1 - T1 (b) BFSF 2 - T1 (c) BFSF 2 – T2 (d) BFSF 2 – T3 (e) BFSF 2 – T4 (f) BFSF 2 – T5

The u-velocity profiles at different locations for the BFSF 1 and BFSF 2 were compared (Figure 5.10)

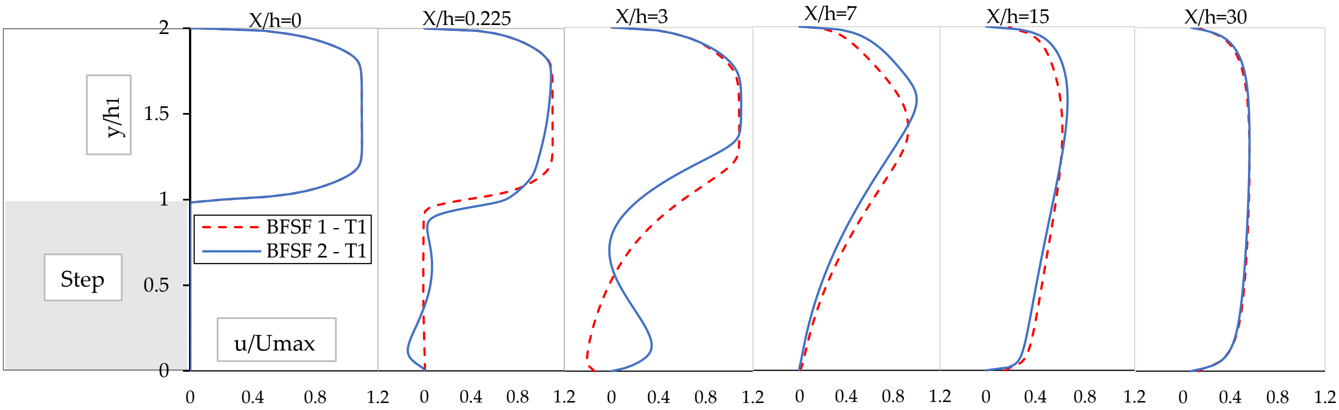
X/h=0
X/h=0.225
X/h=3
X/h=7
X/h=15
X/h=30
y/h1
Step
BFSF 1 - T1
BFSF 2 - T1
u/Umax

(a)

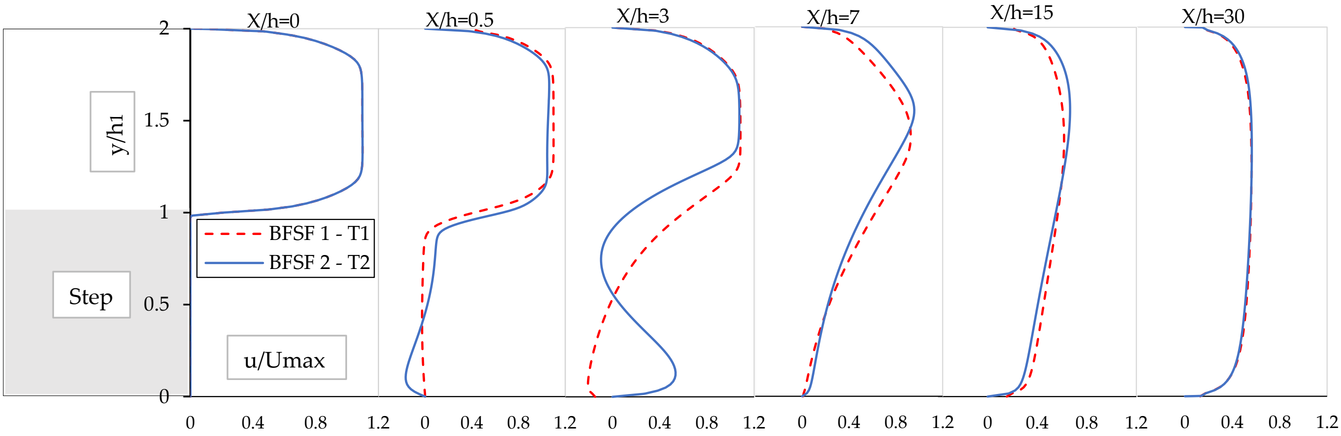
X/h=0
X/h=0.5
X/h=3
X/h=7
X/h=15
X/h=30
y/h1
Step
BFSF 1 - T1
BFSF 2 - T2
u/Umax

(b)

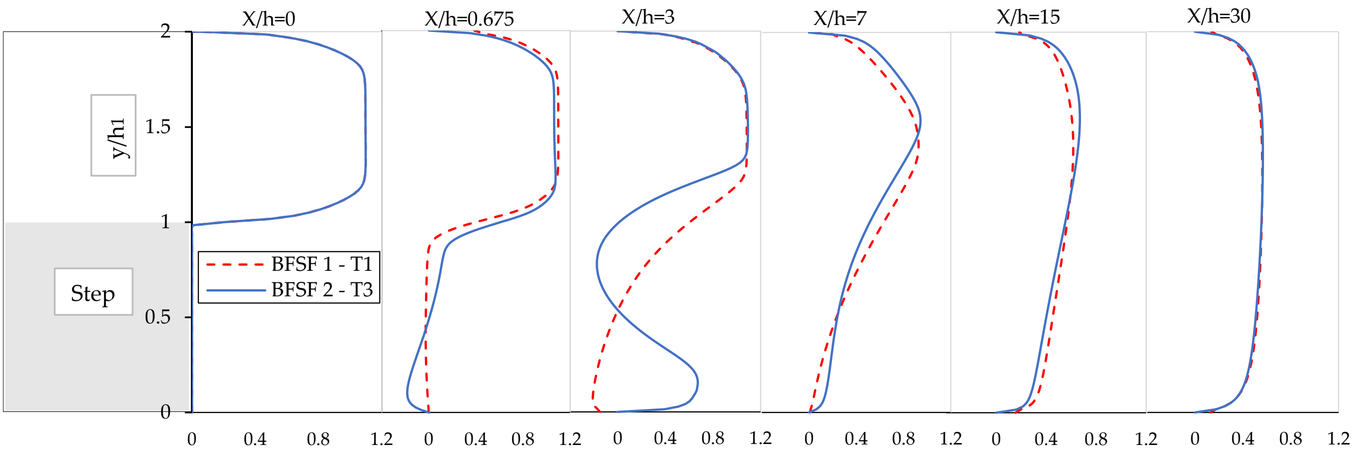
X/h=0
X/h=0.675
X/h=3
X/h=7
X/h=15
X/h=30
y/h1
Step
BFSF 1 - T1
BFSF 2 - T3

(c)

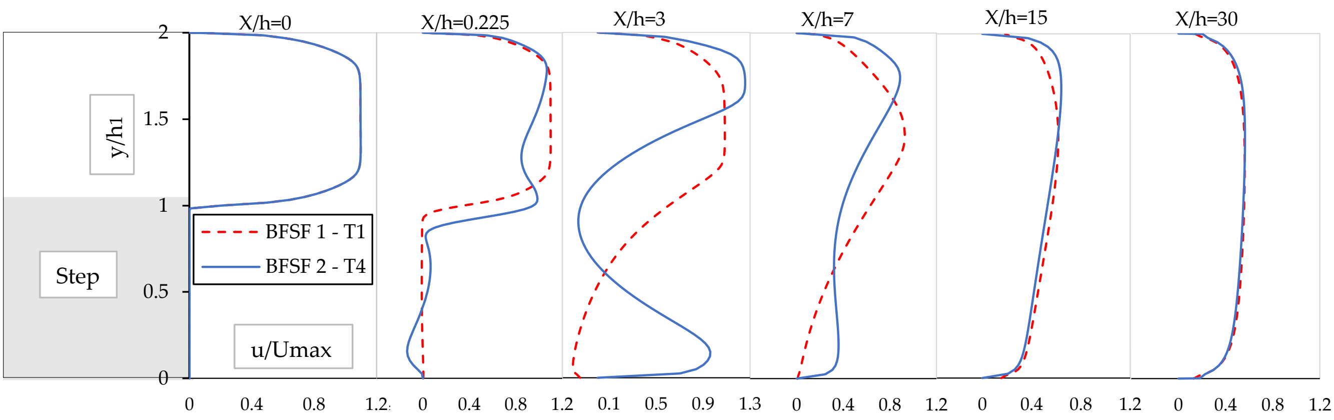

(d)

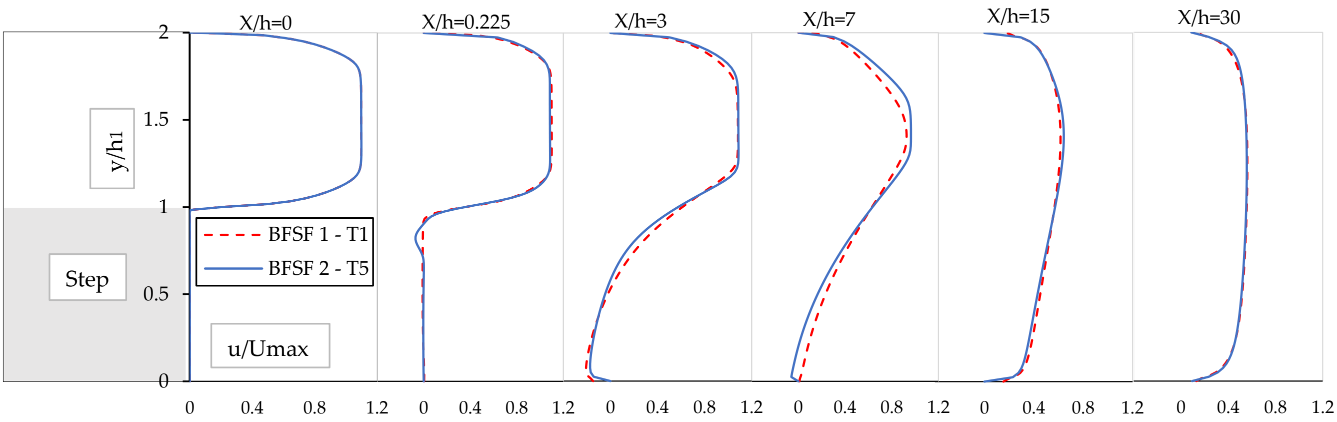

(e)

Figure 5.10. Dimensionless u-velocity (u/U_{max}) profiles of the BFSF 2 at different streamwise locations compared with that of BFSF 1. (a) BFSF 1 - T1 Vs. BFSF 2 – T1 (b) BFSF 1 - T1 Vs. BFSF 2 – T2 (c) BFSF 1 - T1 Vs. BFSF 2 – T3 (d) BFSF 1 - T1 Vs. BFSF 2 – T4 (e) BFSF 1 - T1 Vs. BFSF 2 – T5

For the BFSF 2 Runs, the distribution of vertical profiles of the streamwise velocity was changed. The cylinder affected the regular patterns of the vortex shed to rear of the cylinder and the location of the maximum velocities shifted toward the upper wall. Further downstream of cylinder and reattachment regions, the flow recovers its fully developed flow behavior. In all Runs, the flow was developed into a backward-facing step toward the outlet.

5.3.4. Skin friction distribution of the bottom wall

The distribution of the skin friction coefficient (C_f) at the bottom wall of the BFSF 2 is shown in Figure 5.11. Note that for the BFSF 2, the location was scaled using Lr_1 from the BFSF 1 – T1.

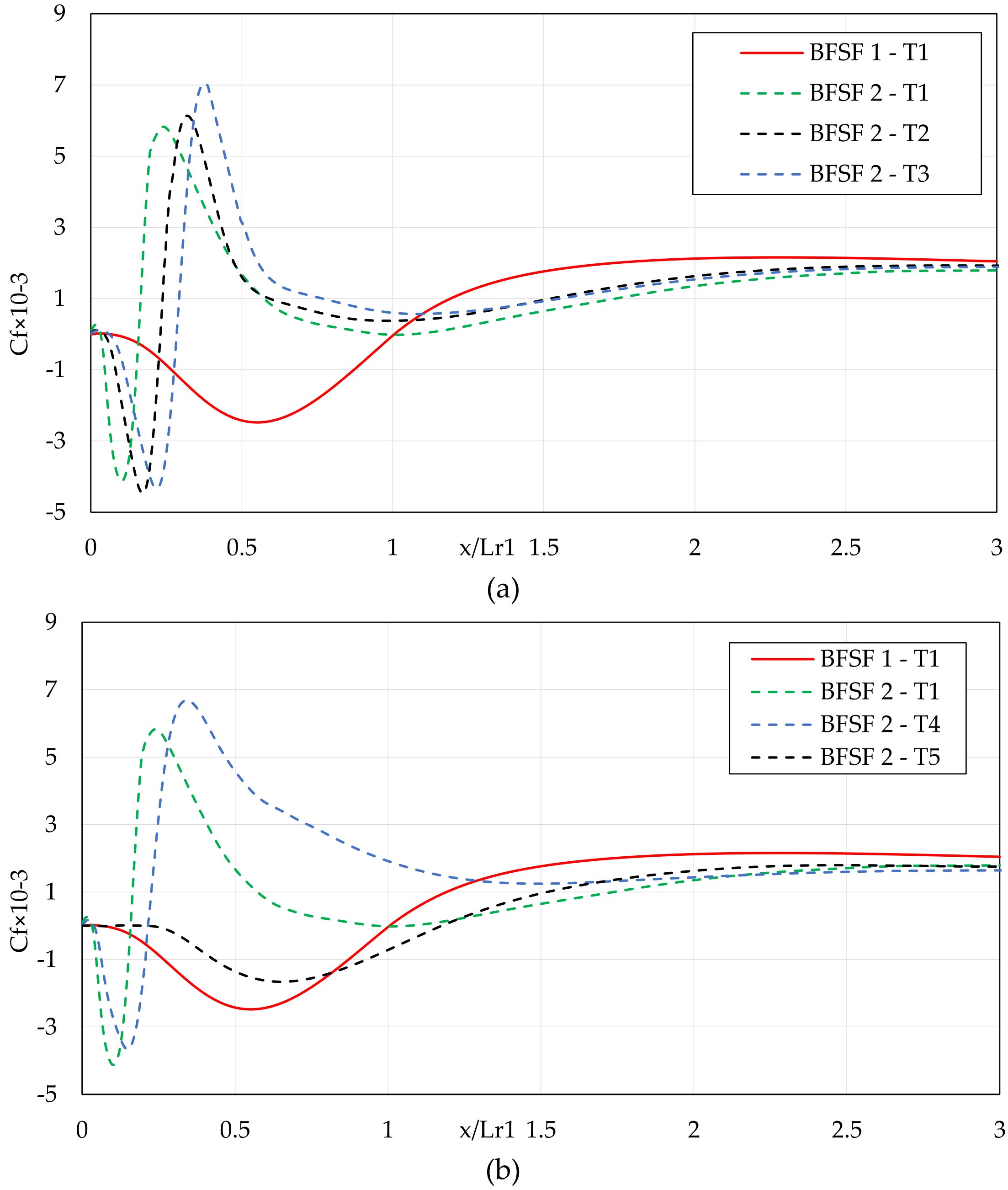

Figure 5.11. Longitudinal distribution of C_f at the bottom wall downstream of the step compare with BFSF 1 – T1, (a) different locations of the cylinder in the x-direction (b) different locations of the cylinder in the y-direction

For the BFSF 2 Runs, a minimum value of the skin friction coefficient was observed within the recirculating region. The C_f decreased and reached the minimum value in the recirculation zone and gradually recovers to positive values downstream of the reattachment point. For the BFSF 2 – T5, its behavior was the same as BFSF 1 – T1. In the BFSF 2 – T5, the minimum values of the skin friction coefficient were lower than those of the BFSF 1 – T1. However, for BFSF 2 – T1, BFSF 2 – T2, BFSF 2 – T3, and BFSF 2 – T4, two minimum values of the skin friction coefficient ($C_{f,\ min}$) occurred. The value of $(C_{f,\ min})_1$ increased while its position was found to be upstream than for the BFSF 1 – T1. The second minimum value $(C_{f,\ min})_2$ was observed far away from the primary one at the bottom wall and its value was smaller than that of the primary $(C_{f,\ min})_1$. Table 5.3 lists the value of the minimum value of $(C_{f,\ min})_1$, and its location for the BFSF 1 and BFSF 2.

Table 5. 3. Minimum value of skin friction coefficient $(C_{f,\ min})_1$ and its position $X_{(Cf,\ min)1}$ in the BFSF 2 of turbulent flow compared with that of BFSF 1

	BFSF1 – T1	BFSF2 – T1	BFSF2 – T2	BFSF2 – T3	BFSF2 – T4	BFSF2 – T5
$-(C_{f,min})_1 \times 10^{-3}$	2.48	4.12	4.33	4.47	3.66	1.66
$X_{(Cf,min)1}/L_{r1}$	0.561	0.102	0.107	0.219	0.150	0.651

5.3.5. Static pressure coefficient of the bottom wall

As already done in Part 1, the normalized pressure coefficient (C^*_p) was used for the comparison of pressure distribution. The normalized pressure coefficients (C^*_p) against the location scaled with the reattachment position, were compared in Figure 5.12.

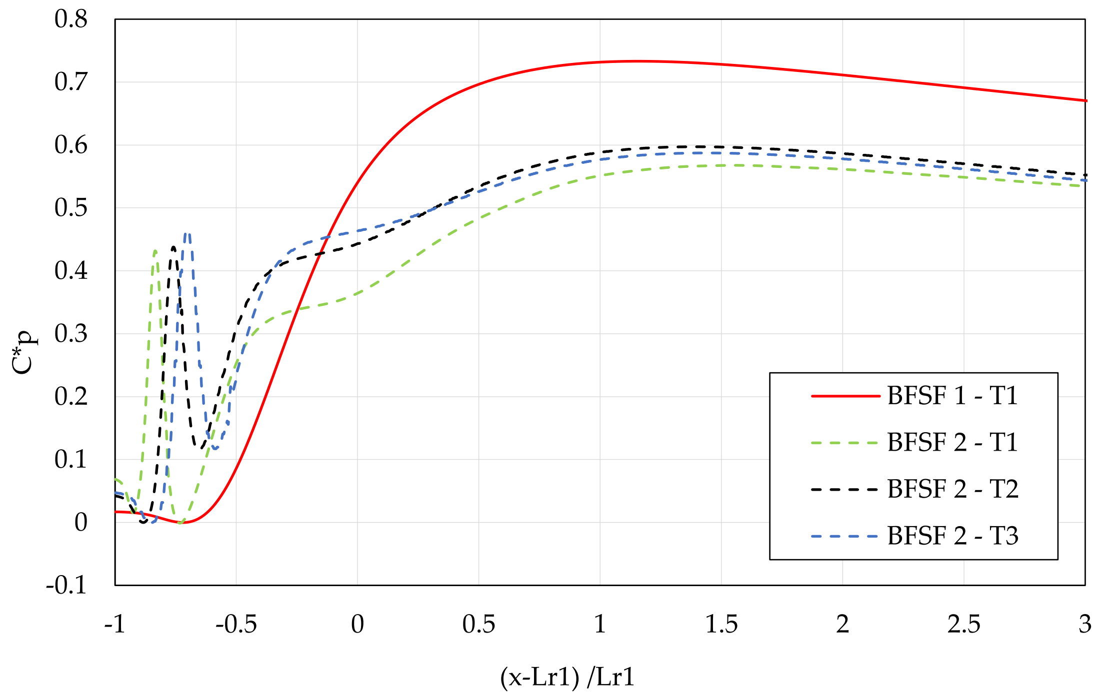

(a)

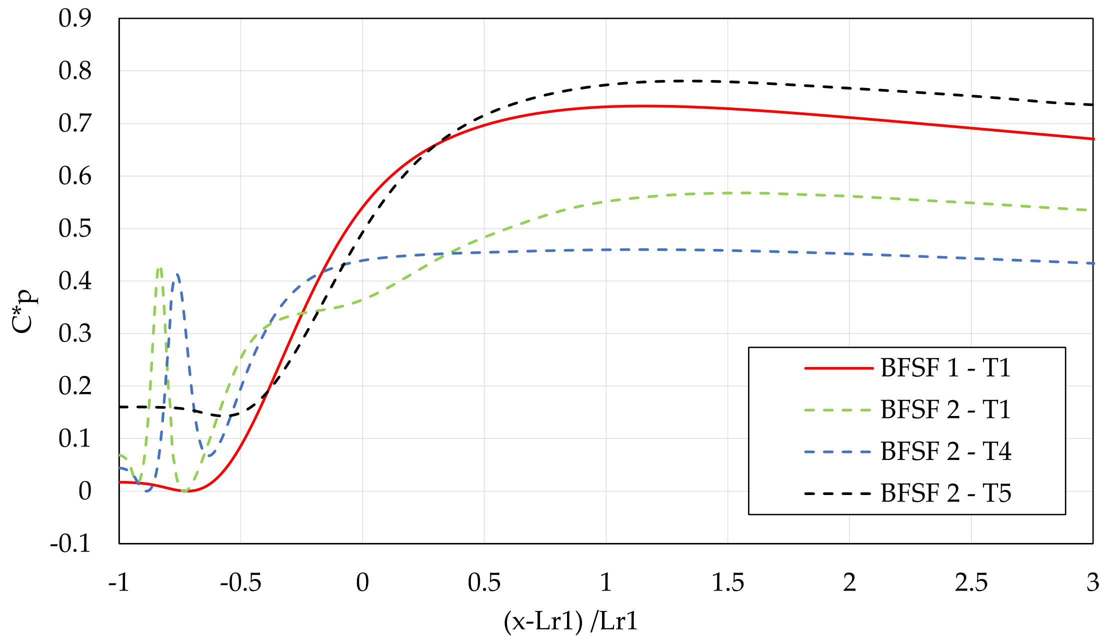

(b)

Figure 5.12. Longitudinal normalized pressure coefficient (C*p) of the bottom wall downstream of the step compare with BFSF 1, (a) different locations of the cylinder in the x-direction (b) different locations of the cylinder in the y-direction

In the BFSF 1 – T1, the static pressure increased starting from the corner of the bottom wall and a sharp increase of pressure occurred in the reattachment zone (from x=3h to x=7h). In the BFSF 2 Runs, a sharp increase in pressure occurred in front of the cylinder, however, the pressure behind the cylinder decreased. The distribution of pressure farther downstream remained relatively stable in the flow recovery process. The computed Cp values by the different tests of BFSF 2 are shown in Table 5.4.

Table 5. 4. Pressure coefficient (Cp) on the bottom walls at different Runs of BFSF 2 compared with that of BFSF 1 in turbulent flow

Case	C_P values range on the bottom wall
BFSF 1 – T1	-0.141 to 0.329
BFSF 2 – T1	-0.39 to 0.115
BFSF 2 – T2	-0.245 to 0.199
BFSF 2 – T3	-0.214 to 0.205
BFSF 2 – T4	-0.139 to 0.336
BFSF 2 – T5	-0.709 to -0.153

The C_P values computed for BFSF1 – T1 at the bottom wall ranged from -0.141 to 0.329 and its distribution agreed with literature experimental data (Driver and Seegmiller 1985, Kim et al. 1980, Westphal et al. 1984) and numerical results (Kopera et al. 2011). In the BFSF 2, the minimum and maximum values of the pressure coefficients were lower than those in the BFSF 1. The cylinder affected the distribution of pressure along the bottom wall and the Cp values ranged from -0.709 to 0.336 on the bottom wall. In the BFSF 2, the variation of the pressure downstream of the cylinder at the bottom wall could be due to: the streamline curvature and the high turbulence intensity. The average value of Cp downstream of the reattachment point was smaller than that in the BFSF 2 if compared to the BFSF 1.

5.3.6. Surface pressure distributions of cylinder

Surface pressure distributions of the cylinder in crossflow, where it was mounted downstream of the step at different locations are shown in Figure 5.14.

a)

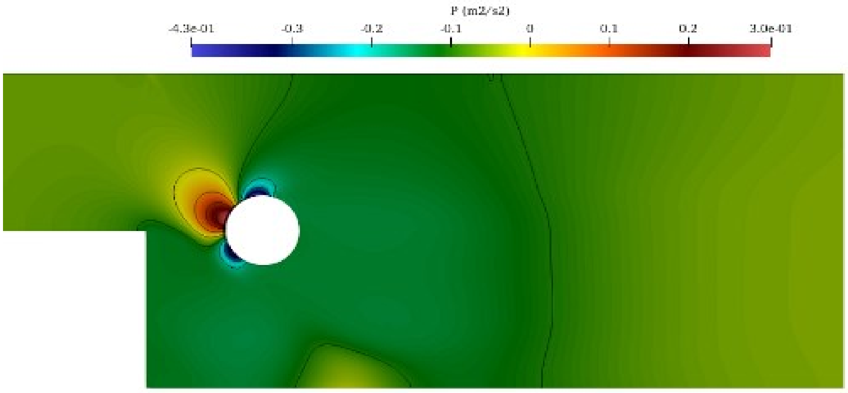

b)

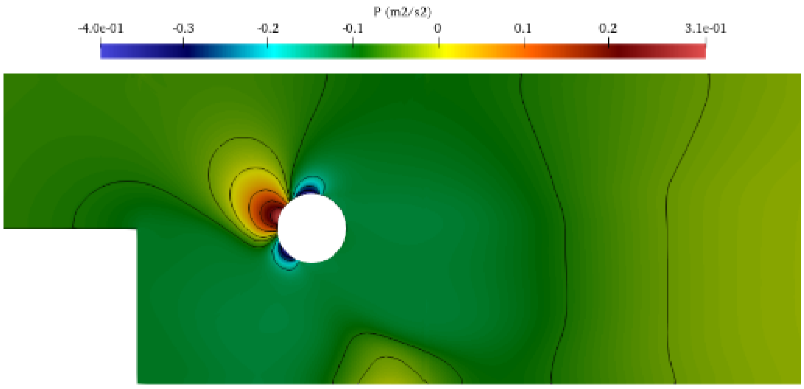

c)

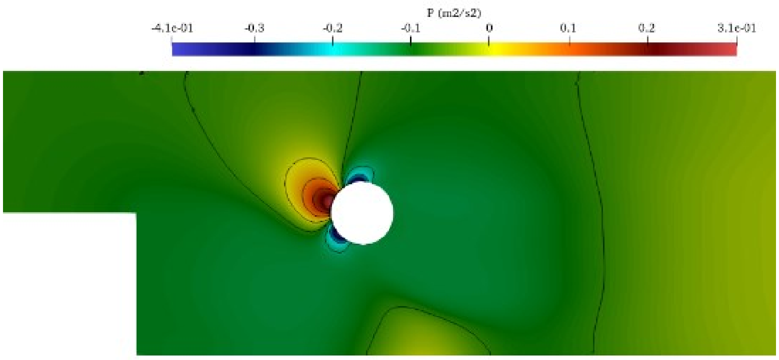

d)

e)

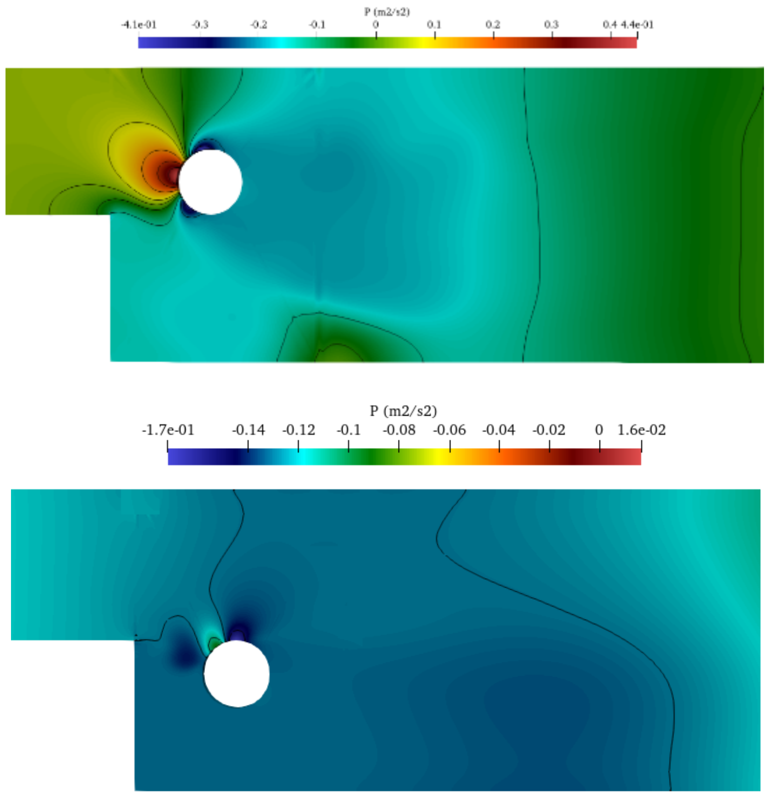

Figure 5.13. Distribution of surface pressure of cylinder in the BFSF 2 in turbulent flow(a) BFSF 2 – T1 (b) BFSF 2 - T2 (c) BFSF 2 - T3 (d) BFSF 2 - T4 (e) BFSF 2 – T5

The step affected the pressure distribution around the cylinder by changing the maximum and minimum points of surface pressure, which moved away from the centerline. The largest pressure was induced on the front side of the cylinder where the incoming flow decelerated while being deflected around the top of the cylinder. The lowest pressures were recorded at the sides of the cylinder but rather just at the separation points. As expected, the largest pressure was found for BFSF 2 – T4 when the cylinder was positioned above the step and the incoming flow crossed with the cylinder.

5.3.7. Turbulent kinetic energy

In the RANS turbulence model, the turbulent kinetic energy (k) is given directly by the resolution of its transport equation. Figure 5.14 shows the distribution of turbulent kinetic energy in the BFSF 1 and BFSF 2 for different locations of the cylinder.

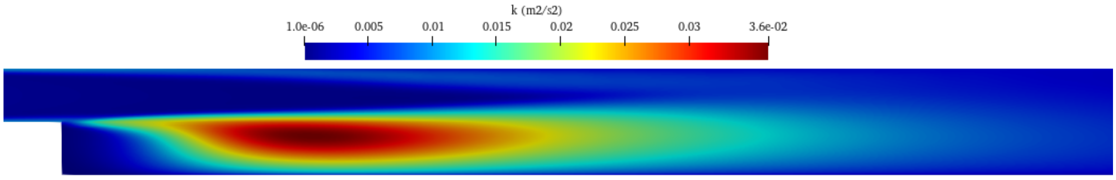

(a)

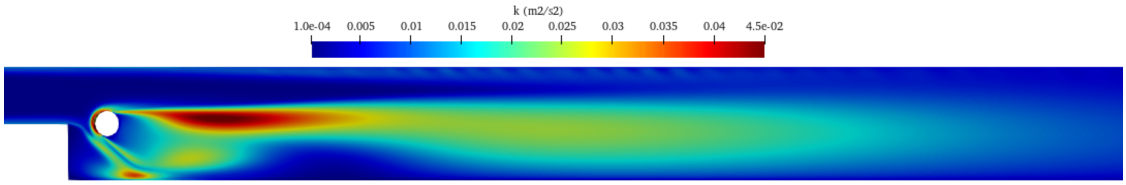

(b)

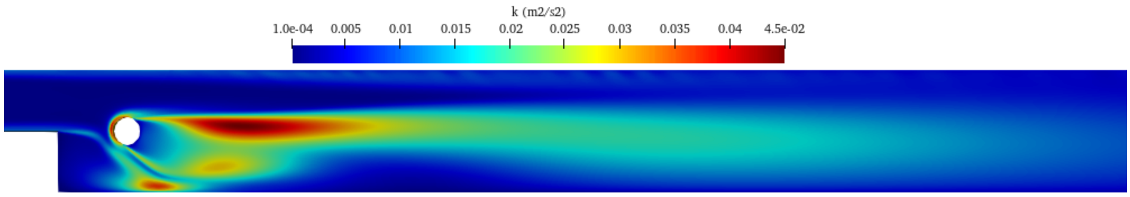

(c)

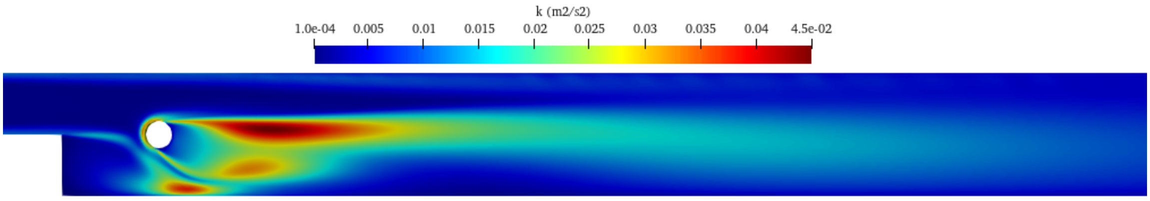

(d)

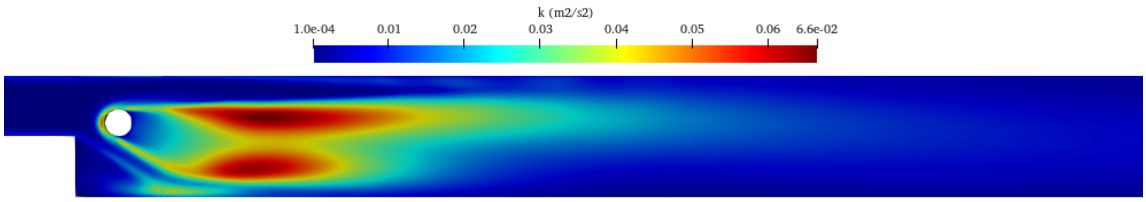

(e)

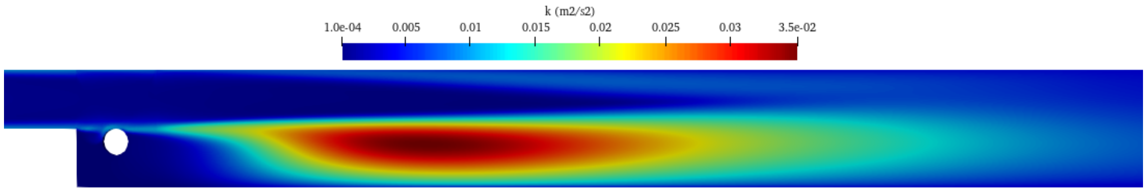

f)

Figure 5.14. Distribution of turbulent kinetic energy (k) in the BFSF 2 and compared with BFSF 1 in turbulent flow (a) BFSF 1 – T1 (b) BFSF 2 – T1 (c) BFSF 2 – T2 (d) BFSF 2 – T3 (e) BFSF 2 – T4 (f) BFSF 2 – T5

For BFSF 1 – T1 and BFSF 2 – T5, the maximum turbulent kinetic energy was below the mid-plane of the step, in regions of high shear flow. While, for other the BFSF 2 Runs, the cylinder changed the distribution of turbulent kinetic energy, and the maximum turbulent kinetic energy was shifted above the mid-plane of the step. In the BFSF 1 – T1 and BFSF 2 – T5, the turbulent kinetic energy decreased monotonically starting from the step edge in the x-direction. However, TKE was amplified downstream of the cylinder in midplane and the region of high TKE was also bounded by the cylinder. In the vertical plane, the region of high TKE downstream of the cylinder contained two subregions of high TKE and it was in the highest value when the cylinder was above the mid-plane of step (BFSF 2 – T4). These subregions were even better delimited in Figure 5.15 showing the value of maximum turbulent kinetic energy profiles. In figures $(k_{max}/(U_{max})^2$ profiles were measured in a vertical plane in the section where the maximum value of turbulent kinetic energy was found. The top subregion of high flow turbulence was mostly due to the passage of flows inside the separated shear layers of the cylinder.

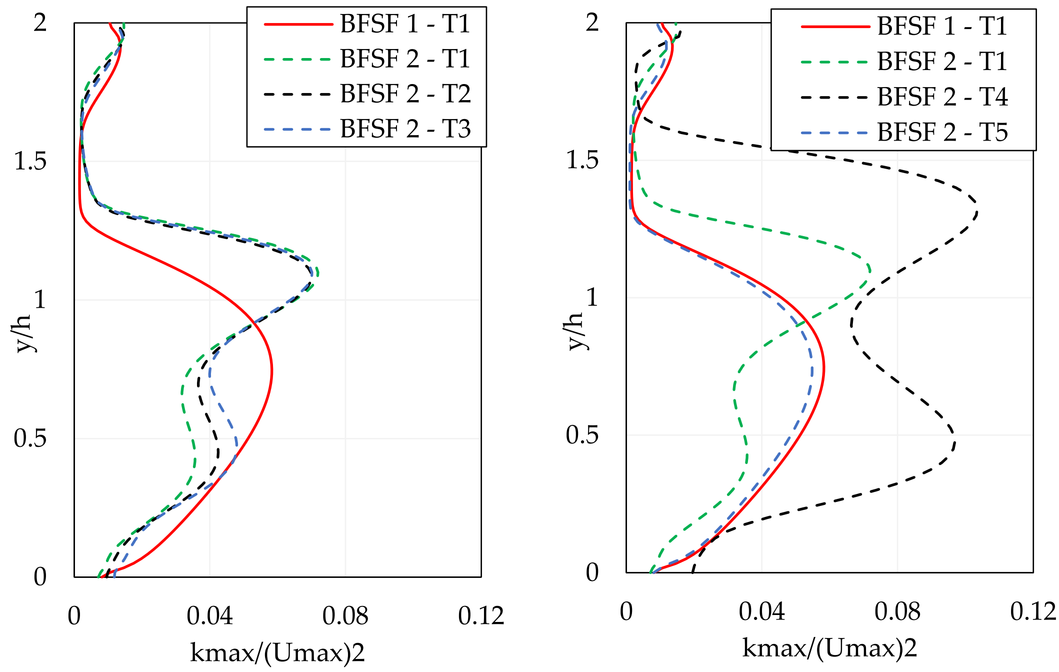

(a) (b)

Figure 5.15. Dimensionless maximum turbulence kinetic energy downstream of the step compare with BFSF 1, (a) different locations of the cylinder in the x-direction (b) different locations of the cylinder in the y-direction

5.4. Discussion

Flow downstream of the step is complex and the presence of a cylinder creates eddies, transverse flows, velocity gradients, and other spatial flow patterns. A better understanding of how the cylinder interacts to create spatially varying flows downstream of the step leads to the quantification of its features. The key findings from this study are:

Recirculation zone: In the BFSF 1, three recirculation zone were observed: primary recirculation zone on the bottom wall in laminar and turbulent flow; second recirculation zone at the upper wall for Re_h>300; and third recirculation zone on the bottom wall in the early part of the transitional regime. In laminar flow, the cylinder pushed the primary recirculation region upstream to the corner of the step and its length decreased, while the second recirculation zone near the upper wall was missing for BFSF 2. In the BFSF 2, the third recirculation zone was observed even for laminar and turbulent flow when a cylinder was positioned at a diameter distance from the step edge and its location was upstream than in the BFSF 1. In turbulent flow, the size of the third recirculation zone was smaller than that of laminar flow. As the cylinder was placed far away from the step and above or below the step, the third recirculation zone was missing.

Cylinder wake: In laminar flow, the step modified the structure of the flow past the cylinder, leading to an asymmetric wake distribution. A large portion of these vortices shifted toward the below cylinder. In turbulent flow, when a cylinder was positioned along the step edge or above the step edge, flow passing over the cylinder suppressed the formation of the von Kármán vortex street, and two vortices formed behind the cylinder in different sizes, and their location shifted towards the bottom wall. As the cylinder was located below the step, the structure of flow downstream of step was similar to BFSF 1, and only primary recirculation zone was observed.

Streamwise velocity: The cylinder increased the velocity due to a narrow cross-section downstream of the cylinder. The location of the maximum velocity shifted towards the middle of the channel in both laminar and turbulent flow.

Skin friction distribution: The wall shear stress is associated with the skin friction coefficient at the bottom wall. A minimum value of skin friction coefficient ($C_{f,\,min}$) at the bottom wall occurred due to the recirculating flow. In the BFSF 1, a minimum value of skin friction coefficient ($C_{f,\,min}$) at the bottom was observed in both laminar and turbulent flow. However, in the BFSF 2, two minimum values of skin friction coefficient $(C_{f,\,min})1$ and $(C_{f,\,min})2$ were observed due to the two recirculation zones for Re_h>75. The cylinder downstream of the step produced significantly high minimum and maximum values of the skin friction coefficient at the bottom wall than that without the cylinder.

Pressure distribution: The cylinder affected the distribution of pressure along the bottom wall. In the BFSF 2, the minimum and maximum values of the pressure coefficients were lower than those in the BFSF 1. However, the average value of pressure coefficients downstream of the reattachment point was smaller than that in the BFSF 2. In addition, the step affected the distribution of the surface pressure of the cylinder by moving the largest pressure region to the top of the cylinder.

Turbulent kinetic energy: In the BFSF 1, the maximum turbulent kinetic energy was found downstream of the step, below the mid-plane of the step. However, in the BFSF 2, the cylinder increased the turbulent kinetic energy and the location of the maximum TKE shifted toward the centerline of the channel. The highest regions of TKE were found in the wakes of the cylinder and its value was higher than that of BFSF 1.

Chapter 6 Analysis of results - Part 2:

Solute transport

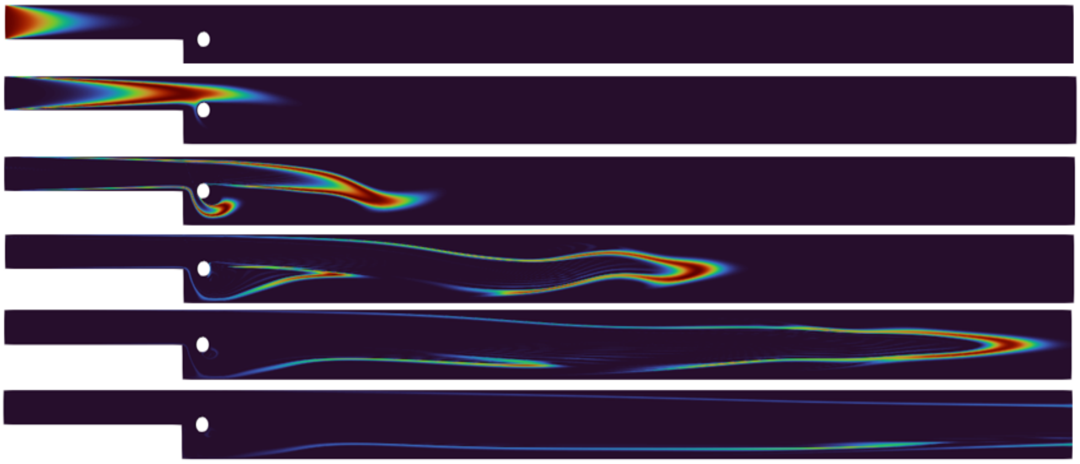

In this chapter, the results of the solute transport due to the pulse load of it in laminar flow downstream of the step are presented

6.1. Introduction

Solute transport in streams and rivers is significantly affected by the presence of expansion due to geometrical irregularities, that may have both natural and anthropic origins. Solute transport in streams is strongly related to river characteristics, such as mean flow velocity, velocity distribution, secondary currents, and turbulence features. These parameters are mainly determined by the river morphology and the discharge conditions. Step-like geometries are characterized by mean flow velocity in the mainstream direction approximately equal to zero and by exchange processes of solutes with the mainstream (Gualtieri 2008). This chapter presents the preliminary results of a numerical study undertaken to investigate the fundamental solute transport phenomena around and inside a simplified geometry BFSF, representative of flow in the step channel with a cylindric obstacle.

6.2. Set-up of tracer transport simulations

As previously noted in Chapter 2 (section 2.4), the code was developed, and the ADE equation was linked to the RANS equation. The tracer study was carried out for a pulse release at the inlet of the backward-facing step, where the concentration at the inlet C_{in} changed over time as a pulse concentration type boundary condition, i.e. Eq. (6.1), was applied (Gualtieri 2009a):

$$C_{in}(t)=C_0\, exp\,(-(t-3)^2) \qquad (6.1)$$

Where t is time (s) and C_0= 100 mg/l or 0.1 kg/m^3 (Gualtieri 2009a). Eq 6.1 is believed to better reproduce the input conditions in the physical model.

In this study, a typical case of the instantaneous and uniform tracer of a laminar flow was considered. The specific objective of this chapter is to quantify and illustrate the effect of cylindrical obstacles on tracer transport downstream of the step in the recirculation zone. The study was conducted at a step-height Reynolds number Re_h=336 for two-dimensional classical backward-facing step flow (BFSF 1) and backward-facing step with a cylinder (BFSF 2). As previously pointed out (section 3.3.1) for laminar flow, a cylinder with a diameter (D) was set at one cylinder-diameter distance from the step edge (x=D) in the x-direction. To reduce computational time for the tracer transport study, the domain downstream of step was reduced to L_d = 30 h for both cases BFSF 1 and BFSF 2. Figure 6.1 shows the computational domain for the tracer study.

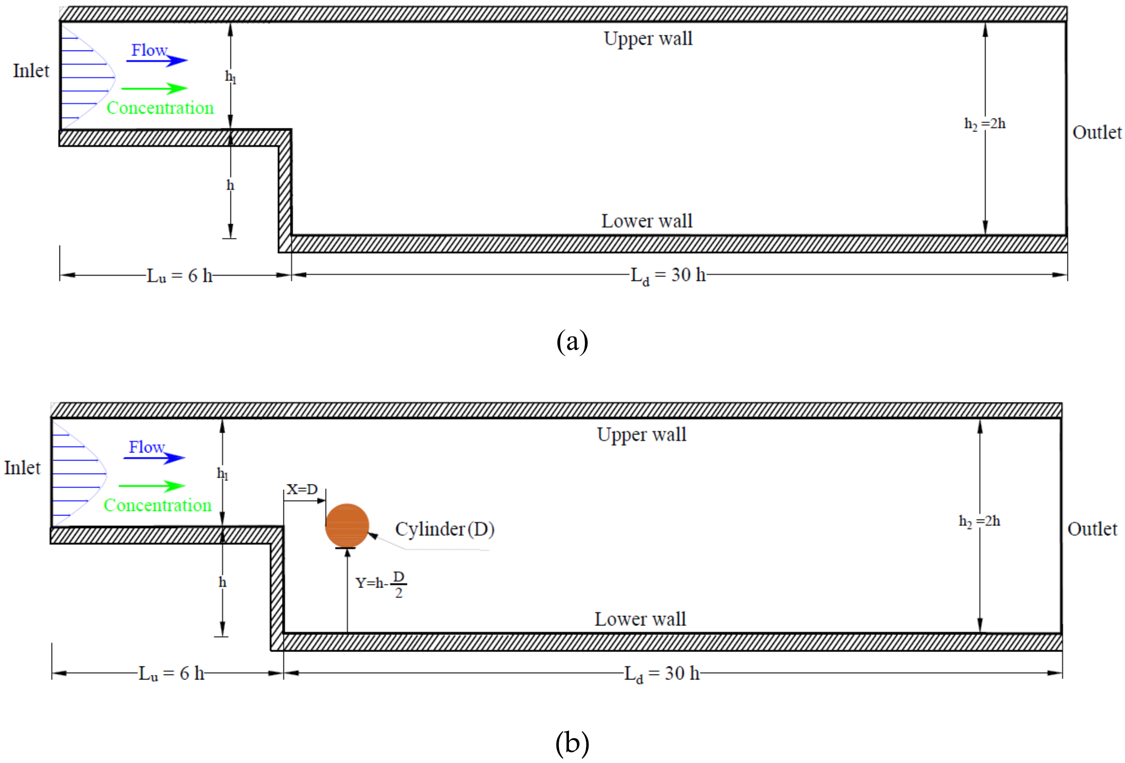

Figure 6.1. Computational domain of tracer transport study (a) BFSF1 (b) BFSF2. h, h1, and h2 represent the step height, inlet-section height, and outlet-section height, respectively, with the expansion ratio ($ER=h_2/h_1$) of 2.

6.3. Analysis of the tracer field

The tracer transport study was carried out for pulse release of the BFSF 1 at Re_h=336. The distribution of the concentration over the time in the BFSF 1 is shown in Figure 6.2.

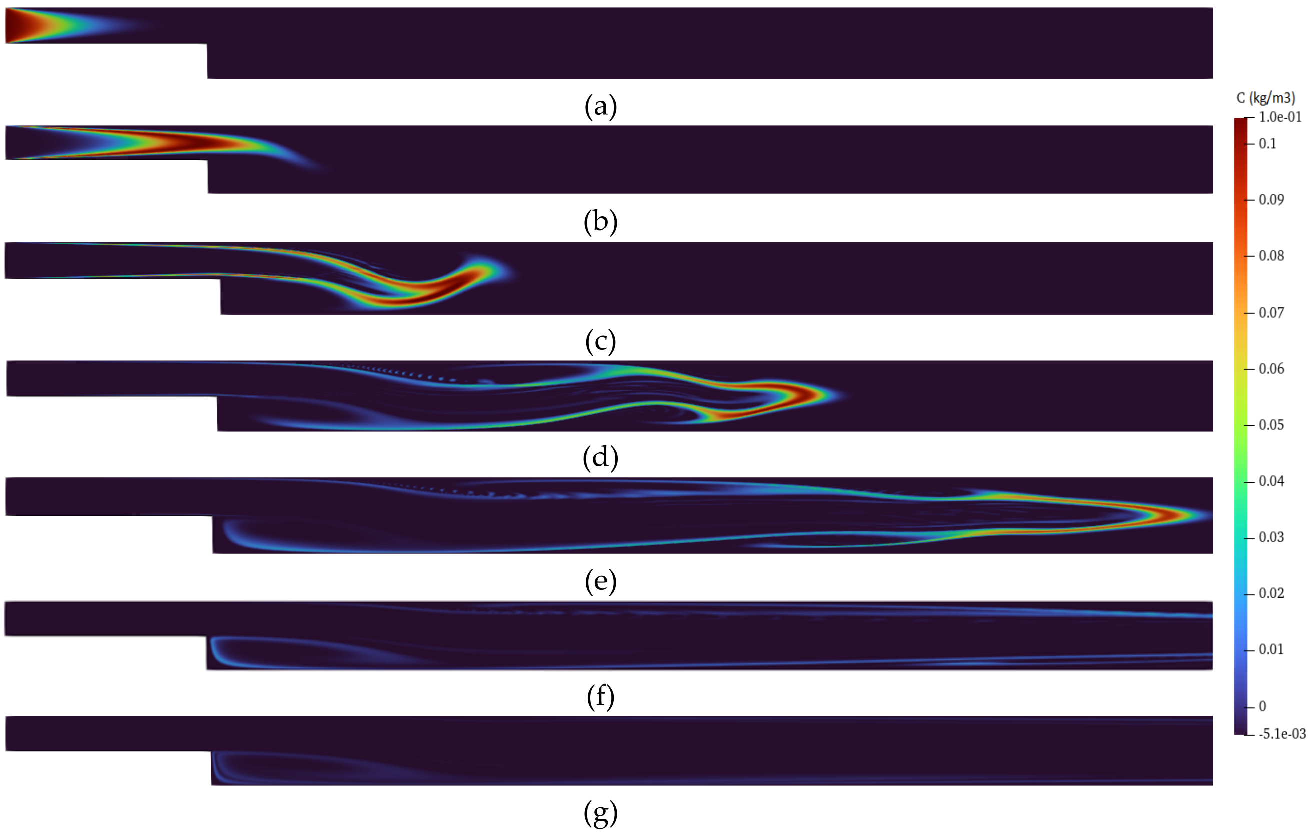

Figure 6.2. Concentration field in the BFSF 1 at different time steps in Re_h=336 (a) t = 3 s (b) t = 6 s (c) t = 10 s (d) t = 20 s (e) t = 30 s (f) t = 50 s (g) t = 100 s

For the BFSF 1, the solute injection peak occurred at t=3 s and reached downstream of the step at t=6 s. From t=10 s to t=30 s the initial volume of tracer moved downstream and reached the outlet. At t=20 s, the result indicated that inside the recirculation zone, the solute was reduced to a small zone downstream of the step. While a large amount of solute was left of the domain from t=30 s to t=100 s, a small solute was still in the geometry. As a cylinder was placed downstream of the step, the process of transport was changed. The distribution of the concentration over the time in the BFSF 2 is shown in Figure 6.3.

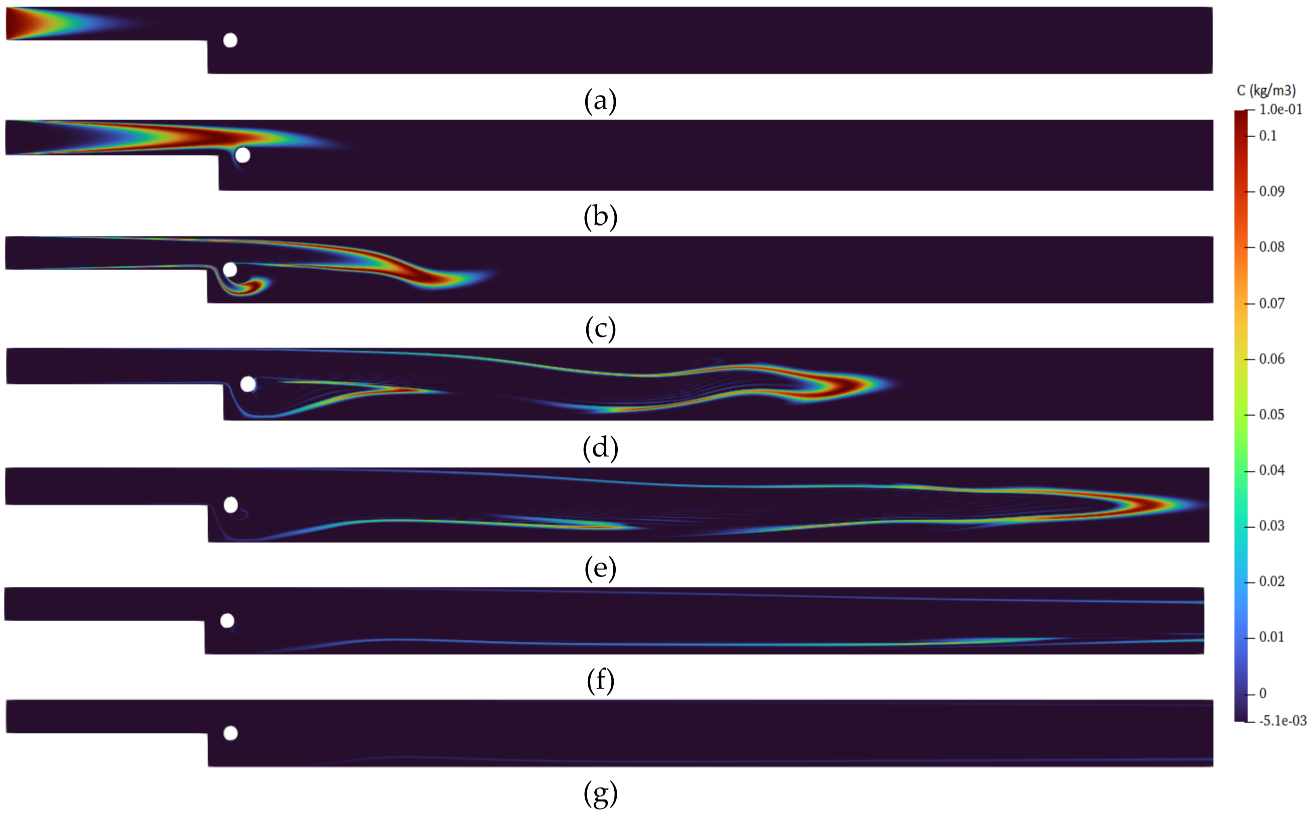

Figure 6.3. Concentration field of BFSF 2 at different time steps in Re_h=336 (a) t = 3 s (b) t = 6 s (c) t = 10 s (d) t = 20 s (e) t = 30 s (f) t = 50 s (g) t = 100 s

For the BFSF 2, the solute peaked at t=3 s and reached downstream of the step at t=6 s. At t=10 s, some portion of the solute was directed towards the below of the cylinder and a large portion of them continued to move in the x-direction. At t=20 s, some solute was confined in the region below the cylinder, which region included the vortex of the cylinder. From t=30 s to t=100 s the initial material volume of solute moved towards the walls and downstream. At t=100 s, while a large amount of the tracer washed out of the domain, some small solute was still in the computational domain. In the next section, the distribution of the solute trapped in the recirculation zone is discussed in detail.

6.3.1. Tracer transport in the recirculation zones

As discussed in Chapter 5, for the BFSF 1 at Re_h=336, the primary and second recirculation zones were formed on the bottom and upper walls, respectively. For the BFSF 2, the primary and third recirculation zone was observed on the bottom wall. Figure 6.4 shows the concentration field at t=20 s for the BFSF 1 and BFSF 2 and its behavior in recirculation zones.

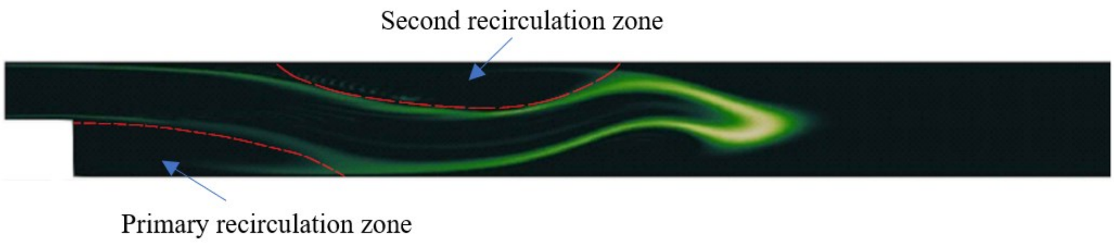

(a)

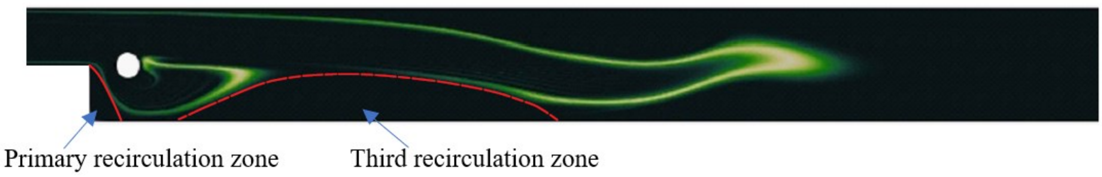

(b)

Figure 6.4. Concentration field in recirculation zones of BFSF 1 compared with BFSF 2 at t=20 s (a) BFSF 1 (b) BFSF 2. (Red dotted lines determine the recirculation zones)

As shown in Figure 6.4 a, for the BFSF 1, the tracer passed out of the primary and secondary recirculation zones. For the BFSF2, the tracer close to the cylinder deviated and then it was advected downstream of the cylinder and downstream of the separation point, the solute had high concentration. For both BFSF 1 and BFSF 2, downstream of the reattachment point, the tracer farther from the walls was advected downstream more rapidly than elements closer to the walls. After 100 seconds, in both BFSF 1 and BFSF 2, a large amount of tracer left the geometry, however, some tracer was confined in the geometry in the recirculation zones. Figure 6.5 shows the concentration field in recirculation zones at t=100 s for both BFSF 1 and BFSF 2.

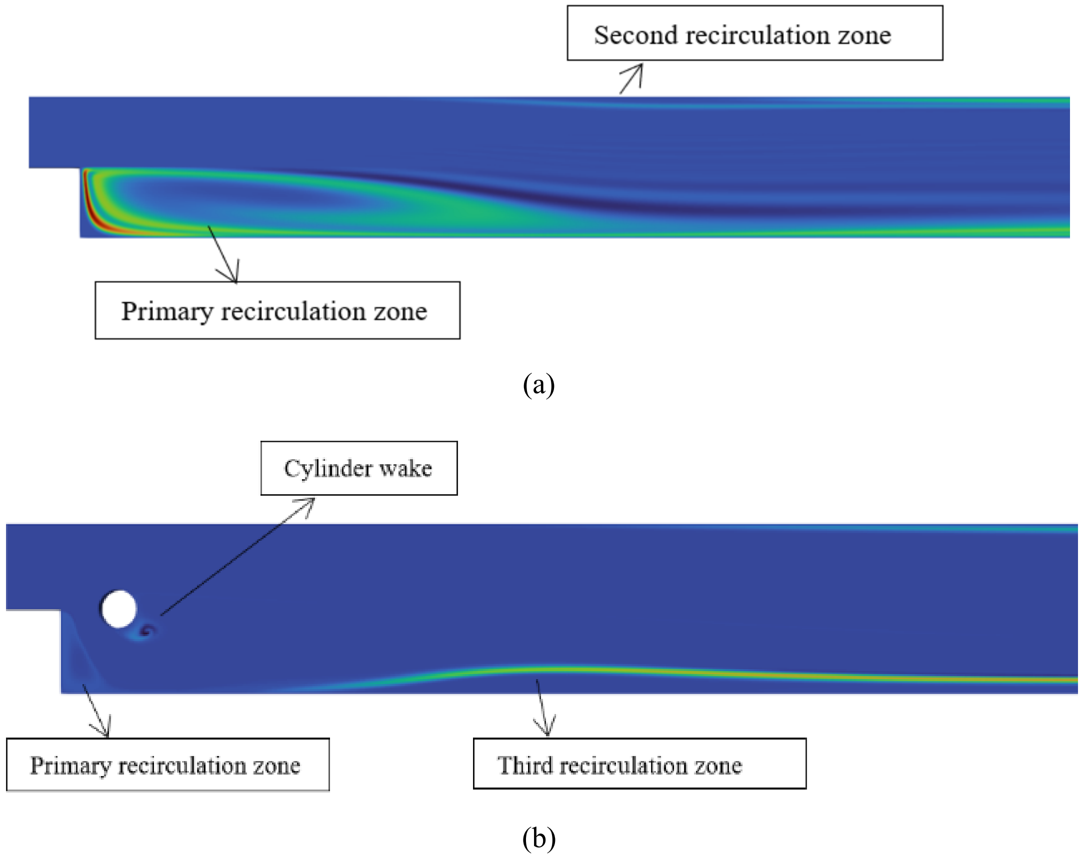

Figure 6.5. Concentration field in recirculation zones of BFSF 1 compared with BFSF 2 at t=100 s (a) BFSF 1 (b) BFSF 2

As shown in Figure 6.4-a, for the BFSF 1, the tracer decreased due to downwardly directed flow downstream of the step and a large part of the tracer was carried slightly downstream. The dividing streamline divided the region of high solute into two parts that were inside and outside the primary recirculation zone. The tracer that diffused across the dividing streamline or was in fluid elements that pass out of the recirculation zones moved towards the wall. Some portion of tracer that did not pass across the dividing streamline before reaching the vicinity of the reattachment point moved back upstream along the wall towards the step. It was trapped in the primary recirculation zone.

For the BFSF 2, the tracer was trapped in the recirculation zones. The primary recirculation zone was smaller than that of the BFSF 2 if compared to the BFSF 1. As a result, a small amount of the tracer was trapped in the primary recirculation zone. In addition, a small part of the tracer was in the cylinder wake and the third recirculation zone at the bottom wall.

In both BFSF 1 and BFSF 2, the transport of the tracer across the dividing streamline was the result of two effects. First, at any instant, the tracer can diffuse across a streamline. Moreover, the separation streamline here is unsteady, with its point farthest from the fluid elements lying inside the recirculation zone will later lie outside that zone, where they are carried downstream.

6.3.2. Residence Time Distribution (RTD)

The Residence Time Distribution (RTD) is defined as the probability distribution of time that fluid materials stay inside unit operations in a continuous flow system (Gao et al. 2012). The residence time distribution (RTD) curves at seven different locations in the BFSF 1 and BFSF 2 was considered. The values of the concentration were calculated over time, i.e., the flow-through curve (FTC).

The location of the points is shown in Figure 6.6 for both BFSF 1 and BFSF 2. Point 1 is in the inlet, point 2 is above the step, whereas points 3, 4, and 5 are in recirculation zones and cylinder wake, point 6 is in the middle of the channel, and point 7 is located in the outlet of the channel. Figure 6.7 presents location of the points where the concentration was analyzed for BFSF 1 and BFSF 2.

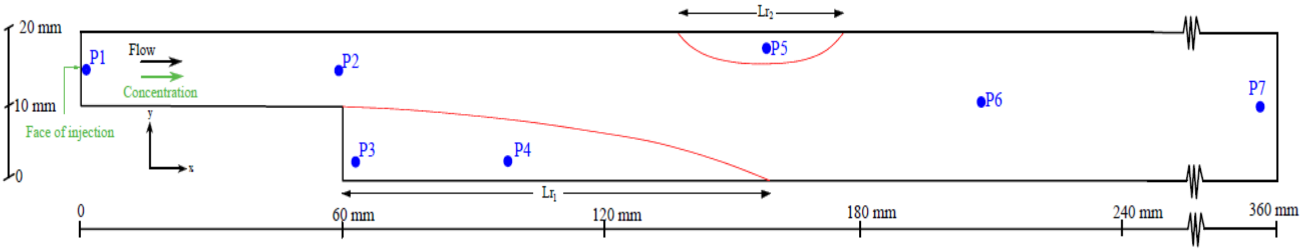

Point	X(mm)	Y (mm)
P1	0	15
P2	60	15
P3	65	3
P4	105.5	3
P5	152.5	17
P6	200	10
P7	360	10

(a)

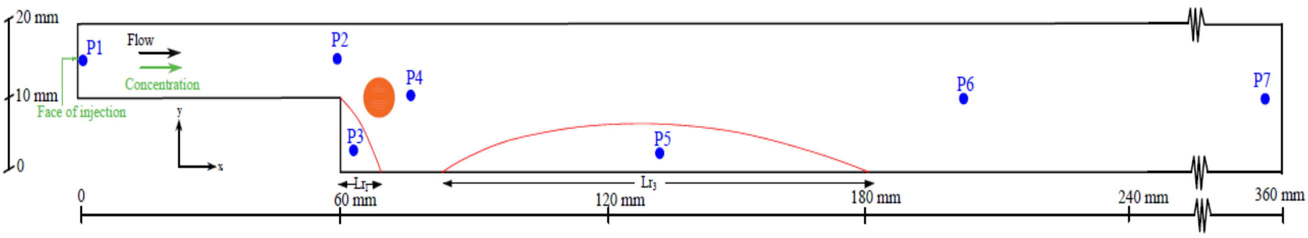

Point	X(mm)	Y (mm)
P1	0	15
P2	60	15
P3	65	3
P4	73.5	10
P5	132.5	3
P6	200	10
P7	360	10

Figure 6.6. Location of points where the concentration was analyzed (a) BFSF 1 (b) BFSF 2.

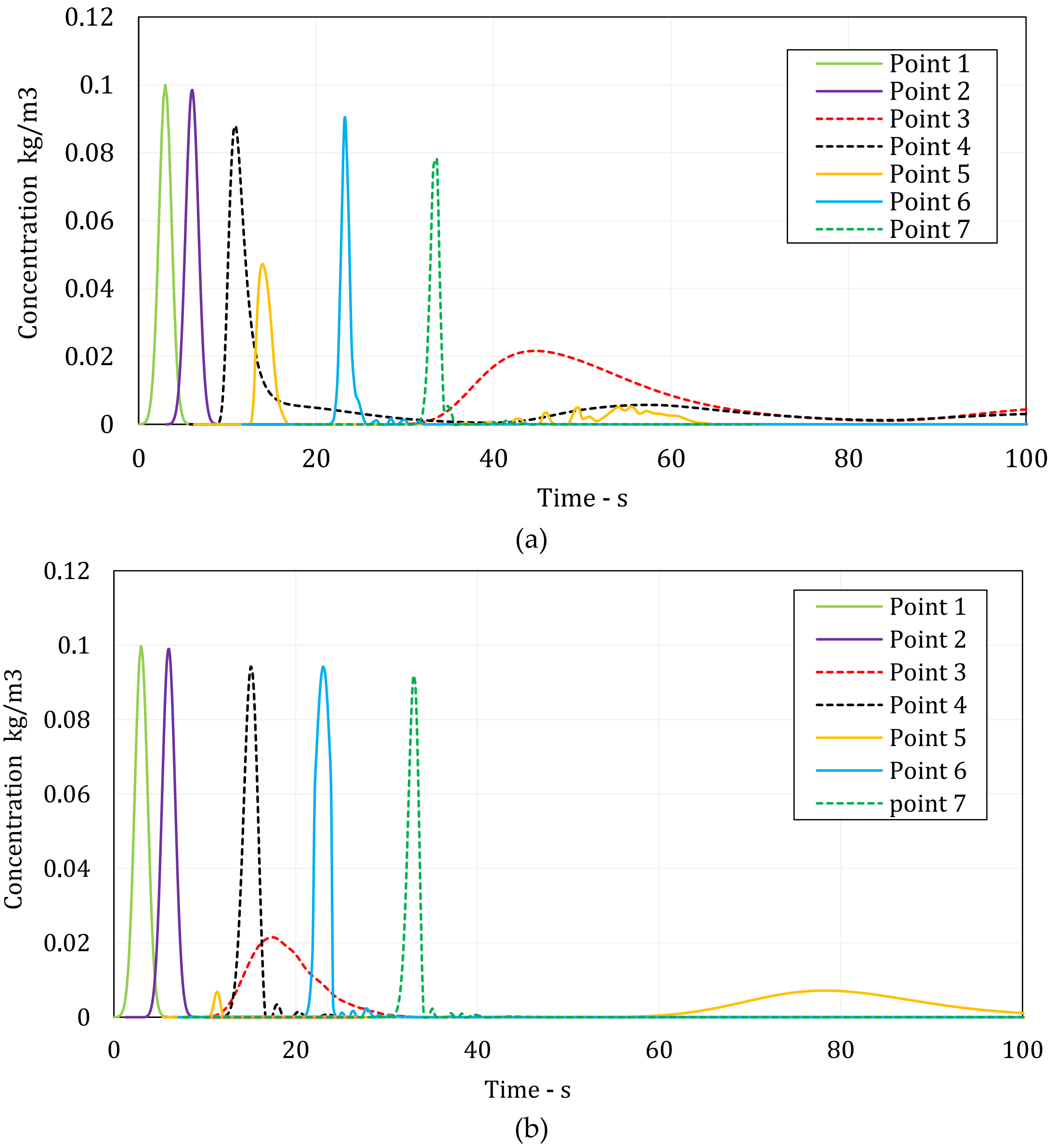

Figure 6.7. Concentration fields at different points over time (a) BFSF 1 (b) BFSF 2

Both in the BFSF 1 and the BFSF 2, at points 1 and 2 the concentration had a very high peak value. Their values in these points showed a pulse load of a tracer injected into the geometry. The lowest peak value of the BFSF 1 was at point 5, which was the secondary recirculation zone at the upper wall, while in the BFSF 2 the lowest value was in the third recirculation zone. The tracer moved both above and below the cylinder. The results show that there are some differences in concentration distributions at the same location as point 3, which is in the primary recirculation zone. For the BFSF 1, the tracer was trapped in the corner of the step and then released back into the main channel. However, in the BFSF 2, the tracer concentration was affected by the cylinder located downstream of the step. Comparatively, at point 7 some portion of the tracer concentration was trapped in the BFSF 1. Some parts of tracer in domain do not pass through the outlet, means that there is a distribution of the residence times in the system.

Tracer transport at inlet and outlet was measured over time. Figures 6.8 show the curves of injection and response concentration for the BFSF 1 and BFSF 2. The time scale was non-dimensional as $\theta=t/t_{HRT}$, where t_{HRT} is the theoretical mean residence time, defined as the ratio of the volume of the domain to the flow discharge.

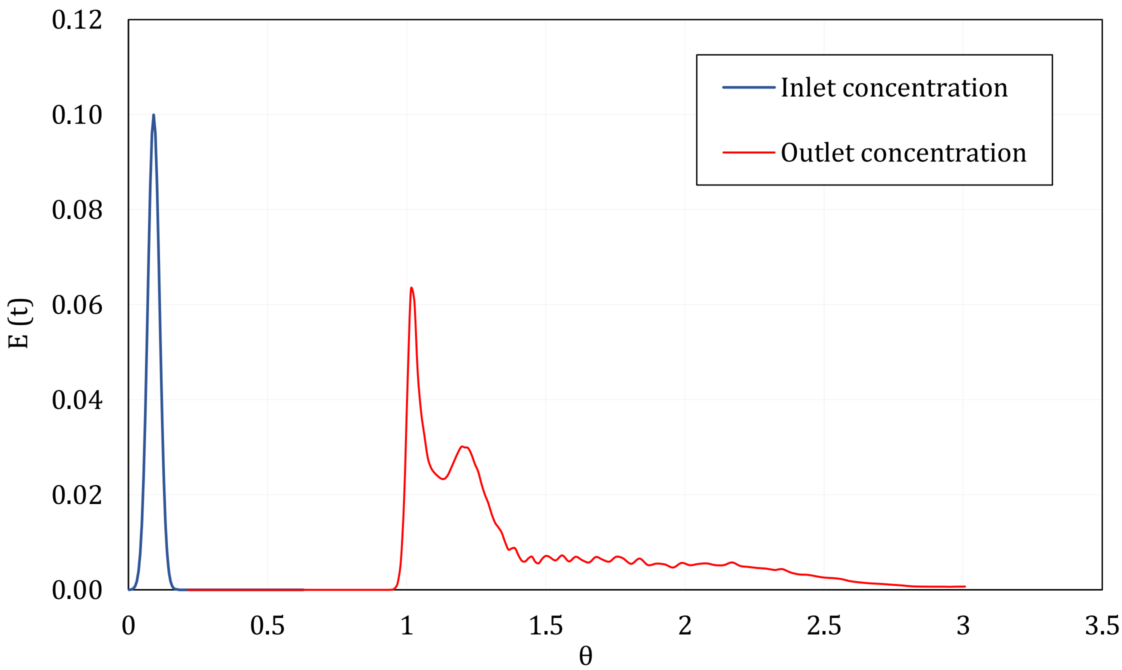

(a)

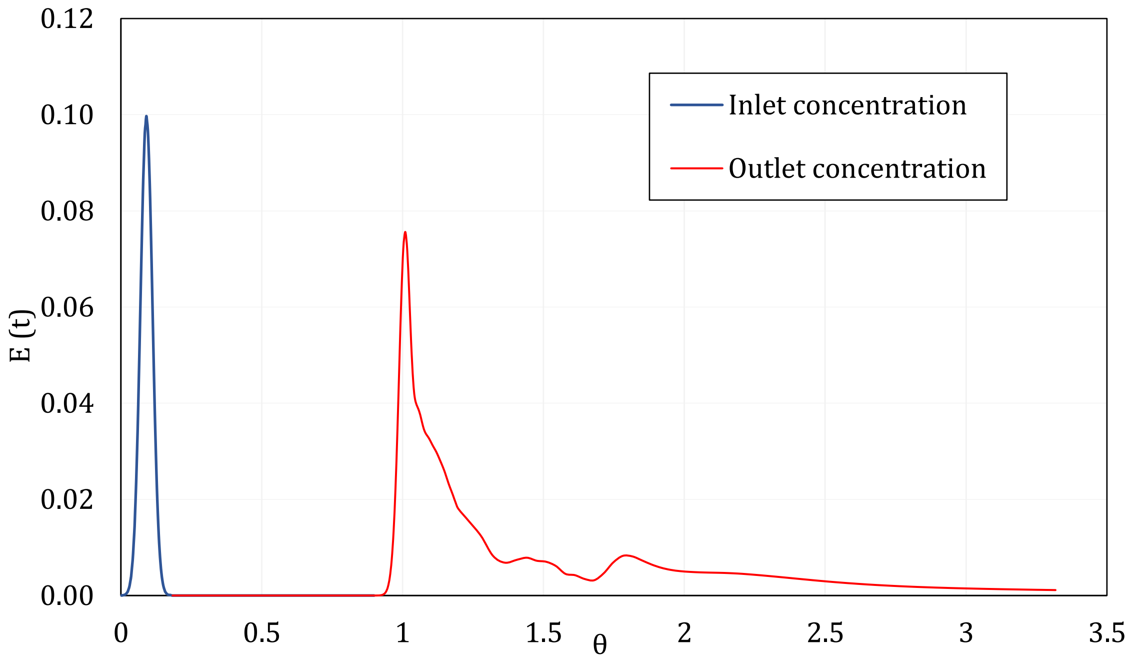

(b)

Figure 6.8. E(t) at the inlet and outlet vs. dimensionless time (θ) (a) BFSF 1 (b) BFSF 2

In both BFSF 1 and BFSF 2, the cloud of tracer had a range larger that the cloud at the input. Figure 6.9 shows the outlet normalized RTD and Figure 6.10 cumulative RTD, for BFSF 1 and BFSF 2.

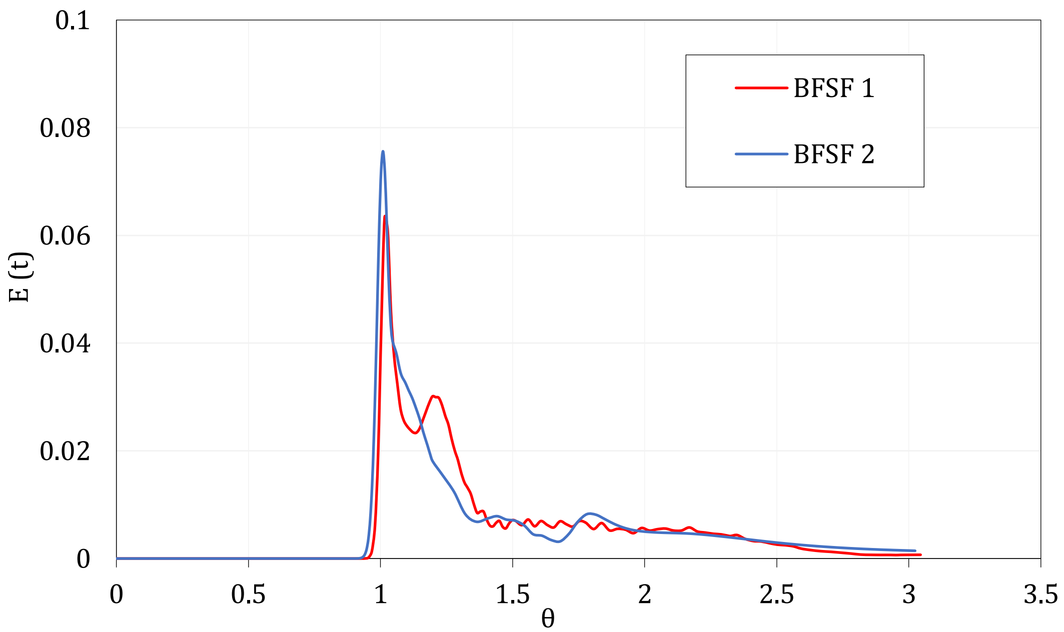

Figure 6.9. Normalized residence time distributions (RTD) at the outlet vs dimensionless time (θ) for the BFSF 1 and BFSF 2

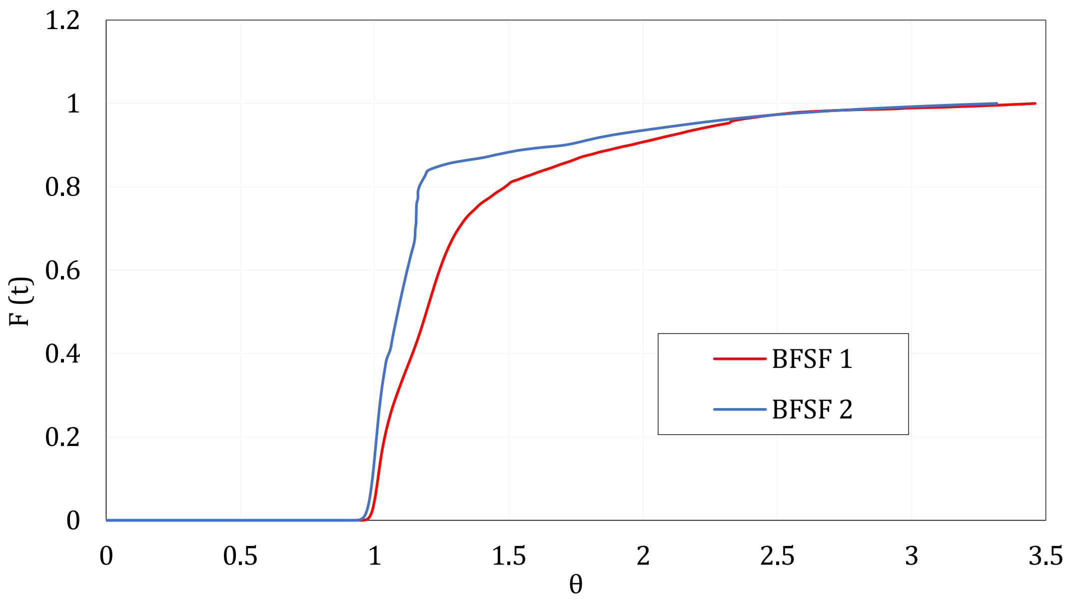

Figure 6.10. Cumulative residence time distributions (RTD) vs dimensionless time (θ) for the BFSF 1 the BFSF 2

The peak arrival time was also analyzed. It was found that in the BFSF 2, the concentration peak arrived before the peak for the BFSF 1. This means a shorter pass-through time for the BFSF 2. In addition, due to the small primary recirculation zone in the BFSF 2, no second peak was observed in this case compared to the BFSF 1. The second peak of the BFSF 1 was associated with the release of the tracer trapped in the primary recirculation zones. This trapped tracer left the geometry after the first peak. Also, for the BFSF 2, the peak of the normalized RTD plot increased in comparison to the BFSF 1.

6.3.3. Hydraulic performance indicators

The analysis of the concentration field in both BFSF 1 and BFSF 2 was carried out using the most common indicators used to evaluate the hydraulic efficiency, based on the residence time distribution (RTD) function. The mixing of a system can be described using different indicators derived from the RTD curve. The value of mixing indicators for BFSF 1 and BFSF 2 are listed in Table 6.1. Furthermore, the hydraulic efficiency indicators that were previously defined were computed for the BFSF 1 and BFSF 2.

Table 6. 1. Hydraulic efficiency indicators for the BFSF 1 and BFSF 2 (θ_{10} and θ_{90} denote the time that 10% and 90% of the injected tracer has reached the outlet. M_{90-10} is time elapsed between t_{10} and t_{90} and M_{75-25} is time elapsed between t_{25} and t_{75}. θ_f is time that the tracer is first observed at the outlet and MI is Morill index)

Indicators	BFSF 1	BFSF 2
θ_{10}	1.00	0.99
θ_{90}	1.95	1.719
θ_f	0.906	0.894
S_{50}	1.19	1.09
M_{90-10}	0.94	0.72
M_{75-25}	0.344	0.144
MI	1.95	1.729

The most common phenomenon, flow short-circuiting, was observed when a significant amount of flow exited the system at a faster rate than the nominal residence time, typically through high-velocity flow to the outlet. For the BFSF 2, a sharp peak of an RTD curve revealed flow short-circuiting. The short-circuiting indicators, such as θ_{10} and θ_{90}, were used for the tracer exiting at the outlet to determine the level of short-circuiting. The values of θ_{10} and θ_{90} show the time in which 10 % and 90% of the injected tracer reached the outlet. In the BFSF 2, the values of θ_{10} were smaller than that of the BFSF 1. A low θ_{10} value is normally associated with a short circuit between the inlet and the outlet. In BFSF 1, the value of θ_{90} was higher than that of BFSF 2 ($\theta_{90\text{-}BFSF1} > \theta_{90\text{-}BFSF2}$), meaning that large stagnant zones were found in the BFSF 1 .

For the BFSF 2, the value of θ_f (θ_f=0.894) was smaller than in the BFSF 1(θ_f=0.906) which means the first tracer was observed at the outlet earlier than in BFSF 1. In BFSF 2 the velocity was larger than for the BFSF 1 as the cylinder reduced the cross-section, but the difference was small.

As previously outlined, the indicator M_{90-10} is the time elapsed between t_{10} and t_{90}. Nuruzzaman et al. (2021), reported that M_{90-10} and M_{75-25} greater than 0 (M_{90-10} and $M_{75-25} > 0$) show mixing in the system. The comparison of results of M90-10 and M_{75-25} between the BFSF 1 and BFSF 2 indicated that some portions of the tracer were trapped in BFSF 1, consequently, the value of these indicators increased for the BFSF 1.

Morrill Index (MI) reflects the relative spread of the RTD curve between the θ_{10} and θ_{90}. It can also be interpreted as indicating the level of mixing. Teixeira and do Nascimento Siqueira (2008) recommended using the Morrill Index (MI) when the mixing level is low. As can be seen in Table 6.1, the value of MI index in both cases (BFSF 1 and BFSF 2) was greater than one, which showed mixing in the cases.

6.4. Discussion

The numerical study of solute transport downstream of BFSF geometry revealed several key findings that provide insights into the fundamental transport phenomena in step channels with cylindric obstacles. The key findings from this chapter are:

✓ The concentration further from the walls in the BFSF 1 and BFSF 2 downstream of the reattachment point was transported at a faster rate compared to the solute particles located closer to the walls.

✓ For the BFSF 1, the tracer was carried downstream due to downwardly directed flow downstream of the step. The tracer was trapped in the primary recirculation zone and some portion of it moved back upstream along the wall towards the step.

✓ For the BFSF 2, the tracer was affected by the cylinder located downstream of the step and trapped in the primary and third recirculation zones. The primary recirculation zone was smaller than that of the BFSF 1, resulting in a small amount of the tracer being trapped in the primary recirculation zone. The transport of the tracer across the dividing streamline was the result of two effects: diffusion across a streamline and an unsteady separation streamline.

✓ The analyzing of peak arrival time showed that the concentration peak arrived before the peak for BFSF 1 in BFSF 2. This indicates a shorter pass-through time for BFSF 2. There was a distribution of residence times in the system, and some parts of the tracer did not pass through the outlet.

✓ The hydraulic performance indicators, based on the RTD curves, showed that BFSF 2 had better hydraulic efficiency than BFSF 1, with a shorter residence time for the injected tracer, a higher degree of short-circuiting, and an earlier observation time for the tracer at the outlet. However, both BFSF 1 and BFSF 2 exhibited sufficient mixing behavior, with the MI index values greater than one, and M_{90-10} and M_{75-25} values greater than zero, indicating mixing in the systems.

Chapter 7 Analysis of results - Part 3: Habitat complexity metric

In this chapter, the effect of cylinder placement on the local variations of the habitat complexity metric is studied.

7.1. Introduction

Rivers can develop spatial varying flows, referred to as nonuniform flow, due to spatial variation in bedform elevation (Gualtieri et al. 2017). Most natural channels are characterized by relevant diversity of morphological due to changing riverbeds (Gualtieri 2008).

Recirculation zones and transverse flows downstream of step-like geometry typically play an important role in stream ecology as they can increase the residence time of organic matter and nutrients and enhance deposition processes. Defining habitat for fish, and other aquatic organisms may be evaluated through hydraulic characteristics such as flow depth, velocity gradients, vortices, circulation, and circulation (Crowder and Diplas 2002, Gualtieri et al. 2017). Velocity gradients along with other microhabitat and microhabitat parameters such as river depth and width are important across all scales and can influence physical habitat as well as biological activity, such as fish and other aquatic organisms spawning, feeding, and access to refugia. Fish are known to react to the velocity patterns in high flows by adjusting their behaviors in spawning, feeding, and access to refugia (Gualtieri et al. 2020). In ecological systems in streams, habitat is correlated with the substrate and the flow characteristics, which is related to the hydraulic complexity within a stream (Golpira et al. 2022, Gualtieri et al. 2020, Gualtieri et al. 2017). Many research studies have attempted to quantify the complexity and hydraulic habitat features in streams (Fischer et al. 2020, Kozarek et al. 2010, Shields and Rigby 2005); confluence (Gualtieri et al. 2020, Gualtieri et al. 2017) downstream of engineered log jam (L'Hommedieu et al. 2020); near boulder (Crowder and Diplas 2000a, Crowder and Diplas 2002, 2006, Golpira et al. 2022).

It is important for river management to quantitatively characterize the hydrodynamic interaction between the step and its surrounding environment because of localized velocity gradients that occur between the step and the main flow current, affecting aquatic habitat. As pointed out in Chapter 2, some cylindrical obstacles like wood may be trapped near or inside the expansions, further modifying the turbulent properties of the flow. Flow within step-like geometry is typically highly complex and the presence of cylindrical obstacles creates eddies, transverse flows, velocity gradients, and other spatial flow patterns. These obstacles in a stream may enhance the biotic diversity of macroinvertebrates as well as fish and may increase the availability of favorable habitats for spawning, foraging, and refuge (Golpira et al. 2022, Kozarek et al. 2010).

In this chapter, the results of cylinder placement at different horizontal locations on the local variations of velocity distributions and the habitat complexity metric downstream step considering the top wall as a free surface were analyzed.

7.2. Set-up of step flow simulations

To study the effect of cylinder placement at different horizontal locations on the local variations of the habitat complexity metrics two geometries were considered as step flow (SF 1) and step slow with cylinder (SF 2) with an expansion ratio ER=2. For the SF 2, a cylinder with different horizontal locations downstream of the step was considered. The sketch of the step with and without the cylinder and its configurations are presented in Figure 7.1 and Table 7.1. To reduce computational time for the tracer transport study, the domain downstream of step was reduced to L_d = 30 h for both cases SF 1 and SF 2. The boundary conditions were assigned at the inlet, the outlet, and the upper and bottom walls. The upper wall was considered symmetry. A fully developed flow was set at the inlet.

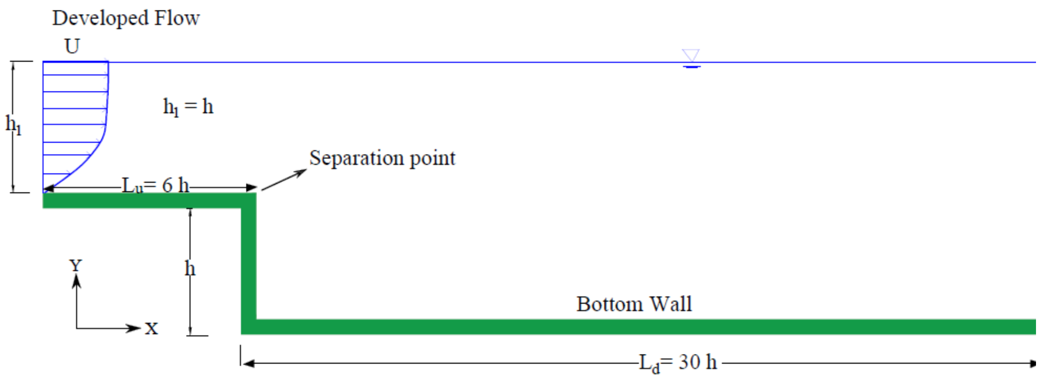

(a) SF 1

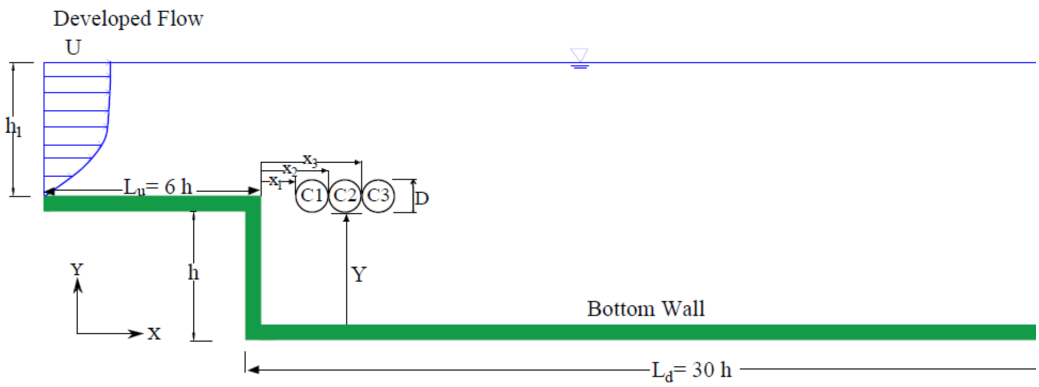

(b) SF 2

Figure 7.1. Sketch of the step simulations (not to scale) (a) Step without cylinder (b) Cylinder was set at a different distance from the step edge in the x-direction. H and h1 represent the step height and inlet-section height, respectively. Lu and L_d are length upstream of step and downstream of step. D is cylinder diameter and its location from step.

Table 7. 1. Step flow configurations of SF 1 and SF 2. x represents the distance of cylinder from step in x-direction and y represents the distance of cylinder from bottom wall in y-direction

Run	x	y	Remarks
SF 1	-	-	Step without cylinder
SF 2 – C1	X1=1 D	$h-\frac{D}{2}$	Step with cylinder
SF 2 – C2	X2=2 D	$h-\frac{D}{2}$	Step with cylinder
SF 2 – C3	X3=3 D	$h-\frac{D}{2}$	Step with cylinder

As previously pointed out in Chapter 4, the most accurate model for predicting flow characteristics of step flow was the standard k-ε model. So, for analyzing habitat complexity metric in stepped channel, the standard k-ε turbulence model was considered. The inlet Reynolds number was $Re_{h1}=Re_h$ = 9,000 for a geometry without and with that obstacle.

7.3. Calculation of the hydraulic complexity metric

Hydraulic complexity is defined as spatial variation in flow patterns, which may include eddies, transverse flows, and other flows causing velocity gradients. Velocity gradients in nonuniform flows are found in flow separation and recirculation zones which are associated with the flow complexity within the stream. They are likely impacting and utilized by fish and other aquatic organisms (Crowder and Diplas 2000a, Crowder and Diplas 2000b, 2002, Gualtieri et al. 2020). The M2 habitat hydraulic complexity metric was used to understand the flow complexity and influence of the cylinder on step flow. M2 indicates the average rate of change in kinetic energy per unit mass and unit length between two points, which is defined as (Crowder and Diplas 2000b):

$$M_2 = 2V_{avg} \frac{\left| V_2 - V_1 / \Delta s \right|}{V_{min}^2} \tag{7.1}$$

where V_2 and V_1 are velocity magnitudes measured a distance Δs apart and in the direction in which the spatial change in kinetic energy is being computed, V_{avg} is the average velocity magnitude between points 1 and 2 (mesh cells), and V_{min} is the minimum value of V_2 and V_1, and s indicates the direction of the line between points 1 and 2.

7.4. Results

7.4.1. Velocity distributions

To plan and evaluate habitat for aquatic organisms, it is crucial to anticipate the changes in flow velocity. Smith et al. (2014), hypothesized that fish select their habitat based on turbulence and velocity. Fish sense increased turbulence due to flow separation and use this to locate roughness elements such as wood for cover. Within the wake of wood, fish then select a region with a lower turbulence level, which can provide velocity shelters (Schalko et al. 2021). Figure 7.2 shows the velocity distributions of SF 1 and all Runs of SF 2 at Re_h=9,000.

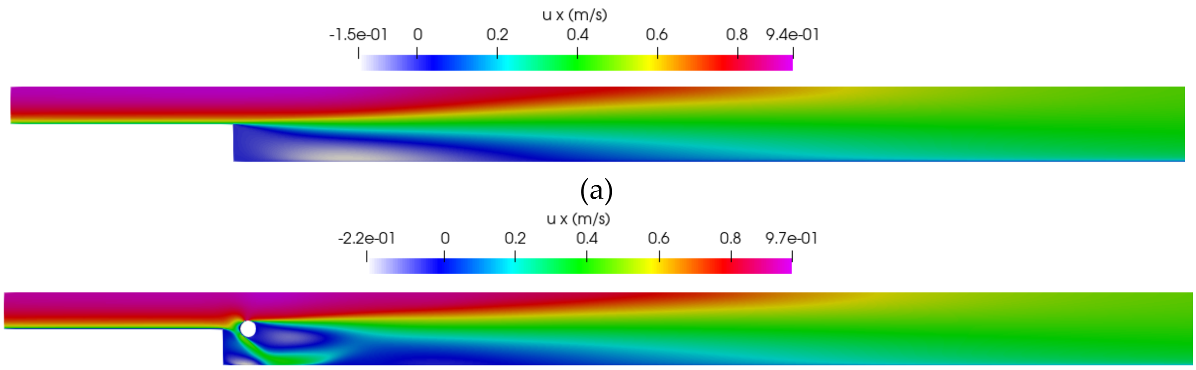

(b)

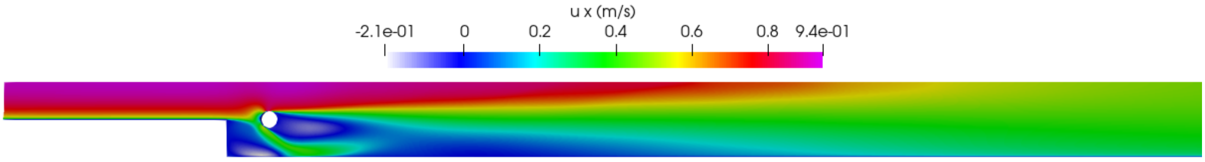

(c)

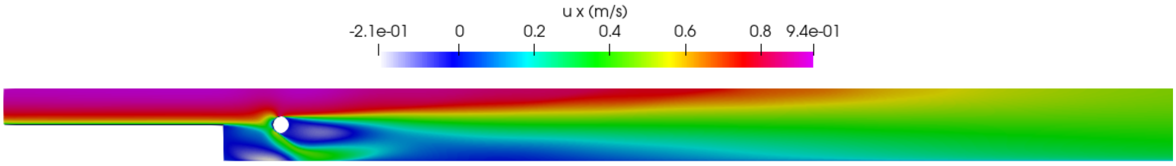

(d)

Figure 7.2. u-velocity distribution downstream of step at different locations of cylinder compared with that of SF 1. (a) SF 1 (b) SF 2 – C1 (c) SF 2 – C2 (d) SF 2 – C3

For all Runs SF 2, the maximum and minimum values of velocity values increased compared to SF 1 and gradually recovered to the values as SF 1 after the reattachment point. As a cylinder was placed at different locations downstream of the step, the values of velocity deceased behind it. The flow around a cylinder produced a wake with reduced velocity and transverse shear that may enhance turbulence production at the scale of the body.

A cylinder downstream of the step can establish both regions of reduced velocity, which provide shelter for resting, and regions of increased velocity near the bottom wall which provide higher drift densities for more efficient feeding and higher rates of energy gain.

7.4.2. **Hydraulic complexity metric (M2)**

Maps of hydraulic complexity M2 metric at the different horizontal locations of the cylinder downstream of the step were generated. In addition, a longitudinal profile of the hydraulic complexity (M2) was generated by taking the value of M2 between the step and the bottom wall (y/h=0.5) and along the step edge (y/h=1). Figures 7.3 – 7.6 depict the map of hydraulic complexity M2 for SF1 and all Runs of SF 2 in the region downstream of the step, and their values at y/h=0.5 and y/h=1.

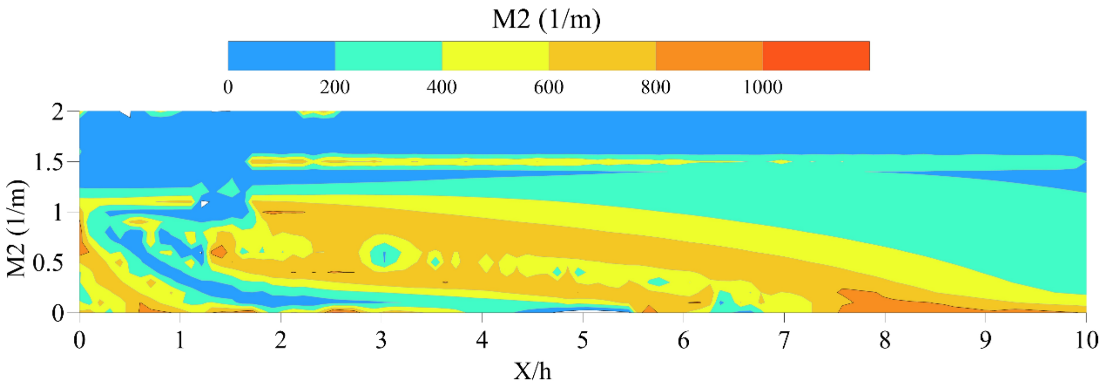

(a)

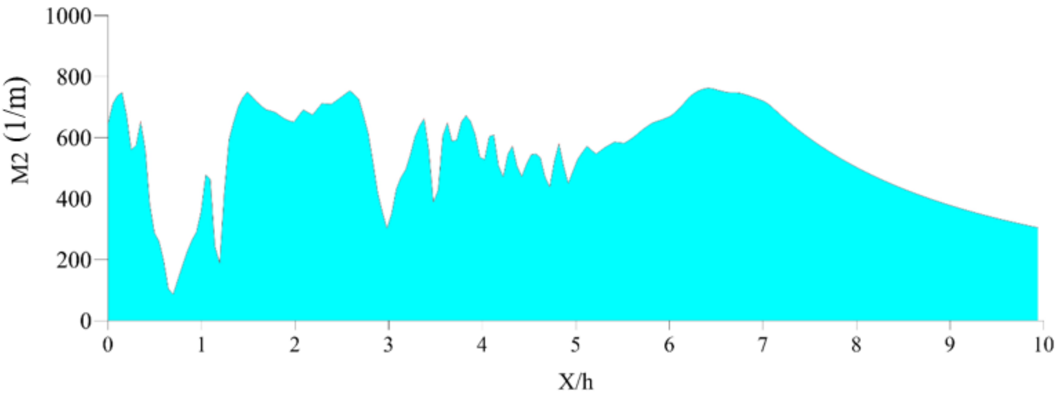

(b)

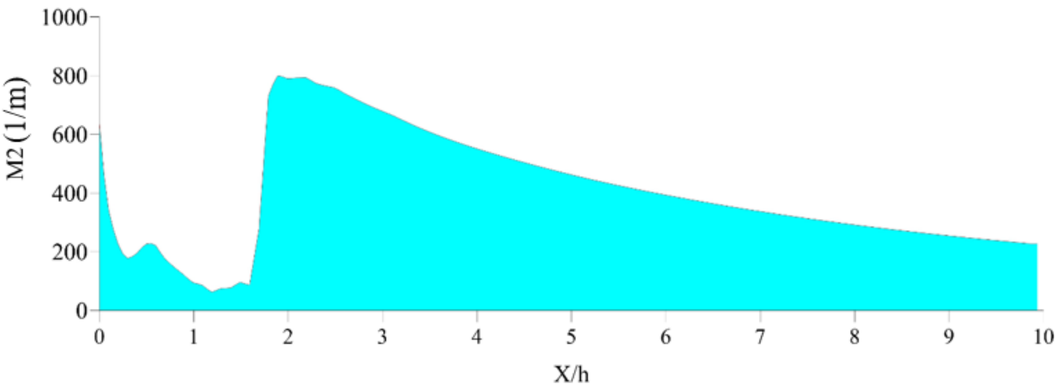

(c)

Figure 7.3. (a) Map of the metric M2 on SF 1; (b) Distribution of M2 vs the distance from the step at y/h=0.5; (c) Distribution of the metric vs the distance from the step at y/h = 1

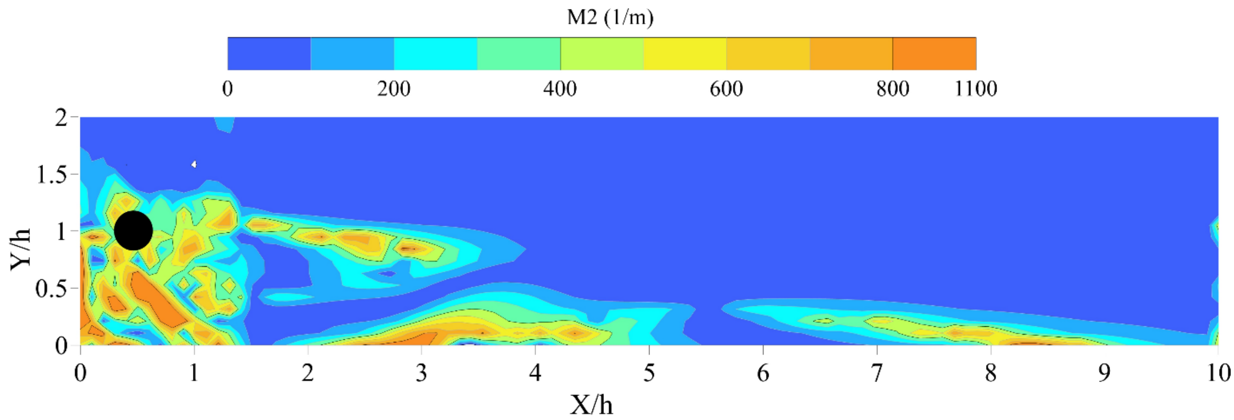

(a)

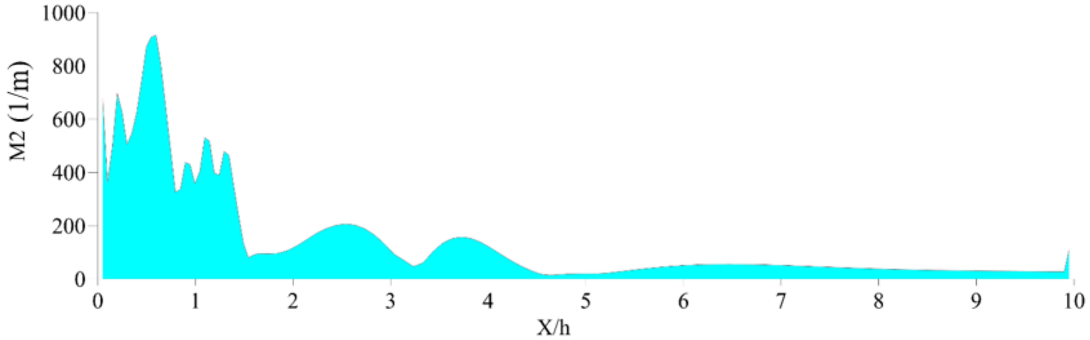

(b)

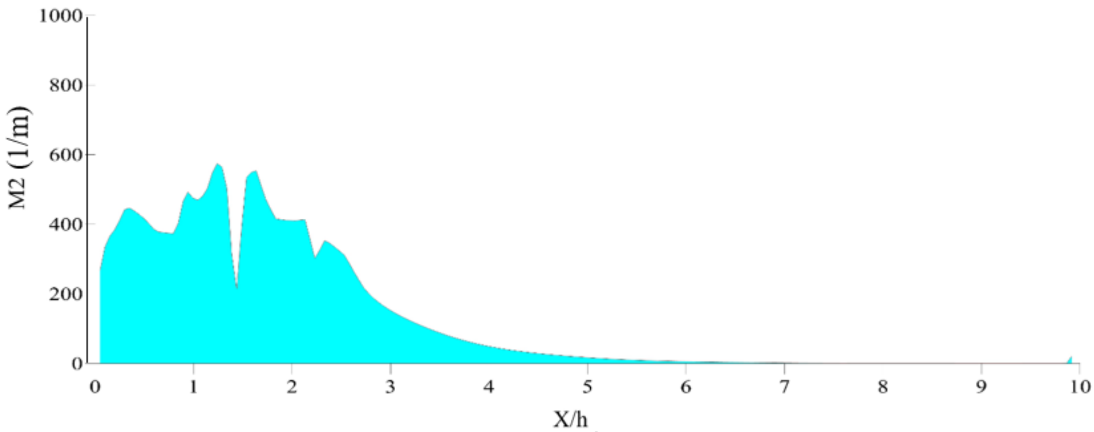

(c)

Figure 7.4. (a) Map of the metric M2 on SF 2 - C1; (b) Distribution of M2 vs the distance from the step at y/h=0.5; (c) Distribution of the metric vs the distance from the step at y/h = 1

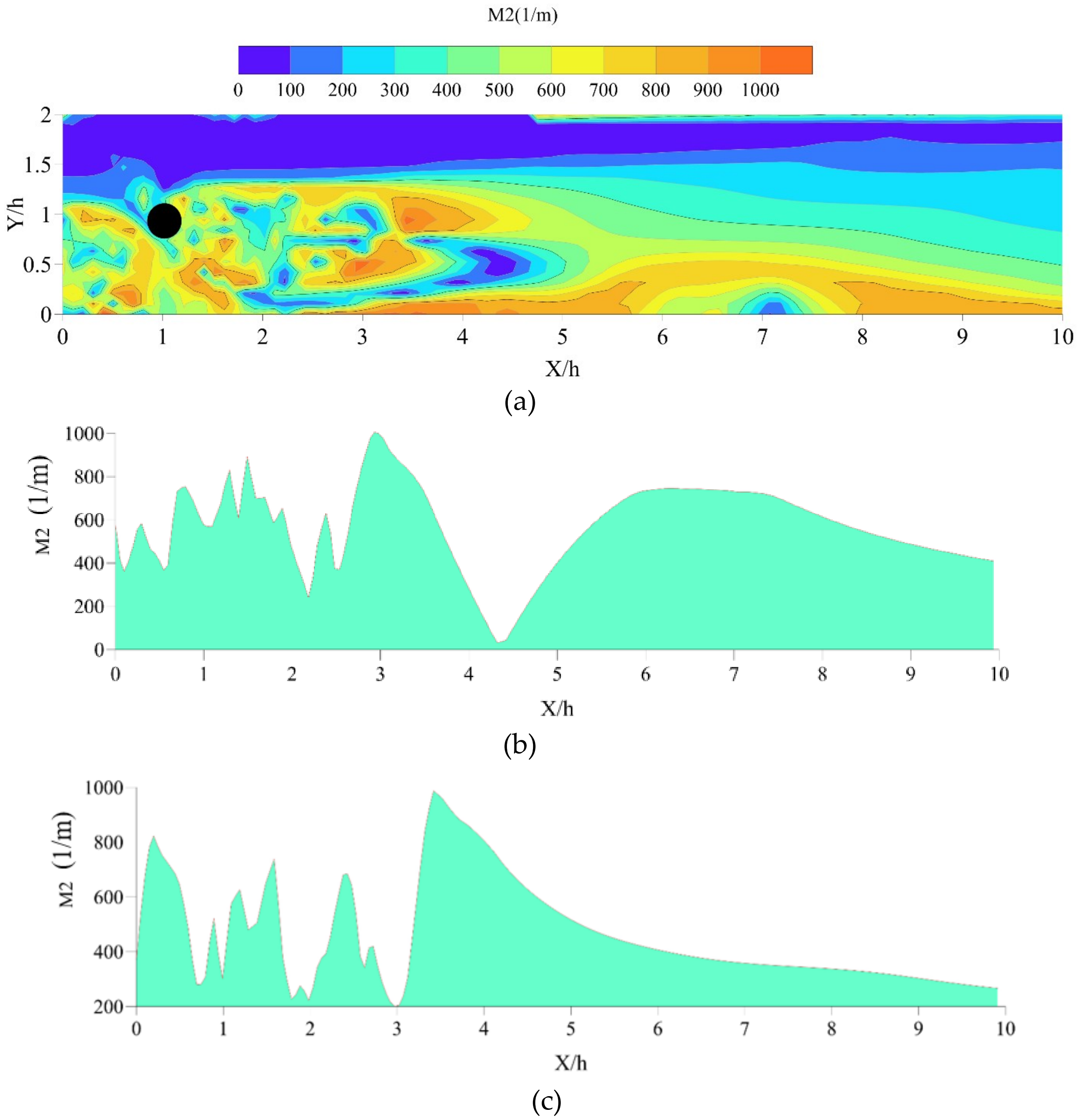

Figure 7.5. (a) Map of the metric M2 on SF 2 – C2; (b) Distribution of M2 vs the distance from the step at y/h=0.5; (c) Distribution of the metric vs the distance from the step at y/h = 1

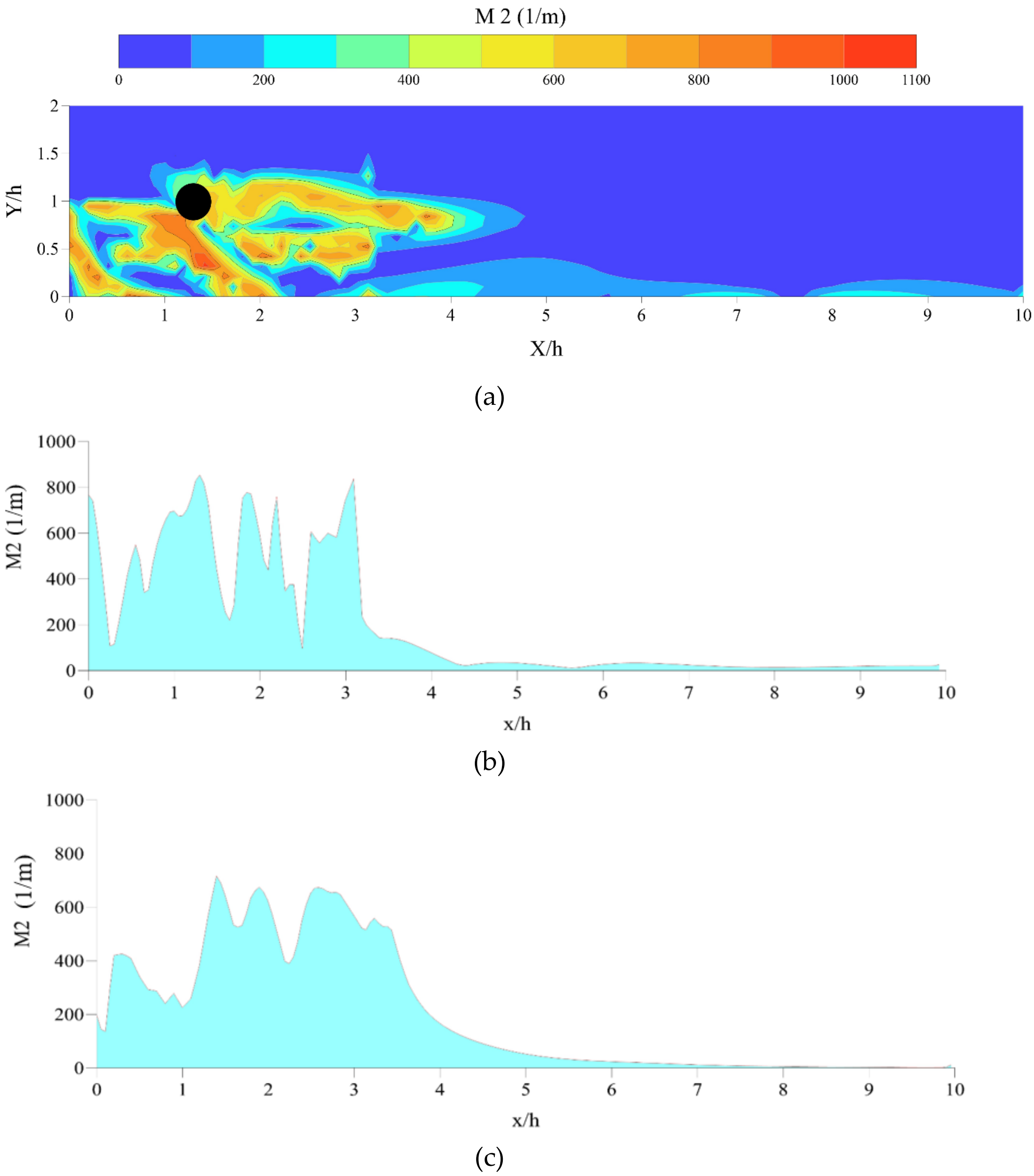

Figure 7.6. (a) Map of the metric M2 on SF 2 – C3; (b) Distribution of M2 vs the distance from the step at y/h=0.5; (c) Distribution of the metric vs the distance from the step at y/h = 1

Figure 7.2 shows the M2 distribution in SF1, where a high M2 region was observed in the vicinity of the reattachment point and the corner of the step. This high M2 region indicates a complex flow structure with significant energy gradients and recirculation zones. Figures 7.3, 7.4, and 7.5 show the M2 distribution in SF2, where a cylinder was placed downstream of the step at different locations. In all runs of SF2, high M2 regions were observed downstream of the cylinder, specifically in the wake of the cylinder. This indicates that adding a cylinder downstream of the step increased the hydraulic complexity metric.

The mean M2 was observed to increase due to the variation in the local flow caused by the presence of the cylinder. This suggests that the presence of obstacle in a flow field can significantly influence the flow structure and increase hydraulic complexity. Regions with significant energy gradients and recirculation can be used to specify suitable habitats, such as spawning and feeding grounds, for aquatic organisms.

The results of this study highlight the importance of understanding hydraulic complexity in environmental hydraulics. The distribution of M2 can provide valuable insights into the flow structure and the impact of obstacle on the flow downstream of step. This information can be used to design more effective and sustainable systems for managing nutrients in aquatic environments. Additionally, the study of hydraulic complexity can aid in the identification of suitable habitats for aquatic organisms and the development of habitat restoration strategies.

The distribution of hydraulic complexity metric M2 was studied in the context of flow over the step with and without a cylinder downstream of the step. The M2 distribution was analyzed for two sets of runs, SF1 and SF2, where SF1 had no cylinder, and SF2 had a cylinder placed at different locations downstream of the step. In conclusion, the distribution of hydraulic complexity metric M2 was analyzed in the context of flow downstream of step with and without a cylinder.

Chapter 8 Conclusions and Recommendations

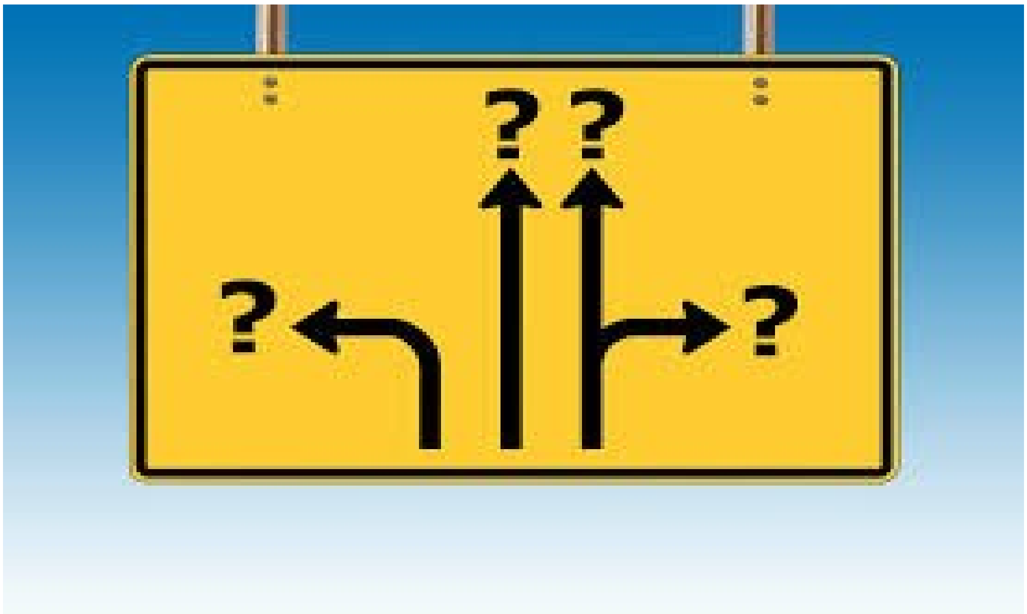

The main findings and conclusions and recommendations of this PhD project are included in this chapter.

8.1. Conclusion

In the present study, flow over a backward-facing step with a cylinder placed downstream of the step in both laminar and turbulent flow was investigated, First, the results of the numerical study were validated by available literature data. The numerical results were found to be in good agreement with the literature's experimental and numerical results.

In the laminar flow, different Reynolds numbers were considered to study the effect of the cylinder on flow over a backward-facing step. Moreover, the concentration transport due to the pulse load of it in laminar flow downstream of the step was investigated.

In turbulent flow, the simulated reattachment lengths, velocity profiles, skin friction coefficients, and pressure coefficient from several RANS models, standard k-ε, RNG k-ε, standard k-ω, SST k-ω, were compared with the available literature data. Considering the accuracy and the calculation time of the models, only the standard k-ε model was used for the study of the effect of a cylinder placed downstream of the step to investigate how the cylinder modifies the classical BFS flow two-dimensional BFSF structure. In addition, in turbulent flow, the effect of cylinder placement on the local variations of the habitat complexity metrics was studied.

Flow downstream of the backward-facing step is complex and the cylinder creates eddies, transverse flows, velocity gradients, and other spatial flow patterns. A better understanding of how the cylinder interacts to create spatially varying flows downstream of the step leads to the quantification of its features. The results of the study provided the following answers to the research questions:

(1) What are the effects of the cylinder on the step in the laminar flow?

In laminar flow, cylinder placement downstream of a backward facing step affects flow structures, such as reattachment and recirculation zones, velocity profile, and skin friction coefficient. In BFSF 1, three recirculation zones were observed: a primary recirculation zone on the bottom wall, a second recirculation zone at the upper wall for Reh > 300, and a third recirculation zone on the bottom wall in the early part of the transitional regime. The cylinder pushed the primary recirculation region upstream to the corner of the step, decreasing its length, while the second recirculation zone near the upper wall was missing for BFSF 2. In BFSF 2, the third recirculation zone was observed when a cylinder was positioned at a diameter distance from the step edge, and its location was upstream of BFSF 1. The cylinder increased the velocity due to a narrow cross-section downstream of the cylinder, and the location of the maximum velocity shifted towards the middle of the channel.

In BFSF 1, a minimum value of skin friction coefficient at the bottom wall occurred due to the recirculating flow. The cylinder downstream of the step produced significantly higher minimum and maximum values of the skin friction coefficient at the bottom wall than those without the cylinder. In BFSF 2, two minimum values of skin friction coefficient were observed due to the two recirculation zones for Reh > 75.

(2) What are the effects of the step on the dynamics of the vortex generation of a cylinder?

In laminar flow, the presence of the step altered the flow structure past the cylinder, resulting in an asymmetric wake distribution with a large portion of the vortices shifting towards the below cylinder. In turbulent flow, the cylinder positioned along or above the step edge suppressed the formation of the von Kármán vortex street, generating two vortices of different sizes behind the cylinder, which were located towards the bottom wall. When the cylinder was located below the step, its behavior was similar to that observed in BFSF 1. In the case of a cylinder placed downstream of the step, it may become submerged during higher discharges, and the flow passing over the cylinder could suppress the formation of the von Kármán vortex street, as observed in this study. The wake generated by the cylinder can provide a longer downstream region for the deposition of organic matter, which is beneficial for aquatic organisms.

(3) Which turbulence models should be used to estimate the field flow downstream of the step in the recirculation zone?

In turbulent flow, the simulated reattachment lengths, velocity profiles, skin friction coefficients, and pressure coefficient from several RANS models, standard k-ε, RNG k-ε, standard k-ω, SST k-ω, were compared with the available literature data. The most accurate model for predicting reattachment lengths, skin friction coefficient, and pressure coefficients was the standard k-ε model with an average error lower than 6, 17.5, and 20.5%, respectively.

(4) What is the effect of the cylinder at different horizontal and vertical locations downstream of the step in turbulent flow?

In the turbulent flow of the BFSF 1, primary recirculation zone was observed on the bottom wal. For the BFSF 2, the cylinder pushed the primary recirculation region upstream to the corner of the step and its length decreased and the third recirculation zone was observed at bottom wall when a cylinder was positioned at a diameter distance from the step edge and its location was upstream than in the BFSF 1. As the cylinder was placed far away from the step and above or below the step mid-plane, the third recirculation zone was missing. As a result, the cylinder placed downstream of the step produced a third small recirculation zone and it can increase the residence time of deposition of nutrients for aquatic organisms, showing the environmental function of the recirculation zone.

As laminar flow, the location of the maximum velocity shifted towards the middle of the channel in both laminar and turbulent flow. Flow velocity influences the kinds of organisms that can live in the stream; some organisms prefer fast-flowing zones; other one need quiet areas. High-velocity streams generally have higher levels of dissolved oxygen than slow streams because they are better aerated.

The cylinder affected the distribution of pressure along the bottom wall. In the BFSF 2, the minimum and maximum values of the pressure coefficients were lower than those in the BFSF 1. However, the average value of pressure coefficients downstream of the reattachment point was smaller than that in the BFSF 2. In addition, the step affected the distribution of the surface pressure of the cylinder by moving the largest pressure region to the top of the cylinder.

The results of turbulent kinetic energy showed the maximum turbulent kinetic energy in BFSF 1 and BFSF 2-T5 was below the mid-plane of the step in the regions of high shear flow, while for other BFSF 2 runs, the maximum turbulent kinetic energy was shifted above the mid-plane of the step. Downstream of the cylinder, TKE was amplified in the midplane, and the region of high TKE was bounded by the cylinder, with two subregions of high TKE found when the cylinder was above the mid-plane of step. Turbulence influences feeding behavior, swimming ability, and habitat selection of the aquatic organisms. Some species select their habitat with lower turbulence levels, which can provide velocity shelters, while other one seeks areas of increased turbulence to reduce locomotory costs.

(5) What is the effect of a cylinder on the concentration field due to its pulse load in recirculation zones downstream of the step?

The study revealed key findings on the fundamental transport phenomena in step channels with obstacles. Further from the walls in the BFSF 1 and BFSF 2 downstream of the reattachment point was transported more rapidly than particles located closer to the walls. For the BFSF 1, the tracer was carried downstream by the downwardly directed flow downstream of the step and trapped in the primary recirculation zone, and some portion of it moved back upstream along the wall towards the step. In BFSF 2, the tracer was affected by the cylinder located downstream of the step and trapped in the primary and third recirculation zones, with the transport of the tracer across the dividing streamline being the result of two effects: diffusion across a streamline and an unsteady separation streamline. The analysis of peak arrival time showed that

BFSF 2 had a shorter pass-through time compared to BFSF 1. Both BFSF 1 and BFSF 2 exhibited sufficient mixing behavior, with the MI index values greater than one and M_{90-10} and M_{75-25} values greater than zero, indicating mixing in the systems. The hydraulic performance indicators, based on the RTD curves, showed that BFSF 2 had better hydraulic efficiency than BFSF 1, with a shorter residence time for the injected tracer, a higher degree of short-circuiting, and an earlier observation time for the tracer at the outlet.

(6) What is the effect of cylinder placement on the local variations of the habitat complexity metrics?

The study examined the distribution of hydraulic complexity metric M2 in the context of flow over the step, with and without a cylinder downstream of the step. The results showed that the presence of a cylinder downstream of the step increased the hydraulic complexity metric, as evidenced by the observed high M2 regions downstream of the cylinder. M2 represents the energy gradients that affect organism's motion and could be used to identify biogeographical boundaries in aquatic ecosystems. In the present study, in the step with a cylinder, the areas with the highest M2 values were located mostly far away from the step. The region downstream of the step with a cylinder can be used to identify areas with biological richness as well as ideal feeding habitats. The study highlights the importance of understanding hydraulic complexity and that recirculation zone can provide suitable habitats for aquatic organisms. The information obtained from analyzing the M2 distribution can be used in the identification of suitable habitats for aquatic organisms and the development of habitat restoration strategies.

8.2. Recommendations

As in this study, the geometry was a backward-facing step flow, follow-on studies are needed to analyze the effect of cylindric obstacles on flow and turbulence characteristics in the step channel. To further advance the understanding of the effects of cylindrical obstacles on flow and turbulence characteristics in the step channel, future studies should focus on analyzing the impact of different cylinder arrangements, sizes, and shapes.

In addition to the two-dimensional flow field analysis conducted in this study, it is also crucial to study the three-dimensional flow and turbulence patterns in the entire wake of different configurations. These studies can provide a more comprehensive understanding of the complex flow structures and turbulence characteristics in the wake of obstacles and can inform the development of physics-based guidelines for the design and installation of instream structures in streams.

Moreover, as natural channels have a diverse range of morphological conditions, it is crucial to quantitatively characterize the hydrodynamic interaction between the step and its surrounding environment to inform river management decisions. Spatial habitat and bioenergetics metrics can be used to assess the impact of cylinder placement on local variations in habitat complexity metrics, providing valuable insights for the design of instream structures. Advanced computational methods such as Detached Eddy Simulation (DES), a hybrid RANS-LES model, can be applied to obtain flow quantities highly resolved in space and time. This can provide a more accurate understanding of the complex flow structures and turbulence characteristics around instream structures, helping to inform design decisions. These studies can help identify the optimal cylinder configuration that can minimize the the negative impacts on the surrounding aquatic ecosystem.

Further research linking instream species and desirable habitat complexity is needed to develop effective management strategies for maintaining a healthy aquatic ecosystem.

Bibliography

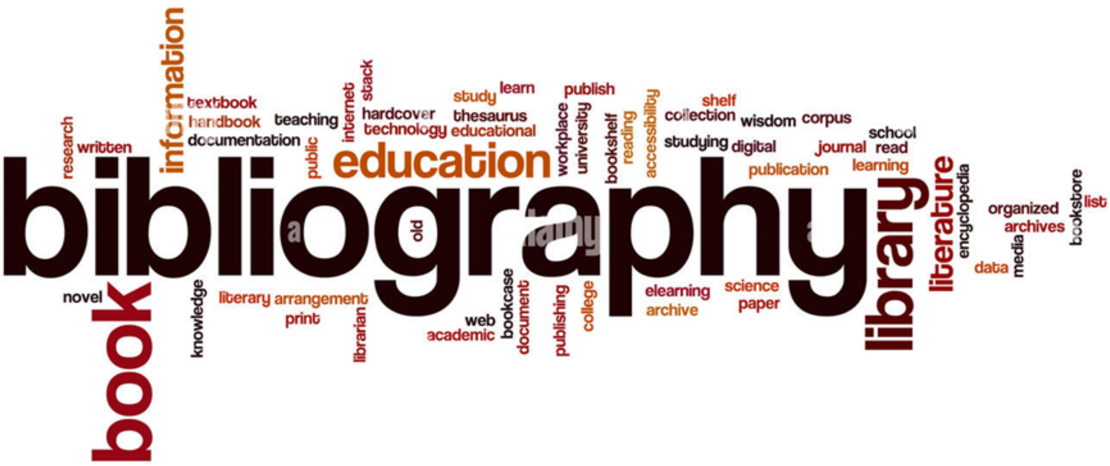

Abbott, D. and Kline, S. (1962) Experimental investigation of subsonic turbulent flow over single and double backward facing steps.

Adams, E. and Johnston, J. (1988a) Effects of the separating shear layer on the reattachment flow structure Part 1: Pressure and turbulence quantities. Experiments in Fluids 6(6), 400-408.

Adams, E. and Johnston, J. (1988b) Effects of the separating shear layer on the reattachment flow structure part 2: Reattachment length and wall shear stress. Experiments in Fluids 6(7), 493-499.

Ahmad, M., Ghani, U., Anjum, N., Pasha, G.A., Ullah, M.K. and Ahmed, A. (2020) Investigating the Flow Hydrodynamics in a Compound Channel with Layered Vegetated Floodplains. Civil Engineering Journal 6(5), 860-876.

Al-Asadi, K. and Duan, J.G. (2017) Assessing methods for estimating roughness coefficient in a vegetated marsh area using Delft3D. Journal of Hydroinformatics 19(5), 766-783.

Al-Aswadi, A., Mohammed, H., Shuaib, N. and Campo, A. (2010) Laminar forced convection flow over a backward facing step using nanofluids. International Communications in Heat and Mass Transfer 37(8), 950-957.

Al-Jelawy, H., Kaczmarczyk, S., AlKhafaji, D., Mirhadizadeh, S., Lewis, R. and Cross, M. (2016) A computational investigation of a turbulent flow over a backward facing step with OpenFOAM, pp. 301-307, IEEE.

Ameur, H. and Menni, Y. (2019) Non-Newtonian fluid flows through backward-facing steps. SN Applied sciences 1(12), 1-8.

Anderson Jr, John D. (2011) "Aerodynamics: Some Fundamental Principles and equations." Fundamentals of aerodynamics 3: 1-417.

Anguraj, A. and Palraj, J. (2018) Numerical study of fluid flow and heat transfer in a backward facing step with a rotating cylinder. Malaya Journal of Matematik (MJM) 6(2, 2018), 435-442.

Anjum, N., Ghani, U., Ahmed Pasha, G., Latif, A., Sultan, T. and Ali, S. (2018) To investigate the flow structure of discontinuous vegetation patches of two vertically different layers in an open channel. Water 10(1), 75.

Anjum, N. and Tanaka, N. (2020a) Hydrodynamics of longitudinally discontinuous, vertically double layered and partially covered rigid vegetation patches in open channel flow. River Research and Applications 36(1), 115-127.

Anjum, N. and Tanaka, N. (2020b) Investigating the turbulent flow behaviour through partially distributed discontinuous rigid vegetation in an open channel. River Research and Applications.

Anwar-ul-Haque, F.A., Yamada, S. and Chaudhry, S.R. (2007) Assessment of turbulence models for turbulent flow over backward facing step, pp. 2-7.

Araujo, P.P. and Rezende, A.L.T. (2017) Comparison of turbulence models in the flow over a backward-facing step. International Journal of Engineering Research & Science 3(11), 88-93.

Armaly, B.F., Durst, F., Pereira, J. and Schönung, B. (1983) Experimental and theoretical investigation of backward-facing step flow. Journal of fluid mechanics 127, 473-496.

Barri, M., El Khoury, G.K., Andersson, H.I. and Pettersen, B. (2010) DNS of backward-facing step flow with fully turbulent inflow. International Journal for Numerical Methods in Fluids 64(7), 777-792.

Barsukov, A.V., Terekhov, V.V. and Terekhov, V.I. (2021) Effect of a passive disturbance on the flow structure and heat transfer in the separation region behind a backward-facing step. High Temperature 59(1), 115-120.

Bayani-Cardenas, M., 2009. A model for lateral hyporheic flow based on valley slope and channel sinuosity. Water Resour. Res. 45. W01501.

Bishop, R.E.D. and Hassan, A. (1964) The lift and drag forces on a circular cylinder in a flowing fluid. Proceedings of the Royal Society of London. Series A. Mathematical and Physical Sciences 277(1368), 32-50.

Biswas, G., Breuer, M. and Durst, F. (2004) Backward-facing step flows for various expansion ratios at low and moderate Reynolds numbers. J. Fluids Eng. 126(3), 362-374.

Biswas, R. and Strawn, R.C. (1998) Tetrahedral and hexahedral mesh adaptation for CFD problems. Applied Numerical Mathematics 26(1-2), 135-151.

Blocken, B. and Gualtieri, C. (2012) Ten iterative steps for model development and evaluation applied to Computational Fluid Dynamics for Environmental Fluid Mechanics. Environmental Modelling & Software 33, 1-22.

Bosnyakov, S., Duben, A., Zheltovodov, A., Kozubskaya, T., Matyash, S. and Mikhailov, S. (2020) Numerical simulation of supersonic separated flow over inclined backward-facing step using RANS and LES methods. Mathematical Models and Computer Simulations 12(4), 453-463.

Bouda, N.N., Schiestel, R., Amielh, M., Rey, C. and Benabid, T. (2008) Experimental approach and numerical prediction of a turbulent wall jet over a backward facing step. International journal of heat and fluid flow 29(4), 927-944.

Brika, D. and Laneville, A. (1999) The flow interaction between a stationary cylinder and a downstream flexible cylinder. Journal of Fluids and Structures 13(5), 579-606.

Canuto, D. and Taira, K. (2015) Two-dimensional compressible viscous flow around a circular cylinder. Journal of fluid mechanics 785, 349-371.

Carlston, J.S. (2015) Impact of geometric design of hydraulic contact tanks on residence time distributions, Colorado State University.

Caroppi, G., Gualtieri, P., Fontana, N. and Giugni, M. (2018) Vegetated channel flows: Turbulence anisotropy at flow–rigid canopy interface. Geosciences 8(7), 259.

Caroppi, G., Västilä, K., Gualtieri, P., Järvelä, J., Giugni, M. and Rowiński, P.M. (2021) Comparison of flexible and rigid vegetation induced shear layers in partly vegetated channels. Water Resources Research 57(3), e2020WR028243.

Catalano, P., Wang, M., Iaccarino, G. and Moin, P. (2003) Numerical simulation of the flow around a circular cylinder at high Reynolds numbers. International journal of heat and fluid flow 24(4), 463-469.

Chandrsuda, C. and Bradshaw, P. (1981) Turbulence structure of a reattaching mixing layer. Journal of fluid mechanics 110, 171-194.

Chang, K., Constantinescu, G. and Park, S.-O. (2007) Assessment of predictive capabilities of detached eddy simulation to simulate flow and mass transport past open cavities.

Chen, C.-K., Yen, T.-S. and Yang, Y.-T. (2006a) Lattice Boltzmann method simulation of a cylinder in the backward-facing step flow with the field synergy principle. International journal of thermal sciences 45(10), 982-989.

Chen, H. and Zou, Q.-P. (2019) Eulerian–Lagrangian flow-vegetation interaction model using immersed boundary method and OpenFOAM. Advances in water resources 126, 176-192.

Chen, L., Asai, K., Nonomura, T., Xi, G. and Liu, T. (2018) A review of Backward-Facing Step (BFS) flow mechanisms, heat transfer and control. Thermal Science and Engineering Progress 6, 194-216.

Chen, Y., Nie, J., Hsieh, H.-T. and Sun, L. (2006b) Three-dimensional convection flow adjacent to inclined backward-facing step. International journal of heat and mass transfer 49(25-26), 4795-4803.

Cheng, W., Sun, Z. and Liang, S. (2019) Numerical simulation of flow through suspended and submerged canopy. Advances in water resources 127, 109-119.

Cherdron, W., Durst, F. and Whitelaw, J.H. (1978) Asymmetric flows and instabilities in symmetric ducts with sudden expansions. Journal of fluid mechanics 84(1), 13-31.

Choi, H.H. and Nguyen, J. (2016) Numerical investigation of backward facing step flow over various step angles. Procedia Engineering 154, 420-425.

Choi, S.-U. and Kang, H. (2006) Numerical investigations of mean flow and turbulence structures of partly-vegetated open-channel flows using the Reynolds stress model. Journal of Hydraulic Research 44(2), 203-217.

Clancy. L. J., Aerodynamics (1975) Pitman Publishing Limited, London. ISBN 0-273-01120-0

Crowder, D. and Diplas, P. (2000a) Using two-dimensional hydrodynamic models at scales of ecological importance. Journal of hydrology 230(3-4), 172-191.

Crowder, D.W. and Diplas, P. (2000b) Evaluating spatially explicit metrics of stream energy gradients using hydrodynamic model simulations. Canadian Journal of Fisheries and Aquatic Sciences 57(7), 1497-1507.

Crowder, D.W. and Diplas, P. (2002) Vorticity and circulation: spatial metrics for evaluating flow complexity in stream habitats. Canadian Journal of Fisheries and Aquatic Sciences 59(4), 633-645.

Crowder, D.W. and Diplas, P. (2006) Applying spatial hydraulic principles to quantify stream habitat. River Research and Applications 22(1), 79-89.

Cruz, D.O.d.A., Batista, F. and Bortolus, M. (2000) A law of the wall formulation for recirculating flows. Journal of the Brazilian Society of Mechanical Sciences 22, 43-51.

Cui, J. and Neary, V.S. (2008) LES study of turbulent flows with submerged vegetation. Journal of Hydraulic Research 46(3), 307-316.

Czernuszenko, W., Rowinski, P. (Eds.), 2005. Water Quality Hazards and Dispersion of Pollutants. Springer ScienceþBusiness Inc., New York, NY, USA, ISBN 0-387- 23321-0, p. 250.

Dange, A. (2010) Modeling of turbulent particulate flow in the recirculation zone downstream of a backward facing step preceding a porous medium, Oklahoma State University.

Darmawan, S. and Tanujaya, H. (2019) CFD Investigation of Flow Over a Backward-facing Step using an RNG k-? Turbulence Model. Mechanical Engineering 10(2).

De Lima, P.H., Janzen, J.G. and Nepf, H.M. (2015) Flow patterns around two neighboring patches of emergent vegetation and possible implications for deposition and vegetation growth. Environmental Fluid Mechanics 15(4), 881-898.

DeBonis, J.R. (2022) A Large-Eddy Simulation Of Turbulent Flow Over A Backward Facing Step, p. 0337.

Demirel, E. and Aral, M.M. (2018) Performance of efficiency indexes for contact tanks. Journal of Environmental Engineering 144(9), 04018076.

Derakhshandeh, J. and Alam, M.M. (2019) A review of bluff body wakes. Ocean Engineering 182, 475-488.

Dimitris, S. and Panayotis, P. (2011) Macroscopic turbulence models and their application in turbulent vegetated flows. Journal of Hydraulic Engineering 137(3), 315-332.

Driver, D.M. and Seegmiller, H.L. (1985) Features of a reattaching turbulent shear layer in divergent channelflow. AIAA journal 23(2), 163-171.

Durst, F. and Tropea, C. (1983) Structure of Complex Turbulent Shear Flow, pp. 41-52, Springer.

Dworak, F.E. and Schwartz, J.S. (2007) Use of a 3D Hydrodynamic Model in an Incised Urban Channel with Woody Bank Vegetation to Evaluate Pool-Riffle Maintenance: Implications for Stream Restoration Design, pp. 1-11.

Endreny, T., Lautz, L., Siegel, D.I., 2011. Hyporheic flow path response to hydraulic jumps at river steps: flume and hydrodynamic models. Water Resour. Res. 47, W02517.

Erturk, E. (2008) Numerical solutions of 2-D steady incompressible flow over a backward-facing step, Part I: High Reynolds number solutions. Computers & Fluids 37(6), 633-655.

Etminan, V., Lowe, R.J. and Ghisalberti, M. (2017) A new model for predicting the drag exerted by vegetation canopies. Water Resources Research 53(4), 3179-3196.

Farzadkhoo, M., Keshavarzi, A., Hamidifar, H. and Ball, J. (2019) Flow and longitudinal dispersion in channel with partly rigid floodplain vegetation, pp. 229-240, Thomas Telford Ltd.

Finn, R. (1953) Determination of the drag on a cylinder at low Reynolds numbers. Journal of Applied Physics 24(6), 771-773.

Fischer-Antze, T., Stoesser, T., Bates, P. and Olsen, N. (2001) 3D numerical modelling of open-channel flow with submerged vegetation. Journal of Hydraulic Research 39(3), 303-310.

Fischer, J.L., Filip, G.P., Alford, L.K., Roseman, E.F. and Vaccaro, L. (2020) Supporting aquatic habitat remediation in the Detroit River through numerical simulation. Geomorphology 353, 107001.

Franck, J. A. (2009). Large-eddy simulation of flow separation and control on a wall-mounted hump. Doctrol thesis in California Institute of Technology.

Follett, E., Schalko, I., & Nepf, H. (2021). Logjams With a Lower Gap: Backwater Rise and Flow Distribution Beneath and Through Logjam Predicted by Two-Box Momentum Balance. Geophysical Research Letters, 48(16), e2021GL094279.

Furuichi, N., Hachiga, T. and Kumada, M. (2004) An experimental investigation of a large-scale structure of a two-dimensional backward-facing step by using advanced multi-point LDV. Experiments in Fluids 36(2), 274-281.

Gao, Y., Muzzio, F.J. and Ierapetritou, M.G. (2012) A review of the Residence Time Distribution (RTD) applications in solid unit operations. Powder technology 228, 416-423.

Gaur, N., Lingeshwar, R. and Kannan, B. (2022) Computational analysis of backward facing step flow using OpenFOAM®, p. 030005, AIP Publishing LLC.

Gautier, N. and Aider, J.-L. (2014) Feed-forward control of a perturbed backward-facing step flow. Journal of fluid mechanics 759, 181-196.

Ghani, U., Anjum, N., Pasha, G.A. and Ahmad, M. (2019) Numerical investigation of the flow characteristics through discontinuous and layered vegetation patches of finite width in an open channel. Environmental Fluid Mechanics 19(6), 1469-1495.

Golpira, A., Baki, A., Ghamry, H., Katopodis, C., Withers, J. and Minkoff, D. (2022) An experimental study: effects of boulder placement on hydraulic metrics of instream habitat complexity. Scientific reports 12(1), 1-18.

Gualtieri, C. (2005) Numerical simulations of laminar backward-facing step flow with FemLab 3.1, pp. 657-662.

Gualtieri, C. (2008) Numerical simulation of flow patterns and mass exchange processes in dead zones.

Gualtieri, C. (2009a) Analysis of flow and concentration fields in a baffled circular storage tank, pp. 4384-4392.

Gualtieri, C. (2009b) Modeling 2D laminar steady-state flow over a rectangular cavity. Environ. Comput. Solut.

Gualtieri, C. (2010) Advances in environmental fluid mechanics, pp. 249-274, World Scientific.

Gualtieri, P., et al. (2011). "Integral length scales in vegetated open channel flows." HEFAT 2011.

Gualtieri, C., Abdi, R., Ianniruberto, M., Filizola, N. and Endreny, T.A. (2020) A 3D analysis of spatial habitat metrics about the confluence of Negro and Solimões rivers, Brazil. Ecohydrology 13(1), e2166.

Gualtieri, C., Ianniruberto, M., Filizola, N., Santos, R. and Endreny, T. (2017) Hydraulic complexity at a large river confluence in the Amazon basin. Ecohydrology 10(7), e1863.

Gualtieri, C., Jiménez, L. and Rodríguez, J. (2010) Modelling turbulence and solute transport in a square dead zone.

Gualtieri, P., De Felice, S., Pasquino, V. and Doria, G.P. (2018) Use of conventional flow resistance equations and a model for the Nikuradse roughness in vegetated flows at high submergence. Journal of Hydrology and Hydromechanics 66(1), 107.

Gualtieri, P., Doria, G.P. and Taglialatela, L. (2004) Influence of vegetation height and density on a turbulent boundary layer.

Guo, G.-m., Liu, H. and Zhang, B. (2017) Numerical study of active flow control over a hypersonic backward-facing step using supersonic jet in near space. Acta Astronautica 132, 256-267.

Gurarslan, G., Karahan, H., Alkaya, D., Sari, M. and Yasar, M. (2013) Numerical solution of advection-diffusion equation using a sixth-order compact finite difference method. Mathematical Problems in Engineering 2013.

Hart, F.L. (1979) Improved hydraulic performance of chlorine contact chambers. Journal (Water Pollution Control Federation), 2868-2875.

Heenan, A. and Morrison, J. (1998) Passive control of pressure fluctuations generated by separated flow. AIAA journal 36(6), 1014-1022.

Harleman, D. R. F., & Rumer, R. R. (1963). Longitudinal and lateral dispersion in an isotropic porous medium. Journal of Fluid Mechanics, 16(3), 385-394.

Hemavathi, S., Manjula, R. and Ponmani, N. (2019) Numerical Modelling and Experimental Investigation on the Effect of Wave Attenuation Due to Coastal Vegetation, pp. 99-110, Springer.

Heseltine, J.L. (2011) Flow around a circular cylinder with a free end.

HU, R., WANG, L. and FU, S. (2015) Review of backward-facing step flow and separation reduction. SCIENTIA SINICA Physica, Mechanica & Astronomica 45(12), 124704.

Huai, W.-X., Zhang, J., Wang, W.-J. and Katul, G.G. (2019) Turbulence structure in open channel flow with partially covered artificial emergent vegetation. Journal of Hydrology 573, 180-193.

Huai, W., Xue, W. and Qian, Z. (2015) Large-eddy simulation of turbulent rectangular open-channel flow with an emergent rigid vegetation patch. Advances in Water Resources 80, 30-42.

Hussain, S. and Ahmed, S.E. (2019) Unsteady MHD forced convection over a backward facing step including a rotating cylinder utilizing Fe3O4-water ferrofluid. Journal of Magnetism and Magnetic Materials 484, 356-366.

Iaccarino, G. (2001) Predictions of a turbulent separated flow using commercial CFD codes. J. Fluids Eng. 123(4), 819-828.

Jahra, F., Kawahara, Y., Hasegawa, F. and Yamamoto, H. (2011) Flow–vegetation interaction in a compound open channel with emergent vegetation. International journal of river basin management 9(3-4), 247-256.

Jehad, D., Hashim, G., Zarzoor, A. and Azwadi, C.N. (2015) Numerical study of turbulent flow over backward-facing step with different turbulence models. Journal of Advanced Research Design 4(1), 20-27.

Jauregui, R., & Silva, F. (2011). Numerical validation methods. Numerical analysis—theory and application, 155-174.

Jing, H.-f., Cai, Y.-j., Wang, W.-h., Guo, Y.-k., Li, C.-g. and Bai, Y.-c. (2019) Investigation of open channel flow with unsubmerged rigid vegetation by the lattice Boltzmann method. Journal of Hydrodynamics, 1-13.

Jongebloed, L. (2008) Numerical study using FLUENT of the separation and reattachment points for backwards-facing step flow. Master's thesis in mechanical engineering, Rensselaer Polytechnic Institute.

Jovic, S. and Driver, D. (1995) Reynolds number effect on the skin friction in separated flows behind a backward-facing step. Experiments in Fluids 18(6), 464-467.

Jovic, S. and Driver, D.M. (1994) Backward-facing step measurements at low Reynolds number, Re (sub h)= 5000.

Kalinowska, M.B., Västilä, K., Kozioł, A., Rowiński, P.M., Kiczko, A. and Kubrak, J. (2020) Recent Trends in Environmental Hydraulics, pp. 91-101, Springer.

Kasagi, N. and Matsunaga, A. (1995) Three-dimensional particle-tracking velocimetry measurement of turbulence statistics and energy budget in a backward-facing step flow. International journal of heat and fluid flow 16(6), 477-485.

Keyes, D., Ecer, A., Satofuka, N., Fox, P. and Periaux, J. (2000) Parallel Computational Fluid Dynamics' 99: Towards Teraflops, Optimization and Novel Formulations, Elsevier.

Kim, D. and Moin, P. (2010) Direct numerical study of air layer drag reduction phenomenon over a backward-facing step. Center for Turbulence Research, Annual Research Briefs, 351-363.

Kim, H., Kimura, I. and Park, M. (2018) Numerical simulation of flow and suspended sediment deposition within and around a circular patch of vegetation on a rigid bed. Water Resources Research 54(10), 7231-7251.

Kim, J. and Choi, H. (2005) Distributed forcing of flow over a circular cylinder. Physics of fluids 17(3), 033103.

Kim, J., Kline, S. and Johnston, J.P. (1980) Investigation of a reattaching turbulent shear layer: flow over a backward-facing step.

Kim, J.J. (1978) Investigation of separation and reattachment of a turbulent shear layer: flow over a backward-facing step, Stanford University.

30. Kopera, M.A.; Kerr, R.M.; Blackburn, H.; Barkley, D. Direct numerical Ssimulation of turbulent flow over a backward-facing step. Doctoral dissertation University of Warwick, 2011 Kozarek, J., Hession, W., Dolloff, C. and Diplas, P. (2010) Hydraulic complexity metrics for evaluating in-stream brook trout habitat. Journal of Hydraulic Engineering 136(12), 1067-1076.

Krishnamoorthy, C. (2007) Numerical analysis of backward-facing step flow preceeding a porous medium using FLUENT, Oklahoma State University.

Kuehn, D.M. (1980) Effects of adverse pressure gradient on the incompressible reattaching flow over a rearward-facing step. AIAA journal 18(3), 343-344.

Kumar, A. and Dhiman, A.K. (2012) Effect of a circular cylinder on separated forced convection at a backward-facing step. International journal of thermal sciences 52, 176-185.

L'Hommedieu, W., Tullos, D. and Jones, J. (2020) Effects of an engineered log jam on spatial variability of the flow field across submergence depths. River Research and Applications 36(3), 383-397.

Lan, H., Armaly, B. and Drallmeier, J. (2009) Three-dimensional simulation of turbulent forced convection in a duct with backward-facing step. International journal of heat and mass transfer 52(7-8), 1690-1700.

Launder, B.E. and Spalding, D.B. (1972) Lectures in mathematical models of turbulence.

Le Moullec, Y., Gentric, C., Potier, O. & Leclerc, J. (2010a). Comparison of systemic, compartmental and CFD modelling approaches: application to the simulation of a biological reactor of wastewater treatment. Chemical Engineering Science 65, 343–350.

Le Moullec, Y., Gentric, C., Potier, O. & Leclerc, J. (2010b). CFD Simulation of the hydrodynamics and reactions in an activated sludge channel reactor of wastewater treatment

Le, H., Moin, P. and Kim, J. (1997) Direct numerical simulation of turbulent flow over a backward-facing step. Journal of fluid mechanics 330, 349-374.

Lee, T. and Mateescu, D. (1998) Experimental and numerical investigation of 2-D backward-facing step flow. Journal of Fluids and Structures 12(6), 703-716.

Lees, M.J., Camacho, L.A. and Chapra, S. (2000) On the relationship of transient storage and aggregated dead zone models of longitudinal solute transport in streams. Water Resources Research 36(1), 213-224.

Lera, S., Nardin, W., Sanford, L., Palinkas, C. and Guercio, R. (2019) The impact of submersed aquatic vegetation on the development of river mouth bars. Earth surface processes and landforms 44(7), 1494-1506.

Liaw, K.F. (2005) Simulation of flow around bluff bodies and bridge deck sections using CFD, University of Nottingham Nottingham.

Lienhard, J.H. (1966) Synopsis of lift, drag, and vortex frequency data for rigid circular cylinders, Technical Extension Service, Washington State University Pullman, WA.

Liu, M., Huai, W., Ji, B. and Han, P. (2021) Numerical study on the drag characteristics of rigid submerged vegetation patches. Physics of fluids 33(8), 085123.

Loksupapaiboon, K. and Suvanjumrat, C. (2021) Numerical simulation of flow over a passive disturbance and backward-facing step, p. 012046, IOP Publishing.

Louda, P., Příhoda, J., Kozel, K. and Sváček, P. (2013) Numerical simulation of flows over 2D and 3D backward-facing inclined steps. International journal of heat and fluid flow 43, 268-276.

Lu, J. and Dai, H. (2018) Numerical modeling of pollution transport in flexible vegetation. Applied Mathematical Modelling 64, 93-105.

Luo, D. (2019) Numerical simulation of turbulent flow over a backward facing step using partially averaged Navier-Stokes method. Journal of Mechanical Science & Technology 33(5).

Marjoribanks, T.I., Hardy, R.J., Lane, S.N. and Parsons, D.R. (2014) High-resolution numerical modelling of flow—vegetation interactions. Journal of Hydraulic Research 52(6), 775-793.

Marjoribanks, T.I., Hardy, R.J., Lane, S.N. and Tancock, M.J. (2017) Patch-scale representation of vegetation within hydraulic models. Earth surface processes and landforms 42(5), 699-710.

Mathupriya, P., Chan, L., Hasini, H. and Ooi, A. (2018) Numerical study of flow characteristics around confined cylinder using openFOAM. International Journal of Engineering and Technology 7, 617-623.

Mihailović, D., Mimić, G., Gualtieri, P., Arsenić, I. and Gualtieri, C. (2017) Randomness representation of turbulence in canopy flows using Kolmogorov complexity measures. Entropy 19(10), 519.

Min, D., Fischer, P.F. and Pearlstein, A.J. (2020) High Schmidt number "Washout" of a soluble contaminant downstream of a backward-facing step. International journal of heat and mass transfer 159, 119740.

Modarres-Sadeghi, Y. (2022) Introduction to Fluid-Structure Interactions, Springer Nature.

Moffatt, H.K. (1964) Viscous and resistive eddies near a sharp corner. Journal of fluid mechanics 18(1), 1-18.

Moss, W., Baker, S. and Bradbury, L. (1979) Turbulent shear flows I, pp. 198-207, Springer.

Mushyam, A., Bergada, J.M. and Navid Nayeri, C. (2016) A numerical investigation of laminar flow over a backward facing inclined step. Meccanica 51(8), 1739-1762.

Nadge, P.M. and Govardhan, R. (2014) High Reynolds number flow over a backward-facing step: structure of the mean separation bubble. Experiments in Fluids 55(1), 1-22.

Neuhaus, V., and Mende, M. (2021) Engineered Large Wood Structures in Stream Restoration Projects in Switzerland: Practice-Based Experiences. Water, 13(18), 2520.

Nguyen, T.H.T., Ahn, J. and Park, S.W. (2018) Numerical and physical investigation of the performance of turbulence modeling schemes around a scour hole downstream of a fixed bed protection. Water 10(2), 103.

Nguyen, V., Nguyen-Thoi, T. and Duong, V. (2021) Characteristics of the flow around four cylinders of various shapes. Ocean Engineering 238, 109690.

Norberg, C. (2003) Fluctuating lift on a circular cylinder: review and new measurements. Journal of Fluids and Structures 17(1), 57-96.

Nuruzzaman, M., Anwar, A.F., Sarukkalige, R. and Sarker, D.C. (2021) Review of hydraulics of Floating Treatment Islands retrofitted in waterbodies receiving stormwater. Science of The Total Environment, 149526.

O'Malley, K., Fitt, A., Jones, T., Ockendon, J. and Wilmott, P. (1991) Models for high-Reynolds-number flow down a step. Journal of fluid mechanics 222, 139-155.

Ötügen, M. (1991) Expansion ratio effects on the separated shear layer and reattachment downstream of a backward-facing step. Experiments in Fluids 10(5), 273-280.

OpenFOAM, 2021. OpenFOAM User Guide v-2112. The Open Source CFD Toolbox. www.openfoam.org

Park, H. and Thornber, B. (2018) DES of Flow Past an Oscillating Cylinder Located Downstream of Backward-Facing Step.

Penna, N., Coscarella, F. and Gaudio, R. (2020) Turbulent flow field around horizontal cylinders with scour hole. Water 12(1), 143.

Pereira, F.S., Eça, L., Vaz, G. and Girimaji, S.S. (2019) On the simulation of the flow around a circular cylinder at Re= 140,000. International journal of heat and fluid flow 76, 40-56.

Prihoda, J., Zubik, P., Sulc, J. and Sedlar, M. (2012) Experimental and numerical modelling of turbulent flow over an inclined backward-facing step in an open channel. Communications-Scientific letters of the University of Zilina 14(4A), 6-12.

Rahimi, H., Tang, X. and Singh, P. (2020) Experimental and numerical study on impact of double layer vegetation in open channel flows. Journal of Hydrologic Engineering 25(2), 04019064.

Ratha, D. and Sarkar, A. (2015) Analysis of flow over backward facing step with transition. Frontiers of Structural and Civil Engineering 9(1), 71-81.

Ren, J., Wang, X., Zhou, Y., Chen, B., & Men, L. (2019). An analysis of the factors affecting hyporheic exchange based on numerical modeling. Water, 11(4), 665.

Roache, P.J. (1997) Quantification of uncertainty in computational fluid dynamics. Annual review of fluid Mechanics 29(1), 123-160.

Roache, P.J. (2009) Perspective: Validation—What does it mean?

Robertson, Eric, et al. (2015) Validation of OpenFOAM numerical methods and turbulence models for incompressible bluff body flows." Computers & Fluids 123: 122-145.

Ruck, B. and Makiola, B. (1988) Particle dispersion in a single-sided backward-facing step flow. International Journal of Multiphase Flow 14(6), 787-800.

Ruck, B. and Makiola, B. (1993) Physics of Separated Flows—Numerical, Experimental, and Theoretical Aspects, pp. 47-55, Springer.

Saleel, C. A., A. Shaija, and S. Jayaraj. (2013) Computational simulation of fluid flow over a triangular step using immersed boundary method. International Journal of Computational Methods. 10.04: 1350016.

Samstag, R. W., Ducoste, J. J., Griborio, A., Nopens, I., Batstone, D. J., Wicks, J. D., & Laurent, J. (2016). CFD for wastewater treatment: an overview. Water Science and Technology, 74(3), 549-563.

Schalko, I., Wohl, E. and Nepf, H.M. (2021) Flow and wake characteristics associated with large wood to inform river restoration. Scientific reports 11(1), 1-12.

Selimefendigil, F. and Öztop, H.F. (2013) Identification of forced convection in pulsating flow at a backward facing step with a stationary cylinder subjected to nanofluid. International Communications in Heat and Mass Transfer 45, 111-121.

Selimefendigil, F. and Öztop, H.F. (2014) Effect of a rotating cylinder in forced convection of ferrofluid over a backward facing step. International journal of heat and mass transfer 71, 142-148.

Selimefendigil, F. and Öztop, H.F. (2015) Numerical investigation and reduced order model of mixed convection at a backward facing step with a rotating cylinder subjected to nanofluid. Computers & Fluids 109, 27-37.

Shields, F.D. and Rigby, J. (2005) River habitat quality from river velocities measured using acoustic Doppler current profiler. Environmental Management 36(4), 565-575.

Shu, C., Peng, Y., Zhou, C. and Chew, Y. (2006) Application of Taylor series expansion and Least-squares-based lattice Boltzmann method to simulate turbulent flows. Journal of Turbulence (7), N38.

Singh, A., Aravind, S., Srinadhi, K. and Kannan, B. (2020) Assessment of Turbulence Models on a Backward Facing Step Flow Using OpenFOAM®, p. 042060, IOP Publishing.

Singh, A.P., Paul, A.R. and Ranjan, P. (2011) Investigation of reattachment length for a turbulent flow over a backward facing step for different step angle. International Journal of Engineering, Science and Technology 3(2).

Smirnov, E., Smirnovsky, A., Schur, N., Zaitsev, D. and Smirnov, P. (2018) Comparison of RANS and IDDES solutions for turbulent flow and heat transfer past a backward-facing step. Heat and Mass Transfer 54(8), 2231-2241.

Smith, D.L., Goodwin, R.A. and Nestler, J.M. (2014) Relating turbulence and fish habitat: a new approach for management and research. Reviews in Fisheries Science & Aquaculture 22(2), 123-130.

Sokáč, M., Velísková, Y. and Gualtieri, C. (2018) An approximate method for 1-D simulation of pollution transport in streams with dead zones. J. Hydrol. Hydromech 66(4), 437-447.

Sokáč, M., Velísková, Y. and Gualtieri, C. (2019) Application of asymmetrical statistical distributions for 1D simulation of solute transport in streams. Water 11(10), 2145.

Sonnenwald, F., Guymer, I. and Stovin, V. (2019) A CFD-based mixing model for vegetated flows. Water Resources Research 55(3), 2322-2347.

Southard, J. (2000) An Introduction to fluid motions and sediment transport. Eastern Section SEPM Short Course.

Sparrow, E. and Kalejs, J. (1977) Local convective transfer coefficients in a channel downstream of a partially constricted inlet. International journal of heat and mass transfer 20(11), 1241-1249.

Spazzini, P.G., Iuso, G., Onorato, M., Zurlo, N. and Di Cicca, G. (2001) Unsteady behavior of back-facing step flow. Experiments in Fluids 30(5), 551-561.

Stamou, A., Papadonikolaki, G., Gkesouli, A., Nikoletopoulos, A., University of the Aegean, L.I.D.o.E.S. and University of the Aegean, L.I.D.o.E.S. (2011) Modeling the effect of vegetation on river floodplain hydraulics, University of the Aegean, Rhodes Island(Greece).

Stoesser, T., Kim, S. and Diplas, P. (2010) Turbulent flow through idealized emergent vegetation. Journal of Hydraulic Engineering 136(12), 1003-1017.

Suzuki, H., Kida, S., Nakamae, T. and Suzuki, K. (1991) Flow and heat transfer over a backward-facing step with a cylinder mounted near its top corner. International journal of heat and fluid flow 12(4), 353-359.

Tahseen, T.A., Eleiwi, M.A. and Hameed, A.F. (2020) Numerical study of fluid flow and heat transfer in a backward facing step with three adiabatic circular cylinder. Journal of Advanced Research in Fluid Mechanics and Thermal Sciences 72(1), 80-93.

Teixeira, E.C. and do Nascimento Siqueira, R. (2008) Performance assessment of hydraulic efficiency indexes. Journal of Environmental Engineering 134(10), 851-859.

Terekhov, V., Smul'skii, Y.I. and Sharov, K. (2016) Experimental study of the separated flow structure behind a backward-facing step and a passive disturbance. Journal of Applied Mechanics and Technical Physics 57(1), 180-187.

Tihon, J., Legrand, J. and Legentilhomme, P. (2001) Near-wall investigation of backward-facing step flows. Experiments in Fluids 31(5), 484-493.

Tihon, J., Pěnkavová, V., Havlica, J. and Šimčík, M. (2012) The transitional backward-facing step flow in a water channel with variable expansion geometry. Experimental Thermal and Fluid Science 40, 112-125.

Tihon, J., Pěnkavová, V. and Pantzali, M. (2010) The effect of inlet pulsations on the backward-facing step flow. European Journal of Mechanics-B/Fluids 29(3), 224-235.

Togun, H., Safaei, M.R., Sadri, R., Kazi, S.N., Badarudin, A., Hooman, K. and Sadeghinezhad, E. (2014) Numerical simulation of laminar to turbulent nanofluid flow and heat transfer over a backward-facing step. Applied Mathematics and Computation 239, 153-170.

Tollner, E., Barfield, B., Vachirakornwatana, C. and Haan, C. (1977) Sediment deposition patterns in simulated grass filters. Transactions of the ASAE 20(5), 940-0944.

Toumey, J., Zhang, P., Zhao, X., Colborn, J. and O'Connor, J.A. (2022) Assessing the wall effects of backwards-facing step flow in tightly-coupled experiments and simulations, p. 0822.

Triton, D. (1959) Experiments on the flow past a circular cylinder at low Reynolds number. J. Fluid Mech. 6, 547.

Tsai, C.-P., Ying-Chi, C., Sihombing, T.O. and Chang, L. (2017) Simulations of moving effect of coastal vegetation on tsunami damping. Natural Hazards and Earth System Sciences 17(5), 693.

Tsakiri, M., Prinos, P. and Koftis, T. (2016) Numerical simulation of turbulent exchange flow in aquatic canopies. Journal of Hydraulic Research 54(2), 131-144.

Uruba, V., Jonáš, P. and Mazur, O. (2007) Control of a channel-flow behind a backward-facing step by suction/blowing. International journal of heat and fluid flow 28(4), 665-672.

Vargas-Luna, A., Crosato, A., Calvani, G. and Uijttewaal, W.S. (2016) Representing plants as rigid cylinders in experiments and models. Advances in water resources 93, 205-222.

Vargas Luna, A. (2016) Role of vegetation on river bank accretion.

Viti, N., Valero, D. and Gualtieri, C. (2018) Numerical simulation of hydraulic jumps. Part 2: Recent results and future outlook. Water 11(1), 28.

Wang, F.-f., Wu, S.-q. and Zhu, S.-l. (2019) Numerical simulation of flow separation over a backward-facing step with high Reynolds number. Water Science and Engineering 12(2), 145-154.

Westphal, R.V., Johnston, J. and Eaton, J. (1984) Experimental study of flow reattachment in a single-sided sudden expansion.

Wilcox, D.C. (1998) Turbulence modeling for CFD, DCW industries La Canada, CA.

Williamson, C. (1996) K. Vortex dynamics in the cylinder wake. Annual review of fluid Mechanics 28(1), 477-539.

Wu, J. and Yu, X. (2021) Numerical investigation of dissolved oxygen transportation through a coupled SWE and Streeter–Phelps model. Mathematical Problems in Engineering 2021.

Xiaohui, S. and Li, C. (2002) Large eddy simulation of free surface turbulent flow in partly vegetated open channels. International Journal for Numerical Methods in Fluids 39(10), 919-937.

Xu, J., Zou, S., Inaoka, K. and Xi, G. (2017) Effect of Reynolds number on flow and heat transfer in incompressible forced convection over a 3D backward-facing step. International Journal of Refrigeration 79, 164-175.

Yakhot, V. and Orszag, S.A. (1986) Renormalization group analysis of turbulence. I. Basic theory. Journal of scientific computing 1(1), 3-51.

Yan, X.-F., Wai, W.-H.O. and Li, C.-W. (2016) Characteristics of flow structure of free-surface flow in a partly obstructed open channel with vegetation patch. Environmental Fluid Mechanics 16(4), 807-832.

Yang, X.-D., Ma, H.-Y. and Huang, Y.-N. (2005) Prediction of homogeneous shear flow and a backward-facing step flow with some linear and non-linear K–ε turbulence models. Communications in Nonlinear Science and Numerical Simulation 10(3), 315-328.

Yang, Z., Bai, F., Huai, W., An, R. and Wang, H. (2017) Modelling open-channel flow with rigid vegetation based on two-dimensional shallow water equations using the lattice Boltzmann method. Ecological Engineering 106, 75-81.

Yao, S. (2000) Two dimensional backward facing single step flow preceding an automotive air-filter, Oklahoma State University.

Zafar, F. and Alam, M.M. (2019) Flow structure around and heat transfer from cylinders modified from square to circular. Physics of fluids 31(8), 083604.

Zhang, C. and Zhang, M. (2023) Numerical investigation of solitary wave attenuation and mitigation caused by vegetation using OpenFOAM. Coastal Engineering Journal, 1-19.

Zhang, J.-t. and Su, X.-h. (2008) Numerical model for flow motion with vegetation. Journal of Hydrodynamics 20(2), 172-178.

Zhang, J., Zhang, N., Zhang, Q., Jiao, F., Xu, L. and Qi, J. (2022) Numerical Simulation of Wave Overtopping of an Ecologically Honeycomb-Type Revetment with Rigid Vegetation. Journal of Marine Science and Engineering 10(11), 1615.

Zhao, F. and Huai, W. (2016) Hydrodynamics of discontinuous rigid submerged vegetation patches in open-channel flow. Journal of Hydro-environment Research 12, 148-160.

Zhao, F., Huai, W. and Li, D. (2017) Numerical modeling of open channel flow with suspended canopy. Advances in water resources 105, 132-143.

Zhou, J. and Venayagamoorthy, S.K. (2019) Near-field mean flow dynamics of a cylindrical canopy patch suspended in deep water. Journal of Fluid Mechanics 858, 634-655.

Zhou, T., & Endreny, T. A. (2013). Reshaping of the hyporheic zone beneath river restoration structures: Flume and hydrodynamic experiments. Water Resources Research, 49(8), 5009-5020.